



Universiteit
Leiden
The Netherlands

Proximity effects in superconducting spin-valve structures
Flokstra, M.G.

Citation

Flokstra, M. G. (2010, February 17). *Proximity effects in superconducting spin-valve structures*. *Casimir PhD Series*. Retrieved from <https://hdl.handle.net/1887/14751>

Version: Corrected Publisher's Version

License: [Licence agreement concerning inclusion of doctoral thesis in the Institutional Repository of the University of Leiden](#)

Downloaded from: <https://hdl.handle.net/1887/14751>

Note: To cite this publication please use the final published version (if applicable).

Proximity effects in superconducting spin-valve structures

Proximity effects in superconducting spin-valve structures

Proefschrift

ter verkrijging van
de graad van Doctor aan de Universiteit Leiden,
op gezag van Rector Magnificus prof.mr. P.F. van der Heijden,
volgens besluit van het College voor Promoties
te verdedigen op woensdag 17 februari 2010
klokke 16.15 uur
door

Machiel Geert Flokstra

geboren op 10 juli 1979
te Oldenzaal

Dit proefschrift is goedgekeurd door de promotor:

Prof. dr. J. Aarts

Samenstelling van de promotiecommissie:

Prof. dr. J. Aarts	Universiteit Leiden, promotor
Prof. dr. C.W.J. Beenakker	Universiteit Leiden
Dr. ir. A. Brinkman	Technische Universiteit Twente
Prof. dr. P.H. Kes	Universiteit Leiden
Prof. dr. ir. T.M. Klapwijk	Technische Universiteit Delft
Prof. dr. S. L. Lee	University of St Andrews, Schotland
Prof. dr. J.M. van Ruitenbeek	Universiteit Leiden

Contents

1	Introduction	1
1.1	Superconductivity	2
1.2	S/F junctions	5
1.3	Motivation & Outline	8
2	Theoretical concepts	11
2.1	Fundamentals of superconductivity	12
2.1.1	Foundation of the microscopical description	12
2.1.2	Bogoliubov-de Gennes equation	15
2.1.3	Green functions and the Gor'kov equation	16
2.1.4	Quasiclassical approximation: Usadel equation	20
2.1.5	Unconventional Cooper pairs	24
2.2	Fundamentals of ferromagnetism	26
2.2.1	Magnetic domains and switching	28
2.3	Proximity effect	31
2.3.1	Proximity effect in S/N	31
2.3.2	Proximity effect in S/F	33
3	Experimental details	37
3.1	Sample specifics	38
3.2	Measurement setup specifics	41
4	Superconducting spin-valve: weak ferromagnetic case	43
4.1	Introduction	44
4.2	The superconducting spin-valve	45
4.3	Sample details	48
4.4	Results	50
4.4.1	Results on the 2 μm bridge	51
4.4.2	Other bilayers and trilayers	55
4.4.3	$I_c(H)$ well below T_c	57
4.5	The influence of magnetic contacts	60

4.6	Conclusions	62
5	Superconducting spin-valve: strong ferromagnetic case	65
5.1	Introduction	66
5.2	Polarized spin bands	67
5.3	Experimental details	70
5.4	Results	72
5.4.1	$R(H)$ for $T > T_c$	72
5.4.2	$R(H)$ for $T < T_c$	76
5.4.3	$I_c(H)$ for T well below T_c	79
5.4.4	Exchange biased Py	80
5.5	Discussion and conclusion	81
6	Probing reversed proximity in the spin-valve using LE-μSR	85
6.1	Introduction	86
6.2	Description of the measurement technique	88
6.2.1	Principle of muon spin rotation	88
6.2.2	Experimental setup	91
6.3	Results	97
6.3.1	Experimental details	97
6.3.2	Fitting of the data	98
6.3.3	Discussion and conclusion	107
7	Critical voltage of a mesoscopic superconductor	109
7.1	Introduction	110
7.1.1	Usadel equation using Keldysh technique	112
7.1.2	Working out the equations	114
7.1.3	Simulation on the NSN system	116
7.1.4	Simulation on the non-local system	118
	Bibliography	121
	Samenvatting	127
	List of publications	131
	Curriculum Vitae	133
	Acknowledgements	135

Chapter 1

Introduction

1.1 Superconductivity

Absolutely nothing... is all that is left of the resistance of a superconductor. This stunning result was first seen by Heike Kamerlingh Onnes in 1911 at the university of Leiden when cooling down a piece of metallic Mercury (Hg) to below 4.2 K [1]. Normally for metallic substances the electrical resistance goes down with decreasing temperature and saturates at low temperatures meaning that a finite resistance remains, caused by imperfections to the (infinite) crystal lattice. The unique property of a superconductor is that the resistance suddenly vanishes at the moment that the temperature falls below the critical temperature (T_c) of the material (see Fig. 1.1).

Several well-known elemental superconductors are Aluminum (Al), Tin (Sn), Lead (Pb) and Niobium (Nb) with respective T_c 's of 1.2, 3.7, 7.2 and 9.3 K. The latter being the highest of elemental bulk superconductors. Higher T_c 's are found in a variety of alloys and compounds. Widely used are the compounds of Niobium with Nitrogen (NbN) and with Titanium (Nb_{0.6}Ti_{0.4}), which have respective T_c 's of 16.1 and 9.8 K. In 1986, a new class of superconductors was discovered by Bednorz and Müller [2], the superconducting copper-oxides (cuprates). These are synthesized ceramic compounds with a perovskite crystal structure. A (at that

time) staggering T_c as high as 92 K was found in the cuprate YBa₂Cu₃O₇, now known as YBCO (Yttrium-Barium-Copper-Oxide). This meant superconductivity at temperatures above the liquid Nitrogen (LN₂) temperature of 77 K, which is the standard coolant to get far below room temperature. Currently the highest observed T_c for a bulk material is found in a cuprate and reaches 138 K (the cuprate being (Hg_{0.8}Tl_{0.2})Ba₂Ca₂Cu₃O_{8.33}). The complete disappearance of electrical resistance is not the only unique property of a superconductor. A second important property is the expulsion of magnetic flux from the interior of the superconductor (Meissner effect [3]) which also starts when the temperature gets below T_c . This is very different from ordinary, non-superconducting matter, where magnetic flux can (almost) penetrate straight through. Two main types of superconductors are distinguished based on their ability to expel magnetic flux. In type-I superconductors the expulsion is

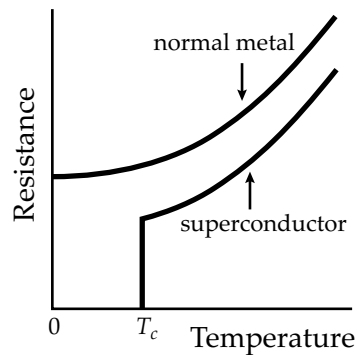


Figure 1.1: Typical resistance versus temperature curves for a normal metal and superconductor with transition temperature T_c .

complete up to a certain maximum or critical field H_{c1} , above which the superconductor returns to the normal state. Type-II superconductors also show complete expulsion up to a field H_{c1} , but now for higher fields magnetic flux starts to enter the superconductor in the form of small flux bundles, so-called vortices, crossing the interior of the superconductor (see Fig. 1.2). These

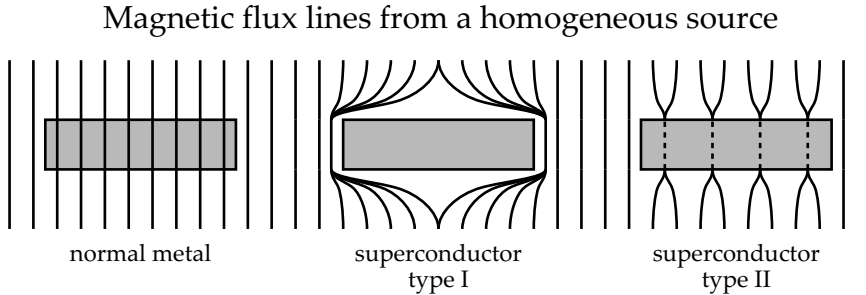


Figure 1.2: Magnetic flux lines through a normal metal, a type-I superconductor and a type-II superconductor. Dashed lines represent the vortices.

vortices are like tubes having a non-superconducting core and carry a single quantum of flux $\phi_0 = h/(2e)$. With increasing field the density of vortices increases until at a field H_{c2} the superconductor becomes normal. Almost all elemental superconductors are type-I (exceptions are Niobium, Vanadium (V) and Technetium (Tc)), while the cuprates and the other superconducting alloys and compounds are all type-II.

But what exactly *is* superconductivity? This question remained unanswered for almost 50 years. The microscopic mechanism and description of this phenomenon got shape in 1957, when it was recognized that an attractive interaction between electrons is needed. For the classical superconductors this is mediated by electron-phonon coupling, but for the high- T_c superconductors the interaction mechanism is not fully unravelled yet even at present day. In short, superconductivity is a condensed state (or condensate) of specially paired electrons isolated from the normal electrons by an energy gap Δ . The binding energy of the pairs is weak (order of meV) and easily destroyed by temperature, so only at very low temperatures superconductivity will appear. It is a macroscopic quantum phenomena which can be described by a single wave function characterized by an amplitude and phase (both in general functions of position and time). This condensate of electron pairs thus moves/acts as a single entity and is not hindered by the obstacles that cause dissipation for the normal electrons. One could say, the mechanism for dis-

sipation in normal metals (such as inelastic collisions with other electrons or the crystal lattice) are just not powerful enough to break these electron pairs apart. For temperatures *above* T_c the superconductor act as a normal metal. The Fermi sphere (the collection of electronic states) is filled up to the Fermi energy (E_F) with the exception of an energy shell of order $k_B T$ around E_F which contains excited states. Furthermore, around E_F the density of states is continuous and more or less constant. For temperatures *below* T_c the superconducting condensate emerges with a peculiar density of states around the Fermi energy; the condensate itself is located *at* E_F , but the continuum of states closely around E_F have disappeared. The condensate is isolated from the normal electron states by an an energy of Δ , both to the states below and above E_F . The full size of the energy gap is $2\Delta \sim 3.5k_B T_c$ (for weak coupling) and thus directly relates to T_c . The electron pairs in the condensate are called Cooper pairs, named after Leon Cooper who in 1956 came up with the idea of these pairs. The pairing goes in a special way: only electrons with opposite momentum (k-vector) and opposite spin can form a Cooper pair and condense into the condensate (in case of a conventional superconductor). The conventional Cooper pair thus contains an electron with spin up and an electron with spin down. This makes superconductivity intrinsically incompatible with magnetic fields, which tend to align all the electron spins. A direct result of the fact that the condensate can move freely, is that it can create circular currents (screening currents) to generate a magnetic field. This is what happens when a superconductor is exposed to magnetic flux; it generates and equal but opposite field to expel the magnetic flux from its interior. Can a superconductor expel just any field? No, because the supercurrent density, and thus the generated field strength, is limited. Above this maximum the Cooper pairs become unstable and the condensate collapses, forcing the superconductor back to the normal state. The field at which this happens is called the (upper) critical field, and the maximum current it can carry is the critical current I_c . Whether a superconductor is type-I or type-II depends on the ratio between two important parameters of the superconductor. These two are the superconducting coherence length ξ_S and the magnetic penetration depth λ . The first one (although a variety of definitions exists) is roughly the characteristic length over which Δ can change its amplitude significantly. It is also roughly the average size of a Cooper pair, which is a very non-local object. The second one is the distance over which magnetic flux can penetrate the superconductor from the sides/surfaces (a normal metal has infinite λ). If the ratio $\lambda/\xi_S < 1/\sqrt{2}$ the superconductor is type-I, else it is type-II, where for ξ_S the Ginzburg-Landau coherence length should be used. In other words, only when the magnetic field screening is strong enough to reduce λ to about

ξ_S , the superconductor can completely free its interior from magnetic flux. Otherwise, the superconductor gives up certain areas, in the form of vortices, to permit flux passing through its interior.

1.2 S/F junctions

Whenever (a layer of) one material is connected to another (layer of) material, an interface is created. At the interface the electronic states from both sides are glued together and the electronic properties of both materials become mixed in a small region near the interface. The quality of the interface determines the resistance, or better, the transmission and reflection probabilities for an incoming electron. In general these probabilities depend on the wave vector (or energy) and spin of the incoming electron. The latter becomes important when magnetic materials are used. The resulting interface region may have new properties (i.e. properties that don't appear in the bulk materials) and transport characteristics can change drastically. This makes it very interesting for both fundamental research and for applied / device-oriented research. A good example is the diode (or pn-junction), which is a very commonly used device and can be formed by connecting a p-type to an n-type doped semiconductor. It shows a highly non-linear (non-ohmic) current-voltage characteristic: the interface allows electrical current to pass in one direction, while blocking the other direction. Whenever a magnetic material is used the interface will have a spin dependent transmission/reflection. Usually the transmission for one spin direction is (much) better than for the opposite spin direction. This difference originates from the availability of electron states near the Fermi energy, which for magnetic materials are generally unequal for the two spin directions. A particular convenience of the electron spin is that its direction can be externally manipulated by applying a magnetic field. This possible manipulation combined with spin dependent interface properties has led to many spin based devices. Perhaps most important is the Giant-Magneto-Resistance (GMR) effect. In GMR devices, the electrical resistance can be changed significantly by a relative small external field. This effect forms the basis for modern spintronics, also called spin transport electronics. These are devices where the electron spin is exploited to manipulate the transport of its electrical charge, thus manipulating the transport characteristics of the device. Although superconductors can carry electrical current without energy loss, they are not well fitted to integrate in standard electronics due to the very low temperature of operation. Yet they have found their way into medical instruments where macroscopically large superconducting coils

Bloch states (plane waves) are defined by wave vector \mathbf{k} and spin σ

are used to generate high magnetic fields (necessary for the Magnetic Resonance Imaging (MRI) scanners) Next to this application of bulky "power" sources, they are also integrated into space technology electronics, usually as highly sensitive measurement/detection electronics (sensors), as in outer space the natural environment temperature is only a few Kelvin.

A superconductor (S) and ferromagnet (F) both have a global, but mutually antagonistic, ordering for electron spins. This makes that interfaces between the two materials (proximity systems) are expected to be very rich in physics as multiple energy and length scales are competing with each other. One of the main questions in these systems is: how does the induced superconductivity (in F) behave and over what distances can it survive. The main competitors are the superconducting gap energy Δ , the ferromagnetic exchange energy E_{ex} , the superconducting (ξ_S) and ferromagnetic (ξ_F) coherence length, and the size of the system (thicknesses of the layers). The energies Δ and E_{ex} are respectively coupled to the lengths ξ_S and ξ_F . Here, ξ_F is the typical distance over which Cooper pairs dephase in the F layer, and E_{ex} is related to the potential energy difference between the (Fermi levels of the) two spin bands. These S/F proximity systems are in general most interesting from a fundamental and theoretical point of view. The first reports on junctions between a superconductor and non-superconducting material date from 1970-1973. Meservey *et al.* [4] and Tedrow *et al.* [5, 6] examined S/F junctions and showed the existence of a spin-polarized current across Al/AlO_x/F junctions. From this an estimate for the degree of polarization of the ferromagnetic layer was obtained. The Aluminum-Oxide (AlO_x) is a (thin) insulator layer, and as ferromagnetic material they used Iron (Fe), Cobalt (Co), Nickel (Ni) and Gadolinium (Gd). In these experiments the superconductor was used for its distinctive quasiparticle density of state (quasiparticles are the elementary excitations of a system), which is zero for sub-gap energies and sharply peaked near the gap edge. During the same period, Tinkham and Clarke [7, 8] studied non-equilibrium superconductivity (which is an imbalance in the quasiparticle density of states) in S/N junctions. They found that the conversion of a normal (quasiparticle) current into a supercurrent leads to an imbalance in the quasiparticle spectrum inside the superconductor. The quasiparticles become distributed over the available states in a way similar to what is expected from an increase in temperature. Later it turned out that the effect of non-equilibrium superconductivity is fundamentally not very different from the effect of a ferromagnetic exchange field (or energy) on a superconductor.

The technological advancements in micro-structuring have boosted, and made it possible to investigate proximity systems on a mesoscopic scale. This

means down to the scale where the various characteristic lengths of the systems (like ξ_s) are competing (or: become visible). In S/F proximity systems, superconductivity is induced into a natural hostile environment, where it is broken down by the exchange energy E_{ex} roughly over a distance ξ_F . In a normal metal superconductivity is also broken down (roughly over a distance ξ_N), but the important energy is then the "temperature" $k_B T$ which is usually much smaller than E_{ex} , leading to $\xi_N \gg \xi_F$, and hence the Cooper pair dephasing in N is much weaker. Apart from the much smaller distance over which superconductivity survives in F, it also behaves in a rather different way. Instead of a clean monotonic decay, it oscillates (see Fig. 1.3). But the

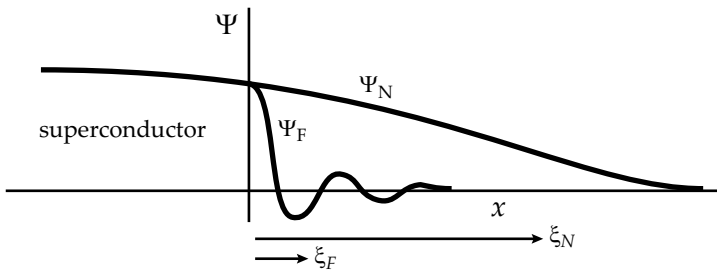


Figure 1.3: Amplitude of the (induced) superconducting wave function Ψ as function of distance x , in a normal metal Ψ_N and a ferromagnet Ψ_F , with ξ_N and ξ_F the respective coherence lengths.

interesting part does not stop with the oscillation, in fact, it is where it starts! The oscillations are not just simple amplitude oscillations. Instead, it is the nature of the pairing itself that is changing which causes this oscillation to appear. The conventional Cooper pair is in a spin singlet state, but now, under the influence of a homogeneous exchange field, spin triplet correlations appear (due to spin rotation of the conventional Cooper pairs) and the Cooper pair becomes a mixture of the two. Under the condition of inhomogeneous exchange fields, it is even possible to create all of the three spin triplet (instead of only the $m_z = 0$ component), which include the "spin equal" components ($m_z = \pm 1$). The ferromagnet has succeeded in changing a part of the normal Cooper pairs, which cannot live long in the ferromagnet, into other types of pairs for which the ferromagnet is no longer a specially hostile environment. This triplet pairing, or, more general, the effect of inhomogeneous exchange fields on the superconducting state, is currently a burning question and a serious research topic in the field of S/F proximity systems. Moreover, there is also interest in the behavior at the S-side of the interface where it is possible

that ferromagnetism is induced.

1.3 Motivation & Outline

The oscillation of the Cooper pair density appears whenever the Cooper pairs experience a homogeneous exchange field. However, for the generation of the "spin equal" triplet components the Cooper pairs need to experience a non-homogeneous exchange field. Such non-homogeneous exchange fields are found in magnetic domains and domain walls. About half of this thesis relates to this problem: what is the effect of inhomogeneous magnetism (in the form of domains and domain walls) on the superconducting state. Thus, rather than examining the induced superconductivity in the ferromagnet, we examine the changes to the superconducting state as caused by the magnetic domains. This we do in a special type of structure that gained much attention: the superconducting spin-valve. Also in such a spin-valve structure we search for traces of induced magnetism in the superconductor, and by replacing the ferromagnet for a normal metal under non-equilibrium conditions we (theoretically) examine non-equilibrium effects on the superconducting state. The latter two form the other half of this thesis.

The superconducting spin-valve consist of a superconductor sandwiched between two ferromagnetic layers (see Fig. 1.4). Calculations show that for such a device T_c is always higher if the magnetization, and therefore the exchange fields, form a anti-parallel (AP) configuration than if they form a parallel (P) configuration [9, 10]. In effect it is a organized inhomogeneous device, which can be switched from inhomogeneous (AP) to homogeneous (P). When the ferromagnetic layers are thin enough, they are also subject to the oscillatory nature of the induced superconductivity and can show full re-entrant behavior, which is the most interesting feature of such a device: the possibility to switch on and off superconductivity by a small field manipulation, and hence, controlling the supercurrent through the device. To gain control of the exchange field, soft magnetic materials are favorable since they can be switched by small external fields such to not disturb the condensate. To achieve separate switching, materials (or layers) with different switching fields can be used, or one could pin one of the layers by using an anti-ferromagnet. The latter one is the one proposed in the first proposal of the spin-valve and is most popular.

Theory describing the superconducting spin-valve (or more general, S/F proximity) is well developed for the case of weak ferromagnetism ($E_{\text{ex}} \ll E_F$)

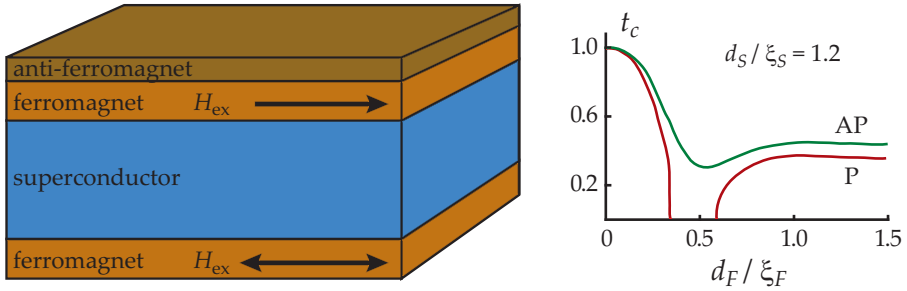


Figure 1.4: Schematic of the proposed superconducting spin-valve, where the direction of the exchange field H_{ex} of one of the layers is pinned by the anti-ferromagnet, while the other can be manipulated by a (small) external field. The calculations are taken from [9] (with interface transparency parameter $T_F = 25$) and show that the reduced transition temperature t_c in anti-parallel (AP) configuration is always higher compared to parallel (P) configuration of the ferromagnetic exchange fields. Here, d is the layer thickness, ξ the coherence length, and subscripts S and F denote the superconductor and ferromagnet.

with homogeneous exchange fields. For strong ferromagnetic materials, or for inhomogeneities in the exchange field (in particular from domains or domain walls), the framework is either intrinsically not suitable or poses severe difficulties. From the experimental side, measurements on spin-valves based on weak ferromagnets (and almost zero spin polarization) seem to coincide with the theoretical prediction, although the effects are generally weaker than what might be expected from theory. However, it is doubtful that the pre-assumed conditions of homogeneous exchange fields are always realized. This makes the interpretation of the results at least "open for discussion", as the effects of magnetic domains and domain walls might be the actual dominating mechanism for the observed effect. When using strong ferromagnets, where E_{ex} is no longer much smaller than E_F and there will be a non-zero spin polarization, contradictory looking results are obtained. Apart from differences in the sample geometry and/or used materials, dipolar fields coming from domains (or domain walls) are often mentioned as being the source for these results. As these main difficulties are all related to domains, it is only natural to examine these effects in more detail, which is the main part of this thesis. *Chapter two* describes the basics of the theoretical concepts encountered in the following chapters. *Chapter three* gives a brief description of the sample fabrication and measurements setup. *Chapter four and five* focus on the effect of domain structure in the ferromagnetic layers on the working of the superconducting spin-valve. This is examined for both the weak ferromagnetic based CuNi

spin-valve (chapter four) as for the strong ferromagnetic based Py spin-valve (chapter five). *Chapter six* is a rather different type of experiment on the superconducting spin-valve, where an attempt is made to detect inverse proximity (induced magnetism in the superconductor) by the usage of muon spin rotation experiments. *Chapter seven* is a theoretical work on non-equilibrium superconductivity in a mesoscopic superconducting wire, connected to normal metallic reservoirs.

Chapter 2

Theoretical concepts

2.1 Fundamentals of superconductivity

2.1.1 Foundation of the microscopical description

The work of Cooper [11] (1956) shows that if the interaction between electrons leads to a net attraction between two electrons close to the Fermi surface, then bound states can be formed located below the Fermi surface. The density of these bound states strongly depends on the total momentum K of the pair, being at a maximum where $K = 0$ and rapidly going to zero for non-zero K . It was therefore suggested that the elementary excitations of the pair were most likely to correspond to the splitting of the pair rather than to increasing the kinetic energy of the pair (since its density falls off so quickly with increasing K). Such net attractive interaction between electrons can occur when the attractive phonon interaction dominates the Coulomb repulsion. Where the latter mechanism is just the direct repulsion between two particles of the same charge, the first mechanism is an indirect interaction. The negatively charged electron slightly deforms the surrounding lattice by pulling on the positively charged atoms and while the electron moves around, it leaves a trail (or wave) of such deformations (or phonons). As this is an area with slightly increased positive charge, it attracts new electrons. Effectively, by this mechanism electrons attract each other mediated by phonons. In the works of Bardeen, Cooper and Schrieffer [12, 13] (BCS theory, 1957) and of Bogoliubov [14] (1958) a systematic theory of superconductivity has been erected on this principle of attraction. It was shown that the ground state of such a system of interacting Fermi particles is located below the normal state with a filled Fermi sphere and, in consequence, it is separated from the excited states by an energy gap with a magnitude of the order of the coupling energy of an individual pair. Furthermore, the net attraction between electrons takes place inside an energy shell of order $k_B T_c$ around the Fermi surface, with T_c the superconducting transition temperature. For the elemental superconductors, like Aluminum (Al), Mercury (Hg), Niobium (Nb), Tin (Sn) and Lead (Pb), this coupling ranges up to about 1 meV, with a corresponding T_c up to about 10 K. An essential feature of the BCS theory is that all the Cooper pairs must behave in exactly the same way, which makes that they can be described by a single wave function. According to BCS theory: "The pairs should be chosen so that transitions between them are possible, i.e. they all have the same total momentum". As a best choice for the ground state pairing they took pairs with zero total momentum and opposite spin. The latter because exchange terms enhance the repulsive interaction for parallel spins. The Cooper pairs are located at the Fermi energy which is separated by an energy gap Δ from the quasiparticle states. The total gap between the (occupied) quasiparticle

spectrum below E_F and the (unoccupied) quasiparticle spectrum above E_F is $2\Delta \approx 3.5k_B T_c$. This approximation is valid in the weak coupling limit, which means superconductors for which $N_0 V < 0.3$ where N_0 is the normal density of states at the Fermi energy and V the attractive interaction. Most classical superconductors belong to this limit (Al has a bulk T_c of 1.2 K with $\Delta \sim 180 \mu\text{eV}$) but for example Pb with a bulk T_c of 7.2 K and $\Delta \sim 1.3 \text{ meV}$ does not. The left panel of Fig. 2.1 shows the pairing of states in k -space, for both a filled pair state ($|\mathbf{k}| > k_F$) and an empty pair state $|\mathbf{k}| < k_F$. The elementary excitations are broken paired states, which means that one of the two states of the paired state is occupied and one is empty. If $|\mathbf{k}| < k_F$ the excitation is hole-like in its behavior, while for $|\mathbf{k}| > k_F$ it is electron-like. The k -space represents only kinetic energy and thus the (potential) energy lowering of the paired states due to condensation is not "included". The paired states assemble in the condensate which is at the Fermi energy E_F while the excitations (broken states) occupy single electron states in the quasiparticle spectrum (right panel of Fig. 2.1, with $E_F = 0$). Electron-like excitations have $E > E_F$ and hole-like excitations have $E < E_F$. The Cooper pairs can be bro-

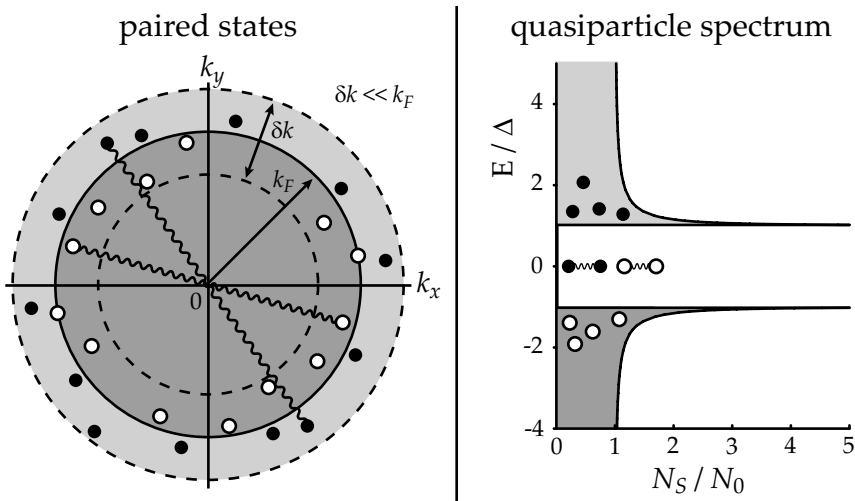


Figure 2.1: Pairing of states in k -space (left panel) and quasiparticle spectrum (right panel) for a BCS superconductor. The light/dark shaded areas represent empty/occupied states, the black/white dots represent electron/hole excitations and the wiggled lines represents the paired states. Left panel: The Fermi wave vector k_F is much larger than the shell δk around k_F where the pairing takes place (for clarity k_z is taken zero). Right panel: The density of states N_S is normalized to the normal state density of states N_0 , the energy E is normalized to the gap energy Δ , and the Fermi energy E_F is set to zero.

ken into excited states by temperature, but also by mechanisms that change the pairing itself. The Cooper pairs in a conventional bulk superconductor (s-wave, spin-singlet = BCS superconductor) consist of two electrons with opposite spin and momentum close to Fermi momentum. The Fermi spheres to which the two particles (\mathbf{k}, \uparrow) and ($-\mathbf{k}, \downarrow$) belong are identical, say symmetrical. Whenever this symmetry is lifted the Cooper pair starts to experience a pair breaking force, weakening the superconducting state. Two types of symmetry breaking effects are recognized. The orbital effect is related to a *shift* between the Fermi spheres, which happens if the one acquires a net momentum with respect to the other. The paramagnetic effect is related to a change in the *size* between the Fermi spheres, which translates to an exchange energy between the two spin states. The orbital effect is responsible for the limitation of the supercurrent density and magnetic flux expulsion. In terms of momentum \mathbf{p} the two electrons of the Cooper pair are (\mathbf{p}, \uparrow) and ($-\mathbf{p}, \downarrow$), but in the presence of an electromagnetic field described by the vector potential \mathbf{A} , the potential (or field) momentum $e\mathbf{A}/c$ needs to be added to the kinetic momentum $m\mathbf{v}$, with c the velocity of light. For the Cooper pair this results in ($\mathbf{p} + e\mathbf{A}/c, \uparrow$) and ($-\mathbf{p} + e\mathbf{A}/c, \downarrow$), which gives a total momentum of $2e\mathbf{A}/c$. The exerted Lorentz force is directed in opposite directions for the two electrons, trying to break the Cooper pair. Whenever the associated energy of the pair momentum exceeds the condensation energy, the Cooper pair is no longer a stable ground state. A transition from the superconducting state to the normal state by the orbital effect is essentially due to the kinetic energy of the pairs becoming larger than the condensation energy, while by the paramagnetic effect it is if the exchange energy becomes larger than the condensation energy.

The BCS Hamiltonian that describes superconductivity is valid for a superconductor in equilibrium at zero temperature in the absence of any interactions other than the attractive interaction that causes the formation of Cooper pairs. Using the creation and annihilation operators ($c_{k\sigma}^\dagger$ and $c_{k\sigma}$) for Bloch states specified by wave vector \mathbf{k} and spin σ , it can be expressed as:

$$\mathcal{H}_{\text{BCS}} = \sum_{k\sigma} \epsilon_k n_{k\sigma} + \sum_{kk'} V_{kk'} c_{k\uparrow}^\dagger c_{-k\downarrow}^\dagger c_{-k'\downarrow} c_{k'\uparrow} \quad (2.1)$$

where $n_{k\sigma} = c_{k\sigma}^\dagger c_{k\sigma}$ is the single-particle number operator (which counts the number of particles in a specific state), $\epsilon_k = \hbar^2 k^2 / (2m)$ is the corresponding (kinetic) energy with m the electron mass, measured with respect to the

momentum \mathbf{p} , velocity \mathbf{v} and wave vector \mathbf{k} are related by $\mathbf{p} = m\mathbf{v} = \hbar\mathbf{k}$

Fermi energy, and $V_{kk'}$ is the attractive interaction. The first term appearing in the Hamiltonian is the standard kinetic energy term, while the second term describes the scattering of a Cooper pair from state $(k' \uparrow, -k' \downarrow)$ to state $(k \uparrow, -k \downarrow)$ under the influence of the attractive interaction. In the BCS model, the attractive interaction is taken constant, $V_{kk'} = V$, for energies up to a certain cut-off energy (the Debye energy), otherwise it is zero. The Hamiltonian is accompanied by a self-consistency relation for the energy gap:

$$\frac{1}{\bar{V}} = \frac{1}{2} \sum_k \frac{1}{\sqrt{\Delta^2 + \epsilon_k^2}} \quad (2.2)$$

Solving the Hamiltonian for a certain potential V gives the eigenstates and eigenenergies of the superconductor. By inserting these into the self-consistency equation, the chosen potential V should be regained if the chosen value was correct. These two equations (Eq. 2.1, 2.2) form the basis for the modern description of superconductivity, which is written in the language of Green functions.

2.1.2 Bogoliubov-de Gennes equation

The BCS theory is written in (standard) single particle creation and annihilation operators for Bloch states specified by wave vector \mathbf{k} and spin σ . However, the elementary excitations of the superconductor are no longer the single particle states which we have for a normal metal, instead they are broken Cooper pair states. This makes the usage of the standard single particle creation and annihilation operators very cumbersome (for finite temperatures). A mathematical formulation based on the BCS theory was developed by Bogoliubov where he introduced the concept of coherent mixtures of particles and holes to describe a superconductor at finite temperatures. These mixed particle-hole excited states are known as Bogoliubons. The introduction of operators for these Bogoliubons has been generalized and evolved into what is now known as the Bogoliubov-deGennes (BdG) equation [15]. In this description, the standard momentum operators (k -space) have been replaced by field operators (real-space), which have the advantage that they are able to describe systems in which k is no longer a good quantum number and thus the eigenfunctions are no longer plane waves (dirty systems for example). The solutions (eigenfunctions) are given by an electron-like part, $\psi_e(r)$, and a hole-like part, $\psi_h(r)$, which have to be solved in a self-consistent manner fulfilling the gap equation. The Bogoliubov-deGennes equation can be expressed as:

$$\begin{pmatrix} H_0 & \Delta(r) \\ \Delta(r)^* & -H_0^* \end{pmatrix} \begin{pmatrix} \psi_e(r) \\ \psi_h(r) \end{pmatrix} = E \begin{pmatrix} \psi_e(r) \\ \psi_h(r) \end{pmatrix} \quad (2.3)$$

The Hamiltonian H_0 contains the kinetic energy term plus all interactions other than Δ (like the crystal potential and impurity potential). The $*$ symbol denoted the complex conjugate. Clearly, the coupling between electron and hole states exists for nonzero Δ only. One of the many applications of the BdG equations is the model of Blonder-Tinkham-Klapwijk [16] (BTK, 1982), which solves the BdG equations for an N/S interface with arbitrary interface barrier potential. They consider all possible reflection/transmission processes at the interface (normal reflection, Andreev reflection, normal transmission, branch-crossing transmission) and calculate the energy dependent transport probabilities, which allows for the calculation of current (I) - voltage (V) characteristics. While the BTK model seems the "end of the story" for N/S interfaces, in 1991 it was shown [17] that it breaks down when transport is dominated by impurity scattering. Strictly speaking, BTK remains correct but its validity becomes limited to the interface itself (which remains ballistic) and so loses its functionality for determining transport properties. So, although potentially the BdG model can deal with impurities, in real systems it is often still of not much use. This is because the positions (and therefore the potential) of the impurities are generally unknown, making it a serious difficulty to add the effects of scattering processes near the interface. This shifted the attention towards the usage of quasiclassical Green functions, which by then was already solidly formulated for about 20 years. The theoretical framework exhibits a higher complexity of mathematical concepts, but its functionality is more powerful. Currently, this framework is the modern way to describe superconductivity.

2.1.3 Green functions and the Gor'kov equation

A large amount of theoretical work has been done in describing superconductivity using quantum field theory, which had proved to be a very powerful and effective tool for microscopic theories of solid state systems (for a thorough description see for example [18, 19]). Green functions contain the information of the transport probabilities of single particles. They describe how particles propagate through the system influenced by all kind of interactions. Once the Green functions of a system are known, all single-particle properties of the system are known (for example, the density of states and electrical current) The single-particle normal Green function is defined by:

$$G_{\alpha\beta}(x, x') = -i \left\langle T_t \left(\psi_\alpha(x) \psi_\beta^\dagger(x') \right) \right\rangle_{st} \quad (2.4)$$

with $x = (\mathbf{r}, t)$ and $\psi_\alpha^\dagger(x)$ and $\psi_\alpha(x)$ are the time dependent electron creation and annihilation (Heisenberg) operators respectively, satisfying the usual

commutation rules for Fermi statistics. The Green function is a statistical average over all possible paths from x' to x , denoted by $\langle \dots \rangle_{\text{st}}$ and T_t is the time-ordering operator which orders the operators logically in time, giving a minus sign for each permutation. Effectively, the normal Green function $G_{\alpha\beta}(x, x')$ describes the movement of a particle from x' to x , or more precise, the probability amplitude for a particle to move coherently from x' to x , where β and α are the initial and final spin direction of the particle (the particle being an electron if $t > t'$ and a hole if $t < t'$). Note that the normal Green function depends on the standard electron operators and not on the quasiparticle operators introduced by Bogoliubov (to describe single-particle motion). The normal Green function is complemented by a Green function that describes the opposite movement:

$$\bar{G}_{\alpha\beta}(x, x') = -i \left\langle T_t \left(\psi_{\alpha}^{\dagger}(x) \psi_{\beta}(x') \right) \right\rangle_{\text{st}} \quad (2.5)$$

and they are related through $G_{\alpha\beta}(x, x')^* = -\bar{G}_{\alpha\beta}(x, x')$, where $*$ denotes the complex conjugate. In addition to the normal Green functions which describes coherent motion of single-particles (using single-particle electron states), a second type of Green function is needed to deal with the Cooper pairs, which occupy the paired states. These so-called anomalous Green functions are defined by:

$$\begin{aligned} F_{\alpha\beta}(x, x') &= -i \left\langle T_t \left(\psi_{\alpha}(x) \psi_{\beta}(x') \right) \right\rangle_{\text{st}} \\ \bar{F}_{\alpha\beta}(x, x') &= -i \left\langle T_t \left(\psi_{\alpha}^{\dagger}(x) \psi_{\beta}^{\dagger}(x') \right) \right\rangle_{\text{st}} \end{aligned} \quad (2.6)$$

and satisfy $F_{\alpha\beta}(x, x')^* = -\bar{F}_{\alpha\beta}(x, x')$. Clearly, $F_{\alpha\beta}(x, x')$ annihilates a Cooper pair (empties a Cooper pair state) and $\bar{F}_{\alpha\beta}(x, x')$ creating one (fills a Cooper pair state). Just as for the normal Green function, the transport nature is visible again as the highest probability to create(annihilate) a Cooper pair is at, or very near the position where the first(remaining) electron has coherently travelled to during the time interval from t' to t . Fig. 2.2 shows a graphical representation of the normal and anomalous Green function. Next to these real time Green functions, the imaginary time Matsubara Green function is often encountered in literature within the field of superconductivity. The Matsubara Green function is valid for systems in equilibrium (i.e. no potential differences) and has the advantage that at finite temperatures the ordering of the electron operators is still unambiguously defined. For the real-time Green functions special time ordering rules (Keldysh technique) are necessary (adding

$$\left\{ \psi_{\alpha}(x), \psi_{\beta}^{\dagger}(x') \right\} = \delta(x - x') \delta_{\alpha\beta} \text{ and } \left\{ \psi_{\alpha}(x), \psi_{\beta}(x') \right\} = \left\{ \psi_{\alpha}^{\dagger}(x), \psi_{\beta}^{\dagger}(x') \right\} = 0.$$

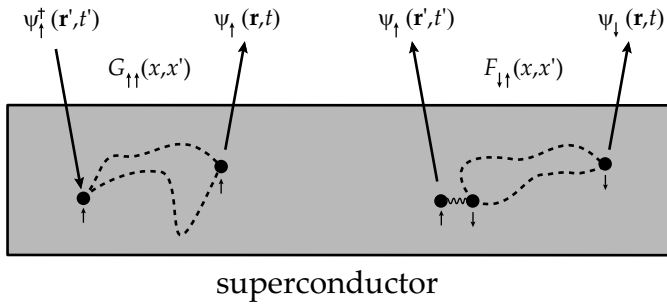


Figure 2.2: (Left) A spin up electron is added to the superconductor (location r' , time t') and at time $t > t'$ the probability to find that electron at location r is probed (where the electron could have taken any possible path from r' to r). This represents the normal Green function $G_{\uparrow\uparrow}(x, x')$. (Right) The spin up electron of a Cooper pair is taken out of the superconductor (location r' , time t') and at time $t > t'$ the probability to find the remaining electron of the Cooper pair is probed. This represents the anomalous Green function $F_{\downarrow\uparrow}(x, x')$.

to the mathematical complexity), but it is applicable to non-equilibrium systems as well. The anomalous Green functions describe the superconducting correlations and are related to the order parameter Δ of the superconductor. This order parameter is a measure for the strength of the superconducting energy gap and uses the same symbol. For an s-wave superconductor we have:

$$\begin{aligned}\Delta_{\alpha\beta}(x) &= -\lambda F_{\alpha\beta}(x, x) \\ \bar{\Delta}_{\alpha\beta}(x) &= -\lambda \bar{F}_{\alpha\beta}(x, x)\end{aligned}\quad (2.7)$$

where λ is the attractive interaction ($\lambda < 0$). Using the anti-commutation rules one can obtain: $\Delta_{\alpha\alpha}(x) = -\Delta_{\alpha\alpha}(x)$ and $\bar{\Delta}_{\alpha\alpha}(x) = -\bar{\Delta}_{\alpha\alpha}(x)$. As a consequence, the order parameter (for an s-wave superconductor) has to be zero for equal spin directions. Only the pairing of electrons/states with opposite spin directions contribute to the superconducting order parameter, which is a fundamental assumption within the BCS theory.

The Green functions can be conveniently written/ordered into 2×2 matrices in spin space, where the elements contain all possible spin combinations. The set of matrices that span the spin space are the Pauli spin matrices given by:

$$\sigma_0 = \begin{pmatrix} 1 & 0 \\ 0 & 1 \end{pmatrix}, \sigma_1 = \begin{pmatrix} 0 & 1 \\ 1 & 0 \end{pmatrix}, \sigma_2 = \begin{pmatrix} 0 & -i \\ i & 0 \end{pmatrix}, \sigma_3 = \begin{pmatrix} 1 & 0 \\ 0 & -1 \end{pmatrix} \quad (2.8)$$

where σ_0 is the unity matrix in spin space and $\sigma_i\sigma_i = \sigma_0$. For the normal Green function and the order parameter we write:

$$\hat{G}(x, x') = \begin{pmatrix} G_{\uparrow\uparrow}(x, x') & G_{\uparrow\downarrow}(x, x') \\ G_{\downarrow\uparrow}(x, x') & G_{\downarrow\downarrow}(x, x') \end{pmatrix}, \hat{\Delta}(x) = \begin{pmatrix} 0 & \Delta_{\uparrow\downarrow}(x) \\ \Delta_{\downarrow\uparrow}(x) & 0 \end{pmatrix} \quad (2.9)$$

Similar definitions hold for $\hat{G}(x, x')$, $\hat{F}(x, x')$, $\hat{F}(x, x')$ and $\hat{\Delta}(x)$. These (2×2) matrix Green functions can be further collected/ordered into a single (4×4) matrix Green function in the Nambu \otimes spin space, with \otimes the tensor product. In the Nambu space (particle-hole space) the Green functions are ordered based on the different combinations of electron/hole operators (ψ^\dagger creates an electron, ψ creates a hole). The elementary matrices of the Nambu space are identical to the ones that span the spin space, but now are denoted by τ_0 , τ_1 , τ_2 and τ_3 . The matrix Green functions \check{G} , \hat{G} , \hat{F} and \hat{F} each consist of a different combination of the two types of electron operators. The matrix Green function and matrix order parameter in Nambu \otimes spin space are written as:

$$\check{G}(x, x') = \begin{pmatrix} \hat{G}(x, x') & \hat{F}(x, x') \\ \hat{F}(x, x') & \hat{G}(x, x') \end{pmatrix}, \check{\Delta}(x) = \begin{pmatrix} 0 & \hat{\Delta}(x) \\ \hat{\Delta}(x) & 0 \end{pmatrix} \quad (2.10)$$

For stationary systems the Green functions no longer depend on the explicit time coordinates, but rather on the time difference between the two operations: $\check{G}(x, x') \rightarrow \check{G}(\mathbf{r}, \mathbf{r}', t - t')$. By making a Fourier transform over the time difference the energy dependent Green functions are obtained:

$$\check{G}(\mathbf{r}, \mathbf{r}', \epsilon) = \int e^{-i\epsilon(t-t')/\hbar} \check{G}(\mathbf{r}, \mathbf{r}', t, t') d(t - t') \quad (2.11)$$

with ϵ the energy of the single-particle (state). When using the imaginary time Matsubara Green functions this works out a bit different. The Matsubara Green functions are defined at the finite time interval: $-\frac{\hbar}{k_B T} < \tau - \tau' < \frac{\hbar}{k_B T}$, and as a result, the Fourier transformed Green functions are non-zero only for a discrete set of frequencies: $\hbar\omega_n = (2n+1)\pi k_B T$, where ω_n are the Matsubara frequencies. This series of frequencies continues up to the cut-off frequency ω_D , which is the Debye frequency. Just as within the BCS model where the Debye energy limits the range over which the attractive interaction is non-zero.

Gor'kov rewrote the original BCS Hamiltonian (Eq. 2.1) into an equation for the Green functions of the system [20]. In matrix form this equation takes a similar form as the BdG equations (Eq. 2.3) with the main difference that

the eigenstate functions of BdG are replaced by the Green functions of the system. Using the τ_i and σ_i matrices, the stationary Gor'kov equation can be expressed as:

$$(-\epsilon(\sigma_0 \otimes \tau_3) + H(\mathbf{r})(\sigma_0 \otimes \tau_0) - \check{\Delta}(\mathbf{r}))\check{G}(\mathbf{r}, \mathbf{r}', \epsilon) = \hbar\delta(\mathbf{r} - \mathbf{r}')(\sigma_0 \otimes \tau_0) \quad (2.12)$$

with $\delta(x)$ the Dirac delta function and $H(\mathbf{r}) = -\frac{\hbar^2}{2m}(\partial_{\mathbf{r}} + \frac{q}{i\hbar}\mathbf{A})^2 + q\varphi$ is the Hamiltonian of a particle (of mass m and charge q) in an electromagnetic field (with vector potential \mathbf{A} and scalar potential φ). Furthermore, $q\varphi = E_F - \mu$ is the energy difference between the Fermi energy and the chemical potential, and $\partial_{\mathbf{r}} \equiv \partial/\partial\mathbf{r}$. With this new set of equations, Gor'kov showed [21] that the famous phenomenological Ginzburg-Landau theory [22] can be microscopically derived from the BCS theory for temperatures close to the transition temperature. This is a solid proof for the "correctness" of the phenomenological Ginzburg-Landau model.

2.1.4 Quasiclassical approximation: Usadel equation

Cooper pairs are non-local objects and much larger (size is of order ξ_s) than the Fermi wavelength λ_F . Therefore, their transport properties (or Green functions) do not vary strongly on the scale of λ_F . This is the key to the quasiclassical approximation which greatly reduces the complexity of the Gor'kov equations. The approximation is based on the observation that the Green functions entering the Gor'kov equations contain (in most cases) fast oscillations on the scale of λ_F due to self-interference effects (like weak localization). These fast oscillations are all redundant information when interested in superconductivity, which only feels the average of such oscillations. The main idea of the quasiclassical approximation is that the relative coordinate of the Green functions $\rho = \mathbf{r} - \mathbf{r}'$ is responsible for the fast oscillations, while the center-of-mass coordinate $\mathbf{R} = (\mathbf{r} + \mathbf{r}')/2$, is responsible for the slow oscillations. Therefore, to lose the redundant information, one could average out the relative coordinate. A convenient way to do this is by first applying a Wigner transformation: $\mathbf{r} \rightarrow \mathbf{R} + \rho/2$ and $\mathbf{r}' \rightarrow \mathbf{R} - \rho/2$, which is an exact transformation to go from coordinates $(\mathbf{r}, \mathbf{r}')$ to (\mathbf{R}, ρ') . Next to make a Fourier transform over the relative coordinate (to separate the fast and slow oscillations in the obtained spectrum) resulting in the relative momentum \mathbf{p} , and finally to integrate over the magnitude of the momentum. The precise definition of the quasiclassical Green functions, defined through the Gor'kov

Green functions, reads:

$$\check{g}(\mathbf{R}, \hat{\mathbf{p}}, \epsilon) = \frac{i}{\pi} \int d\xi_p \int d(\mathbf{r} - \mathbf{r}') \check{G}(\mathbf{r}, \mathbf{r}', \epsilon) e^{-i\hat{\mathbf{p}} \cdot (\mathbf{r} - \mathbf{r}')/\hbar} \quad (2.13)$$

where $\hat{\mathbf{p}} = \mathbf{p}/p$ is the unit vector in the direction of momentum (p is the momentum magnitude) and ξ_p is the kinetic energy variable which is connected to the momentum: $\xi_p = v_F(p - p_F)$, where $p_F = mv_F$ is the Fermi momentum and v_F the Fermi velocity. Application of this quasiclassical approximation on the Gor'kov equation (Eq. 2.12) leads to the Eilenberger equation [23], which in the absence of electromagnetic fields is written as:

$$-i\hbar\mathbf{v}_F\partial_{\mathbf{R}}\check{g} - [\epsilon(\sigma_0 \otimes \tau_3) + \check{\Delta}, \check{g}] = [\check{\Sigma}, \check{g}] \quad (2.14)$$

where the commutator of two elements $[a, b] = ab - ba$, and we used that $v_F\hat{\mathbf{p}} = \mathbf{v}_F$. Furthermore, $\check{g}(\mathbf{R}, \hat{\mathbf{p}}, \epsilon)$ and $\check{\Delta}(\mathbf{R})$ are the quasiclassical variants of Eq. 2.10 and the right-hand-side of the Eilenberger equation adds the effect of self-energies (see below). The Eilenberger equation is called quasiclassical since it describes the system using a mixture of classical and quantum mechanics. It uses the quantum mechanical field operators to find the probability amplitudes (the Green functions) of the motion of classical particles with velocity v_F and direction $\hat{\mathbf{p}}$.

The presented form of the Gor'kov equation (Eq. 2.12) does not contain any interaction term other than the attractive interaction responsible for superconductivity. Taking $\Delta = 0$ (or $T > T_c$) makes it a normal metal and one could say the Green functions are now all of "non-interacting" types. In general, the Green functions are complemented by something called self-energy, usually denoted by Σ . Loosely speaking, the self-energy dresses up the non-interacting Green function by adding the effects of other interactions, such as electron-electron interactions, electron-phonon interactions and impurity scattering. The resulting Green function is then the "real" Green function of the system. In general, the self-energy is a complex function with the real part describing the change in energy (which is a renormalization of mass) and the imaginary part describing the lifetime of the energy state. Since Σ describes the changes of electron states, it depends on Green functions having equal coordinates i.e. $\Sigma_{\alpha\beta}(x) \propto G_{\alpha\beta}(x, x)$. Comparing Σ to Δ (see Eq. 2.7) we can say that Δ is the anomalous equivalent of the self-energies, but now associated with a two-particle state. The interactions of importance are the interactions between or with quasiparticles (the elementary excitations). These interactions are responsible for the relaxation of the system to an equilibrium state, where it is assumed that the crystal lattice (phonons + impurities) itself is already in

equilibrium and forms a heat bath. The main contributions to the relaxation (in descending order of importance) are scattering with impurities (both non-magnetic and magnetic), electron-phonon interactions and electron-electron interactions. A powerful method to incorporate the interaction between electrons and random impurities has been developed by Abrikosov and Gor'kov [24]. It is assumed that physical properties of superconductors containing a large amount of random impurities can be obtained by averaging over realizations of the disordered impurity potentials. A second assumption is the Born approximation, which implies that the scattering potential is small compared to the characteristic atomic potential (which is of the order of the Fermi energy). For isotropic scattering (there is no preferred direction to scatter into, and the dependence on $\hat{\mathbf{p}}$ is lost) the self-energy becomes:

$$\check{\Sigma}(\mathbf{R}, \epsilon) = \frac{i\hbar}{2\tau_{\text{imp}}} \langle \check{g}(\mathbf{R}, \hat{\mathbf{p}}_1, \epsilon) \rangle_{\mathbf{p}_1} + \frac{i\hbar}{2\tau_{\text{sf}}} (\sigma_3 \otimes \tau_0) \langle \check{g}(\mathbf{R}, \hat{\mathbf{p}}_1, \epsilon) \rangle_{\mathbf{p}_1} (\sigma_3 \otimes \tau_0) \quad (2.15)$$

where the momentum average $\langle A(\hat{\mathbf{p}}) \rangle_{\mathbf{p}} = \int A(\hat{\mathbf{p}}) \frac{d\Omega_{\mathbf{p}}}{4\pi}$. Furthermore, τ_{imp} and τ_{sf} are the scattering times for scattering at non-magnetic impurities and magnetic impurities respectively. The first term thus describes non-magnetic impurity scattering while the second describes the magnetic impurity scattering.

When a material is in the dirty limit, a particle scatters a lot of times before losing its phase coherence and this results in the loss of the initial momentum direction. The Green functions, which describe the electron and hole motion, become nearly isotropic in this limit. In a first approximation, they no longer depend on momentum directions and the first-order correction is linear in $\hat{\mathbf{p}}$, which is the unit vector in the direction of momentum (and is equal to $\hat{\mathbf{v}}_F$). For the quasiclassical Green functions in the dirty limit we write:

$$\check{g}(\mathbf{R}, \hat{\mathbf{p}}, \epsilon) = \check{g}_0(\mathbf{R}, \epsilon) + \hat{\mathbf{p}}\check{\mathbf{g}} \quad (2.16)$$

where both the isotropic part \check{g}_0 and the correction $\check{\mathbf{g}}$ do not depend on the direction of momentum. Furthermore $|\check{\mathbf{g}}| \ll \check{g}_0$ and the normalization condition $\check{g}^2 = \check{1}$ applies. Inserting this expansion into the Eilenberger equation and averaging over momentum directions results in the Usadel equation [25], which is fully isotropic. For the stationary system, in the absence of electromagnetic fields, it reads:

$$i\hbar D \partial_{\mathbf{R}} (\check{g}_0 \partial_{\mathbf{R}} \check{g}_0) - [\check{\Delta} + \epsilon (\sigma_0 \otimes \tau_3), \check{g}_0] = [\check{\Sigma}_{sf}, \check{g}_0] \quad (2.17)$$

Where $\check{\Sigma}_{sf}(\mathbf{R}, \epsilon) = \frac{i\hbar}{2\tau_{\text{sf}}} (\sigma_3 \otimes \tau_0) \check{g}_0(\mathbf{R}, \epsilon) (\sigma_3 \otimes \tau_0)$ and we used that the diffusion constant D is coupled to the Fermi velocity and the elastic mean free

path by $D = \frac{1}{3}v_F\ell_e$ where the elastic mean free path $\ell_e = v_F\tau_{\text{imp}}$. From the scattering at impurities, only the magnetic impurity term remains, which acts as pair breaker. The matrix Green function $\check{g}_0(\mathbf{R}, \epsilon)$ and $\check{\Delta}(\mathbf{R})$ have the usual form in Nambu \otimes spin space.

An important limitation of the quasiclassical approximation is the inability to account for different (non-identical) spin bands with different Fermi velocities, as it poses problems to make the integration over $d\xi_p$. As a result, identical spin bands are used, which in general is correct for normal metals and superconductors. However, for a ferromagnet such a model can only be correct if the spin polarization is about zero. This, in combination with the general limitation of correlations between particles separated by energies of the order E_F , is the weak ferromagnetic limit. It has $E_{\text{ex}} \ll E_F$ and a polarization of 0%. A weak ferromagnet is treated as a normal metal with the inclusion of a small exchange field. The strong ferromagnetic limit is when $E_{\text{ex}} \sim E_F$, and usually the polarization is no longer close to zero. The incapability of dealing with non-identical spin bands does not mean that the model cannot treat spin dependent interactions. In fact, the attractive interaction itself depends on spin directions, and also spin-flip processes were already included. As long as the spin dependent interactions are not caused by non-identical spin bands, they can be included in the Hamiltonian.

For spin independent systems a simplification is possible, which comes down to dropping the spin space ordering. Such systems do not contain any coherent spin dependent interactions at all (i.e. changing the spin direction of a particle without disturbing its energy), however, they do include for example spin scattering which randomizes spin. In this case, several components of the Green functions will vanish. For the normal Green functions, components with opposite spin directions vanish while for the anomalous Green functions the components having equal spin directions vanish. The reason for this is that there are no interactions to coherently flip the spin of a particle. For a single particle (normal Green function) this means that a non-zero probability amplitude is only possible if the particle stays in a single spin band. It also means that for a Cooper pair the correlation exists only between opposite spin directions (pairing only occurs between opposite spin directions, and an electron of the Cooper pair cannot flip its spin coherently to create a correlation between equal spin directions). For the non-zero Green functions we get: $G_{\uparrow\uparrow} = G_{\downarrow\downarrow} = G$ and $\overline{G}_{\uparrow\uparrow} = \overline{G}_{\downarrow\downarrow} = \overline{G}$ (the two spin bands are identical). For the anomalous Green functions we get: $F_{\uparrow\downarrow} = -F_{\downarrow\uparrow} = F$ and $\overline{F}_{\uparrow\downarrow} = -\overline{F}_{\downarrow\uparrow} = \overline{F}$. The matrix Green function and order parameter in Nambu \otimes spin space now

reduce to:

$$\check{g}_0 = \begin{pmatrix} G\sigma_0 & iF\sigma_2 \\ i\bar{F}\sigma_2 & \bar{G}\sigma_0 \end{pmatrix}, \quad \check{\Delta} = \begin{pmatrix} 0 & i\Delta\sigma_2 \\ i\bar{\Delta}\sigma_2 & 0 \end{pmatrix}, \quad (2.18)$$

while for the spin-flip self-energy matrix we find:

$$\check{\Sigma}_{\text{sf}} = \frac{i\hbar}{2\tau_{\text{sf}}} \begin{pmatrix} G\sigma_0 & -iF\sigma_2 \\ -i\bar{F}\sigma_2 & G\sigma_0 \end{pmatrix} \quad (2.19)$$

We see that the Nambu space matrices all have a σ_0 spin symmetry on the diagonal and a σ_2 spin symmetry on the off-diagonal. Multiplication of two such matrices results in a matrix having the same spin symmetry, therefore the spin space effectively drops out of the equations. We then find for the spin independent Usadel equation, using now the $\hat{}$ notation for the 2×2 matrix in Nambu space:

$$i\hbar D\partial_{\mathbf{R}}(\hat{g}_0\partial_{\mathbf{R}}\hat{g}_0) - \left[\hat{\Delta}(\mathbf{R}) + \epsilon\tau_3, \hat{g}_0 \right] = \left[\hat{\Sigma}_{\text{sf}}, \hat{g}_0 \right] \quad (2.20)$$

with:

$$\hat{g}_0 = \begin{pmatrix} G & iF \\ i\bar{F} & \bar{G} \end{pmatrix}, \quad \hat{\Delta} = \begin{pmatrix} 0 & i\Delta \\ i\bar{\Delta} & 0 \end{pmatrix}, \quad \hat{\Sigma}_{\text{sf}} = \frac{i\hbar}{2\tau_{\text{sf}}} \tau_3 \hat{g}_0 \tau_3 \quad (2.21)$$

The self-consistency relation for Δ as well as the special boundary condition necessary to describe interfaces between materials are given in Chapter 7.

2.1.5 Unconventional Cooper pairs

Stimulated by the observation or idea that the 3-Helium superfluid state should have a p-wave orbital state (below 0.07 K) the BCS theory has been generalized for non-zero orbital angular momentum. First in the works of Anderson and Morel [26] and improved by Balian and Werthamer [27] (see Leggett's nobel lecture for a review [28]). A condensation of pairs into $\ell = 1$ or higher states can become favorable when for example there is a strong short-range repulsion preventing condensation into the s-wave configuration, which is the case for the 3-Helium superfluid. Because a Cooper pair consists of two Fermi particles and obeys Fermi statistics, an anti-symmetric wave function is required under the exchange of the two particles (the Pauli principle). This puts restraints on the possible types of pairing (i.e. the possible combinations of orbital and spin states). The orbital state is symmetric if the orbital quantum number

in this thesis we use $\hat{}$, $\check{}$ and $\tilde{}$ to respectively denote a 2×2 , 4×4 and 8×8 matrix

$\ell = 0, 2, \dots$ (even) and anti-symmetric if $\ell = 1, 3, \dots$ (odd). The $\ell = 0, 1, 2$ are the s-, p- and d-wave respectively. The spin state of a pair is either in the symmetrical spin singlet state ($S=0$) or in the anti-symmetrical spin triplet state ($S=1$). The implication of this is that pairs in s- or d-wave orbital states should be in spin singlet states, while pairs in p-wave orbital state should be in spin triplet states.

An important difference between s-, p- and d-wave is that only in case of pairing into s-wave orbital states, the superconducting energy gap is isotropic. It does not depend on momentum \mathbf{k} and no single particle states exist for energies within the gap region. This makes the s-wave superconductor robust against impurity scattering because there are no available normal electron states which can "absorb" a pair after scattering at an impurity. However, when we consider a p- or d-wave orbital state, the energy gap is no longer isotropic. This means that for a certain absolute value of k (with energy ε_k), some directions have a full or reduced gap, while other direction don't have a gap at all. As a result, the density of single particle states becomes non-zero (and non-constant) for energies inside the gap region. These superconductors are not robust against impurity scattering and only survive in clean systems, where the superconducting coherence length is (much) smaller than the elastic mean free path. The Cooper pairs as suggested by BCS theory are in a spin singlet state with s-wave orbital state, which is called conventional superconductivity. Triplet superconductivity in conventional thin film superconductors thus seems a non-existing phenomena, and yet it was recently measured in experiments of Keizer *et al.* [29] en Sosnin *et al.* [30]. In the first, triplet pairing was induced in the half-metallic ferromagnet CrO_2 (100 % spin polarized material), while in the latter is was induced in Holmium (Ho) which is a conical ferromagnet. Somehow the above discussion about the possible combinations between orbital and spin states is circumvented. The answer to this lies in the time coordinate/symmetry which thus far was not really taken into account. If the time dependent part of the Cooper pair wave function is anti-symmetric under the exchange of the two particles, a s-wave spin-triplet pairing becomes possible [31]. This mechanism should also allow for p-wave singlets, but they have not been observed (yet).

Another type of unconventional superconductivity is what is now known as the LOFF state, named after Fulde and Ferrell (1964) [32] and Larkin and Ovchinnikov (1964) [33] whom considered this situation for the first time. The LOFF state is an inhomogeneous superconducting state, where the two single electron states forming the paired-state belong to different Fermi surfaces.

This difference between the Fermi surfaces for the two spin bands is (in the model systems) created by a homogeneous exchange field generated by polarized magnetic impurities, making the LOFF state a display for the coexistence of ferromagnetism and superconductivity. The parameter which determines if the LOFF state is viable is the strength of the exchange field compared to the condensation energy (the paramagnetic effect). Unlike the conventional BCS state, the Cooper pairs in the LOFF state have acquired a non-zero total momentum. This gives rise to a spatially varying Cooper pair density (and gap potential). Electronegativity is maintained by the normal electrons created from the breaking of pairs (which is the cause for the density changes). The description of the LOFF state is very similar to the induced superconductivity (or proximity effect) in S/F junctions.

2.2 Fundamentals of ferromagnetism

In our experimental works the ferromagnets are "used" for their exchange field to investigate their interaction with superconductivity. In this section a brief description of magnetism is given, focussed on the type and appearance it takes in our devices (see ref [34] for a more detailed description).

Magnetism is a phenomenon encountered in nature, for example it is found in the magnetic mineral Fe_3O_4 (known as Magnetite). Magnetism is well integrated in nowadays technology, especially in the area of digital data storage. The strength of magnetism, or actually, the magnetic induction or magnetic flux density, is expressed in Tesla. The earth's field is around 30-50 μT at the surface, which is very weak compared to magnetic materials which can have surface strengths up to 1 or 2 Tesla. A magnetic field can be connected to electrical currents. These can be macroscopic, as e.g. utilized in electromagnetic coils. In superconductors, macroscopic screening currents are able to expel magnetic flux from its interior. They can also be microscopic, and it are the atomic electrical currents together with the magnetic moments connected to the electron spin, which lead to the magnetization of matter.

Whenever a piece of material is put into a magnetic field, the electron spin and its associated magnetic moments will start to align with the field, which behavior is know as paramagnetism (it typically only involves a small fraction of the electrons and the induced field is rather weak). However, only few materials show a spontaneous alignment of the spins in the absence of external magnetic fields. This phenomenon is another display of a condensed state of the electrons, just as superconductivity is. Again, the ordering appears *below* a

certain critical temperature, while *above* this temperature the directions of the magnetic moments randomize resulting in a zero net magnetization. Different types of magnetic alignment exist. In a ferromagnetic material, the alignment is parallel and the critical temperature is called the Curie temperature T_C . In an antiferromagnetic material the alignment is perfectly antiparallel and the critical temperature is called the Néel temperature T_N . All the alignments in between are the ferrimagnetic materials.

All materials are built up from atoms, which consist of a positively charged core of protons and neutrons with negatively charged electrons orbiting around it. Both the electron cloud and the nucleus carry an intrinsic magnetic moment, but in general the magnetic moment of the nucleus is much smaller than that of the electrons, and therefore we narrow down the discussion to the electron part. In isolated atoms, incompletely filled electronic shells carry both an orbital angular momentum and a spin angular momentum, and therefore a magnetic moment. As long as the orbits do not overlap, these "local moments" also occur in solids matter, but we shall not be concerned with such magnetism either. Instead, we focus on so-called band ferromagnets, which are found in particular in alloys of 3d-transition metals (Ti, V, Cr, Mn, Fe, Co, Ni and Cu). In a band ferromagnet, the two spin bands are asymmetrically as depicted in Fig. 2.3. Where in the normal metal (in the ground state) both spin bands are filled up to the Fermi energy E_F and contain an equally number of electrons. In case of a ferromagnet one spin band (majority band) contains more electrons n_\uparrow and is filled up to a higher energy level compared to the other spin band (minority band), which contains n_\downarrow electrons. The energy of the electron states are now given by $\epsilon_{\uparrow,\downarrow}(k) = \epsilon_0(k) - I \frac{n_{\uparrow,\downarrow}}{n}$ with I a measure for the exchange correlation and $n = n_\uparrow + n_\downarrow$. In this new state, the kinetic

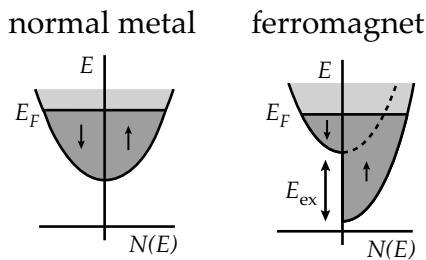


Figure 2.3: Filling of the density of states $N(E)$ of the two spin bands for a normal metal and a ferromagnet, with E_F the Fermi energy and E_{ex} the exchange energy

energy has increased (electrons originally occupying states with $k < k_F$ now occupy states with $k > k_F$, increasing the kinetic energy $\propto k^2$). However, the

potential energy has decreased (with less degenerate states doubly occupied, the total spatially overlap of electron states has reduced, which reduces the Coulomb repulsion energy). This new state is stable if the potential energy decrease is larger than the kinetic energy increase. This leads to the Stoner criterium for ferromagnetism to occur: $N(E_F) I > 1$, with $N(E_F)$ the density of states at the Fermi energy.

2.2.1 Magnetic domains and switching

A ferromagnet at a temperature below its Curie temperature thus shows spontaneous magnetization. However, the magnetization is not necessarily homogeneous. Moreover, the net magnetization of a ferromagnet (in absence of any field) is usually close to zero! Energetically there is a strong preference

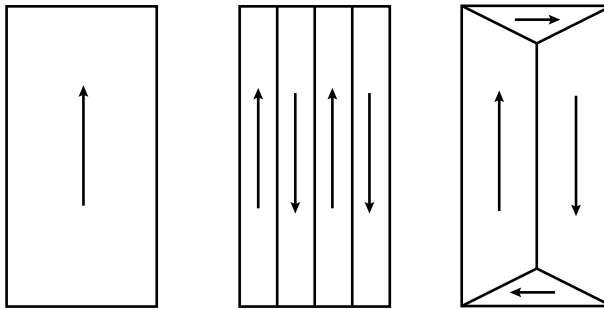


Figure 2.4: Different possible domain configurations in a ferromagnet, with from left to right a decrease of the induced field outside the ferromagnet.

to keep the magnetization inside the material, and this typically leads to the formation of domains (see Fig. 2.4). Each domain has a single orientation of the magnetization vector and the domains are separated by domain walls, which have typically a much smaller lateral dimension. In the domain wall, the magnetization vector rotates from the direction of the domain on the one side to the direction of the domain on the other side. Two main classes of domain walls are distinguished (see Fig. 2.5). In Bloch walls the rotation goes out-of-plane, while in Néel walls it goes in-plane (where the plane is spanned by the two magnetization vectors). Other more complex rotations exist, but are always a combination of the Bloch and Néel type.

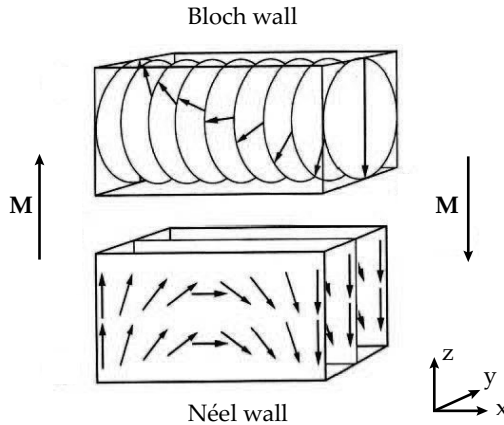


Figure 2.5: Rotation of the magnetization vector \mathbf{M} in an out-of-plane Bloch domain wall (top) and an in-plane Néel domain wall (bottom)

The appearance of the domain configuration is the result of minimizing the total energy of the system. For a ferromagnet, the following terms are to be considered. The *exchange energy* (E_{ex}) relates to the interaction between electron spins and is minimized for parallel alignment of the spins. The *Zeeman energy* (E_{H}) relates to the direction of the magnetization with respect to the external field. It minimizes for parallel alignment. The *crystalline anisotropy energy* (E_{ca}) relates to the direction of the magnetization with respect to the lattice orientation (it is minimized for alignment with the so-called lattice easy-axes). The *magnetostatic (or demagnetization) energy* (E_{D}) is an effect of the dipole fields and therefore connected to the shape of the ferromagnet. It is minimized by keeping flux inside the ferromagnet (or inducing a lowest field outside the ferromagnet). The demagnetization energy is responsible for the presence of domains, while the competition between the exchange energy and crystalline anisotropy energy determines the width of the domain walls. The first favors a (infinitely) broad wall, while the latter favors a thin as possible wall. When the sample dimension becomes of the order of the typical domain sizes, which are usually in the μm range, the shape anisotropy becomes the dominant energy term (because it cannot become lower anymore by making domains), especially in elongated shapes. For a long and thin wire, this often leads to a magnetization aligned with the wire direction. The actual magnetic configuration in the ferromagnet is coupled to an external magnetic field (\mathbf{H}) through the Zeeman term. Whenever this field \mathbf{H} increases or decreases, the magnetic configuration in the ferromagnet usually changes as well, leading to a change in the (average) magnetization vector \mathbf{M} . Fig. 2.6 illustrates this

behavior, where the origin gives the initial state of the ferromagnet (practically zero net magnetization). The curve then passes the points a to f in alphabetic order and ends up again in point a. The foremost characteristic of this curve is that it shows hysteresis (i.e. there is a difference in the path for going up and down in field), and it is generally known as the hysteresis curve. For high enough (absolute) field, the ferromagnet saturates. It has become a single domain, with its magnetization vector pointing along the applied field. Points b and e are the remanent (or residual) magnetization points. After being (partly) saturated once, the ferromagnet now shows a significant magnetization in zero applied field. Points c and f are the coercive field points. They indicate the field required to return to a net magnetization of zero, or, to change the direction of magnetization. The hysteresis curve shows, for the chosen direction of applied field, what field strengths are required to fully magnetize the ferromagnet. It also shows over which field range there is a presence of magnetic domains, and it shows how "easy" or "hard" it is to magnetize along the chosen direction. An easy direction result in a squarish hysteresis curve, with the remanent field values close to the saturation values. For a hard direction the remanent field values are much reduced (points b and e close to 0) and the hysteresis curve starts to close.

Being two very different phenomena, antagonistic even, because the superconductor tries to expel any magnetic field from its interior. The two states are very similar at the same time. Both superconductivity and ferromagnetism are mean field orders of electron spins, parameterized by Δ and E_{ex} respectively. Both orders appear below a certain critical temperature and change the normal metal density of states near the Fermi energy. However, the ferromagnetic density of states is (usually) just an energy shifted version of the normal density of states and the charge, energy and spin transport are governed by normal electrons. The superconductor is much more special in this aspect, as now a gap region has appeared near the Fermi energy. Charge transport is now governed by Cooper pair, which don't transport any heat (the energy is always the Fermi energy, no extra energy can be carried by the Cooper pair), and only the non conventional types can carry spin. Ferromagnetism is an ordering/allignment of electron spin such that one spin band contains more filled states (the majority band) and one contains less filled states (the minority band). As a result, there is a polarization of the electron spin and a potential (and kinetic) energy difference between the two spin bands. In the conventional superconductor, the spin ordering goes in k-space, and in real space no differences exists between the two spin populations.

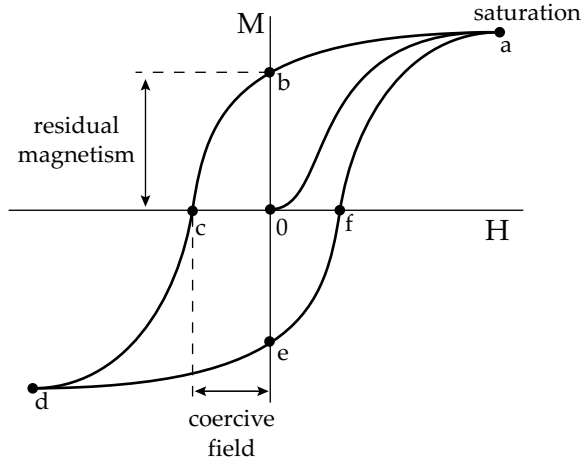


Figure 2.6: Hysteresis curve showing saturation magnetization (points a and d) re-magnetization (points b and e) and coercive fields (points c and f).

2.3 Proximity effect

2.3.1 Proximity effect in S/N

Although Cooper pairs are only generated inside a superconductor (for $T < T_c$), they are not confined to the interior of the superconductor itself. In a junction between a superconductor (S) and a normal metal (N) Cooper pairs can move from S to N, inducing superconducting properties into the normal metal. This is called the (superconducting) proximity effect. At first sight, this proximity effect does not seem possible as the Cooper pairs are not eigenfunctions of any non-superconducting material. Besides that, normal electron transport is blocked by the energy gap for all energies close to the Fermi energy. However, a unique mechanism exists that allows for the transfer of a Cooper pair from S to N (and visa versa). This process is the Andreev reflection [35] and is depicted in Fig. 2.7 (right panel). An incoming (excited) electron at energy $\epsilon < \Delta$ reaches the S/N interface. But, instead of being reflected it drags along a second electron at energy $-\epsilon$, with opposite direction of momentum and spin, to enter the superconductor as a Cooper pair. This

second electron is taken from the valence band and consequently leaves a hole behind. This hole then travels back along the path of the original incoming electron because it has opposite direction of momentum. The reverse mech-

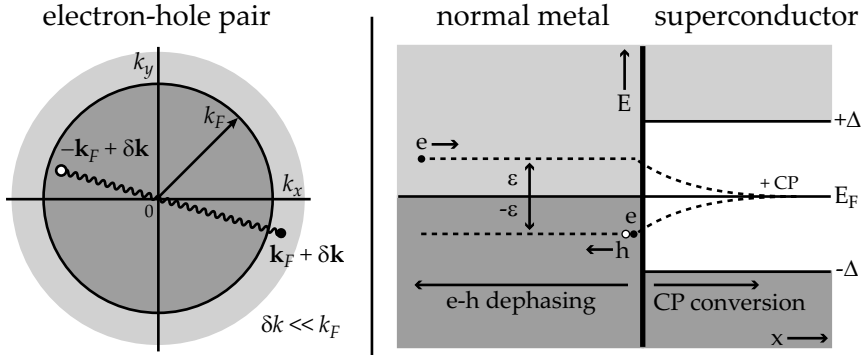


Figure 2.7: The right panel shows the Andreev reflection at a normal metal - superconductor interface. Upon reaching the interface, the incoming electron at energy ϵ causes a hole reflection at energy $-\epsilon$ (together they form the correlated electron-hole pair). The incoming electron itself and the missing electron in the valence band have entered the superconductor where they are converted into a Cooper pair. The left panel shows the correlated electron-hole in k -space.

anism takes place as well. In that case the incoming particle is a hole in the valence band (energy $-\epsilon$), which upon arriving at the interface pulls a Cooper pair out of the condensate. One of the electrons occupies the hole, while the other electron occupies an excited state in the conduction band (energy ϵ , with opposite direction of momentum and spin compared to the incoming hole) and travels back along the path of the original incoming hole. The net result of an Andreev reflection is thus a charge transfer of $-2e$ from N to S. No excessive energy is transferred as in N the electron excitation is swapped for an energy-equivalent hole excitation, while in S the Cooper pair is simply added to the condensate (the ground state). The Andreev reflection is thus purely a transfer of charge.

The induced electron-hole pair in N carries superconducting properties along the path of travelling. It is a Cooper pair no longer bound together by the attractive interaction. However, the two electrons that form the Cooper pair through Andreev reflection (and consequently the induced electron-hole pair) do not necessarily have exactly opposite momentum. The electron from the conduction band has $\mathbf{k}_F + \delta\mathbf{k}$, while the electron from the valence band has $-\mathbf{k}_F + \delta\mathbf{k}$ (Fig. 2.7, left panel). This sums up to a net momentum of

$2\delta k \sim \frac{\epsilon}{\epsilon_F} k_F \ll k_F$. The result of this k-vector mismatch is that the induced pair dephases, even in the absence of pair breaking mechanisms. Only a correlated pair at the Fermi energy ($\delta\mathbf{k} = 0$) can escape from this dephasing. In case of diffusive systems, the dephasing time corresponds to a travelling distance represented by the (energy averaged) coherence length $\xi_N = \sqrt{(\hbar D_N / (k_B T))} = \int \xi_N(\epsilon) d\epsilon$, with D_N the normal metal diffusion constant and T the temperature, which is taken as the primary source of dephasing. Other sources of dephasing, such as inelastic processes and magnetic fields, will only shorten this coherence length. At the Fermi energy, $\xi_N(\epsilon)$ goes to infinity, while for increasing energy this length becomes shorter. This is why for $T \rightarrow 0$, $\xi_N \rightarrow \infty$ as the only possible excitations at zero temperature are located at the Fermi energy. In reality, the coherence length will still be finite (but pretty long) due to the other forms of dephasing. In S a Cooper pair is being constructed (deconstructed) from (into) the two electrons from N. This conversion also takes place over a certain distance, which is the superconducting coherence length $\xi_S = \sqrt{(\hbar D_S / (k_B T_c))}$ with D_S the superconductor diffusion constant (also for diffusive systems). Although ξ_S varies per material, it is typically in the range from 10 nm to 1 μm . This is also the typical range for ξ_N , unless the temperature is close to zero (for conventional superconductors this means at least $T < 1$ K).

2.3.2 Proximity effect in S/F

When the normal metal is replaced by a ferromagnet (F), the effects of a non-zero spin polarization \mathbf{P} and exchange energy E_{ex} have to be included. One consequence is a reduction of the Andreev reflections as the mechanism becomes limited by the minority spin band [36]. In case of 100% spin polarization, the Andreev reflection even becomes fully blocked due to absence of a complete spin band. In the presence of an (elastic) spin-rotation/flip mechanism at the interface, this blocking can be partially circumvented as this effectively allows for Andreev reflection using a single spin band. A second consequence is that the induced electron-hole pair experiences the exchange splitting of the spin bands in the ferromagnet. There is a potential energy difference between spin up direction and spin down direction of an electron (which is at a fixed total energy). The minority spin band has an increased potential energy, which means that at a certain energy level (total energy), for example the Fermi energy, the kinetic energy of an electron in the minority spin band is lower compared to the majority spin band. As a result the Cooper pair acquires a net momentum which leads to an oscillation on top of

using $2m(\epsilon_F + \epsilon) = \hbar^2(k_F + \delta k)^2$ and $\epsilon \ll \epsilon_F$

an exponential decay (see Fig. 1.3), as was shown by Demler and co-workers [37]. The length scales involved are in general much smaller than the "standard decay" (as in S/N) because the exchange energy is usually much higher than the superconductor transition temperature. As an alternative approach to examine the effect of the exchange field on the spin singlet state, we use the Dirac notation and write for the singlet (Ψ^s) and triplet ($\Psi_0^t, \Psi_{-1}^t, \Psi_{+1}^t$) states:

$$\begin{aligned}
 \Psi^s &= \langle \uparrow | \downarrow \rangle - \langle \downarrow | \uparrow \rangle \\
 \Psi_0^t &= \langle \uparrow | \downarrow \rangle + \langle \downarrow | \uparrow \rangle \\
 \Psi_{-1}^t &= \langle \downarrow | \downarrow \rangle \\
 \Psi_{+1}^t &= \langle \uparrow | \uparrow \rangle
 \end{aligned} \tag{2.22}$$

where $|\uparrow\rangle$ and $|\downarrow\rangle$ represent the spin up and spin down state (at fixed energy). In the presence of the exchange energy E_{ex} , the momentum of the electron in the minority (spin down) band is decreased. As a result the spin down state changes into:

$$\begin{aligned}
 |\downarrow\rangle &\rightarrow |\downarrow\rangle \times e^{(-itE_{\text{ex}}/h)} \\
 \langle \downarrow | &\rightarrow \langle \downarrow | \times e^{(+itE_{\text{ex}}/h)}
 \end{aligned} \tag{2.23}$$

The Cooper pair in the spin singlet state then changes as follows:

$$\begin{aligned}
 \Psi^s &= \langle \uparrow | \downarrow \rangle e^{-itE_{\text{ex}}/h} - \langle \downarrow | \uparrow \rangle e^{+itE_{\text{ex}}/h} \\
 &= \Psi^s \times \cos(tE_{\text{ex}}/h) - \Psi_0^t \times i \sin(tE_{\text{ex}}/h)
 \end{aligned} \tag{2.24}$$

The amplitude of the singlet state follows indeed an oscillation, and it also shows that the nature of the oscillation is actually a change into the triplet component Ψ_0^t . The period of this oscillation $T = 2\pi\hbar/E_{\text{ex}}$, which in a diffusive system (diffusion constant D_F) corresponds to a length of $\sqrt{D_F T} = 2\pi\sqrt{\hbar D_F/E_{\text{ex}}} = 2\pi\xi_F$. The definition for the ferromagnetic coherence length ξ_F is similar to its normal and superconducting counter parts, except that each coherence length is based on the dominating energy term of the system. When, for example, the temperature is of the same order as the exchange energy, the temperature has to be added to ξ_F . The presence of a homogeneous exchange field thus leads to the appearance of correlated spin triplet pairs. However, only one out of the three spin triplets appears, and since it still consists of both spin directions, the ferromagnet breaks it down just as easy as the conventional singlet pairs. The other two, the spin equal triplets, are generate from the Ψ_0^t triplet once it experiences multiple directions of the exchange field [38, 39]. These "multiple directions" actually means inhomogeneous magnetism, which for example can come from magnetic domains or

magnetic impurities. These are needed to rotate the spins of the Ψ_0^t ($m_z = 0$) component such that it gathers non-zero m_z which are the "spin equal" components. An interface which exhibits inhomogeneous magnetism is called a spin active interface. Fig. 2.8 shows calculations on such spin active interface by Eschrig *et al.* [40]. The amplitudes of all generated components are depicted. In case of a weakly polarized ferromagnet (top curves), the spin-active interface does not generate a significant fraction of long-range triplet components. In case of a strongly polarized ferromagnet (bottom curves) the long-range triplet component which is aligned with the magnetization vector in the ferromagnet arises. The decay of this component in the ferromagnet is much slower than all other induced components in F. In the superconductor, all generated triplet components decay over a characteristic length ξ_S . The singlet component recovers over that distance, being at a lowest amplitude at the interface.

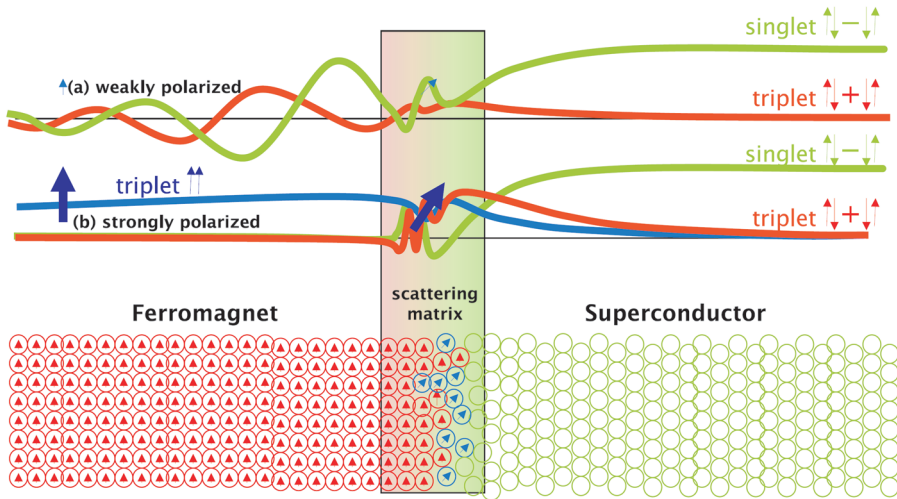


Figure 2.8: Calculation of the triplet components generated at a spin-active S/F interface, as taken from Eschrig *et al.* [40]. Top: weakly polarized ferromagnet, Bottom: strongly polarized ferromagnet

Chapter 3

Experimental details

3.1 Sample specifics

For this work the standard geometry of our devices are elongated S/F bi-layer and F/S/F tri-layer strips. The lateral dimension are either in the macroscopic regime, with a typical dimension of $100 \mu\text{m} \times 1000 \mu\text{m}$, or in the mesoscopic regime, with a typical dimension of $2 \mu\text{m} \times 40 \mu\text{m}$. These strips are contacted with non-magnetic, non-superconducting microscopic contacts which lead to large ($1 \text{ mm} \times 1 \text{ mm}$) contacting pads where connections to the measurement electronics can easily be made. The contact geometry to the strip is a 4-probe type with $10 \mu\text{m}$ respective 1 mm spacing between the voltage probes for the microscopic and macroscopic samples. For the superconductor we use Niobium (Nb), for the ferromagnets we use Copper-Nickel (CuNi) and the Nickel-Iron alloy Permalloy (Py = $\text{Ni}_{80}\text{Fe}_{20}$) to investigate respectively the weak and strong exchange limit. The contacting material is Gold (Au). The substrates used for our devices are all Silicon (Si) cut along the [100]-plane with a low p-type doping concentration of 10^{13-16} dopants per cm^3 . The devices are made in a three-step process: 1) depositing the layers for the strip, 2) defining and etching down the strip and 3) defining and growing the contacts. The details of these three steps are written down below.

In the first step, the metallic layers that comprise the strip are grown onto the Si(100) substrates by DC magnetron sputtering in a ultra high vacuum chamber with a background pressure of 10^{-9} mbar, using Argon (Ar) as plasma. Specific sputtering parameters for the different materials are as follows:

target	Ar pressure	sputtering rate
Nb	4.0 μbar	0.12 nm/sec
$\text{Cu}_{50}\text{Ni}_{50}$	4.0 μbar	0.04 nm/sec
$\text{Ni}_{80}\text{Fe}_{20}$	2.5 μbar	0.20 nm/sec

No additional cooling was used during sputtering, meaning the sputtering temperature starts at room temperature and slowly increases with some tens of degrees. For the sample with Py layers, a specially made magnetic sample holder was used to induce a homogeneous in-plane magnetic field. This sets the direction of the magnetic easy axis and also improves its switching properties. The orientation of the strip is defined parallel to this induced easy axis. Unless specifically mentioned, a thin Nb capping layer (about 2 nm thick) is added on top of the layer package to prevent oxidation of the top ferromagnetic layer. The purity of the Nb target is 99.95 % which yields a T_c of 9.1-9.2 K. The ratio Cu/Ni in the target is 50/50 (atomic percentage), which results in an approximate 43/57 ratio at the sample. The Curie temperature of the

$\text{Cu}_{43}\text{Ni}_{57}$ is around 150 K and it has a degree of polarization close to zero. The (corresponding) exchange energy is some tens of meV ($\ll E_F$) making it a model weak ferromagnet. For the Py the Curie temperature is much higher, around 950-1000 K, and it has a degree of polarization of about 45 %. The (corresponding) exchange energy is some hundreds of meV, which is a sizable fraction of the Fermi energy, making it a strong ferromagnet.

In the second step the strips are defined by standard lithographic techniques and afterwards etched down. First, a MaN 2405 (a negative-tone resist) is spin coated at 6000 RPM (during 60 seconds) on top of the layer package. Afterwards it is baked for 10 minutes at 90 °C. Standard electron beam lithography, using a JEOL JSM 820 Scanning Microscope, was used to pattern the strips and several alignment markers. The beam current was 30 pA and the dose 45 $\mu\text{C}/\text{cm}^2$. As developer, the MaD 332 was used to dissolve the non-exposed areas (in about 30-35 seconds). The thus obtained

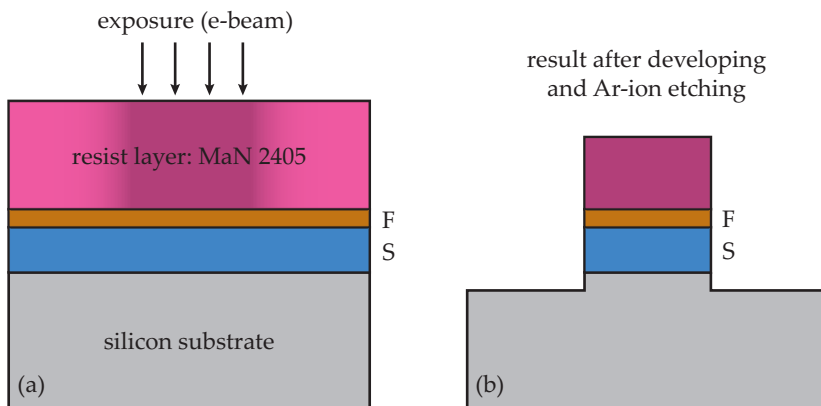


Figure 3.1: Sketch of the side-view of the substrate after (a) spin coating the MaN 2405 resist, and (b) etching down the strip. In (a), the darker-colored resist areas will be sufficiently exposed by the electron beam, and after developing that is what remains.

resist pattern serves as a protective mask for the following Ar ion-etching (see Fig. 3.1) which is performed at 2.5 μbar Ar pressure in a background pressure of 10^{-6} mbar. Etch times were ranging from 5 to 15 minutes depending on the specific layer thicknesses and to prevent burning and hardening of the resist, the sample was continuously cooled with Nitrogen gas (N_2). Additionally, the sample normal makes a small angle with the incoming ions and the sample is rotating in plane at a speed of order 10 Hz. In this way, the unwanted re-

deposition (of the sputtered material) at the sides of the strip is continuously etched away. Finally, the remaining part of the resist mask was cleaned-off using boiling acetone (at 70-75 °C).

In the last step, the contacts are lithographically defined using a lift-off geometry after which the contacting material is sputtered. The used lift-off geometry consist of a double positive-tone resist layer, where the in-plane development of the bottom resist expands further then the top layer. A PMGI/PMMA double resists layer is spin coated. First the PMGI at 4000 RMP (during 60 seconds) followed by a post-bake of 90 minutes at 200 °C, next the PMMA at 4000 RMP (during 60 seconds) followed by a post-bake of 30 minutes at 160 °C. Contacting pads and leads towards the strips were pat-

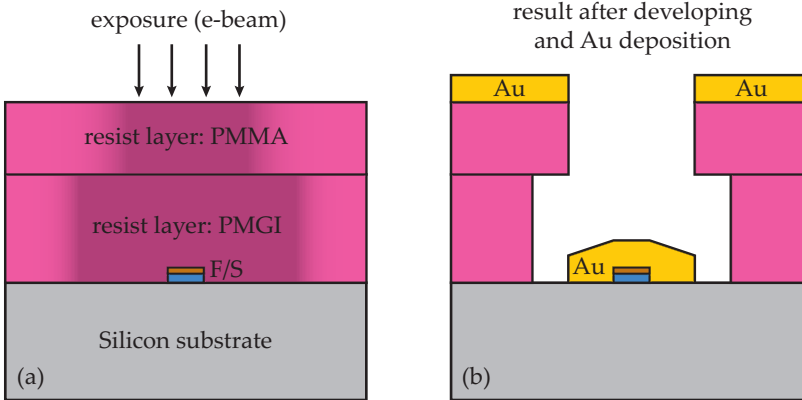


Figure 3.2: Sketch of the side-view of the substrate after (a) spin coating the PMGI/PMMA double resist layer, and (b) sputtering the contact material. In (a), the darker-colored resist areas will be sufficiently exposed by the electron beam, and after developing that is what dissolves. In (b), all the remaining resist (with Au on top) is dissolved using developer, completing the lift-off technique.

terned using the JEOL Microscope, where the alignment markers are used to align this new pattern with the strip. The used beam current was 10 nA and the dose 200 $\mu\text{C}/\text{cm}^2$. The development is now a two-step process. First the top PMMA layer is developed in diluted acetone for 35 seconds (diluted with demi-water, roughly at a 50/50 volume ratio). Second is the development of the PMGI layer in MF 322 for 5 minutes, where the last 2-3 minutes are used to create an undercut. A short cleaning in an Oxygen plasma is performed to remove some resist residues from the contacting areas on the strips (to lower

the interface resistance). Finally the Au contacts are sputtered (see Fig. 3.2) in a ultra high vacuum chamber with a background pressure of 10^{-7} mbar using an Ar plasma. Additionally, an initial few monolayers of Titanium (Ti) are sputtered *in situ* as adhesion layer for the Au. The Au contacts are aimed at a thickness of 100 nm and sputtered at an approximate rate of 0.17 nm/sec with an Ar pressure of 4 μ bar. After sputtering the sample is immersed in NMP (N-methyl-2-pyrrolidone) to complete the lift-off by dissolving all resist.

3.2 Measurement setup specifics

The three main types of transport measurements on our samples are field dependent resistance measurements $R(H)$ at low temperatures, temperature dependent resistance measurements $R(T)$ and field dependent critical current measurements $I_c(H)$ (I_c is determined from measuring the current-voltage characteristics). These measurements are all performed using the same setup, which consist of a standard ^4He cryostat with a home-built insert which is connected to the measurement electronics (see Fig. 3.3). The cryostat is equipped with magnetic shielding to provide a low-noise environment and a superconducting coil (NbTi wire) to provide the magnetic field (up to 1 T). The cryostat insert is a closed type, where the sample chamber is shielded from the Helium bath inside the cryostat. The inner sample space is continuously pumped during measurements and reaches a pressure around 0.1 mbar. An Agilent DC power supply was used for the coil magnet. It provided a smallest current step of 1 mA, which corresponds to an induced field of about 0.1 mT. A heater (Cu wire) is used to increase the sample temperature which, for the given pressure, can go up to at least 10 K. The temperature itself is measured using a carbon glass resistor which has a low temperature sensitivity of about 200 Ω/mK . The desired (low) temperature is PID-regulated by an isolated GPIB circuit to increase its response time, resulting in a good temperature stability with fluctuations of 0.1-0.3 mK at the sample, in the range 4.2 K to 10 K. A Keithley K2400 was used for the heater current source. To measure the resistance of the thermometer a Keithley K220 current source and a Keithley K181 nanovoltmeter were used. By pumping the Helium bath directly the temperature can be lowered down to 1.7-1.8 K, which is necessary for the $I_c(H)$ measurements. All the $R(H)$ and $R(T)$ measurements are performed in the range 5-10 K, as the superconducting transition temperature for our samples is between 5 K and 7 K.

All measurements are current biased and for the $R(H)$ and $R(T)$ measurements we perform bipolar measurements (measuring the voltage difference

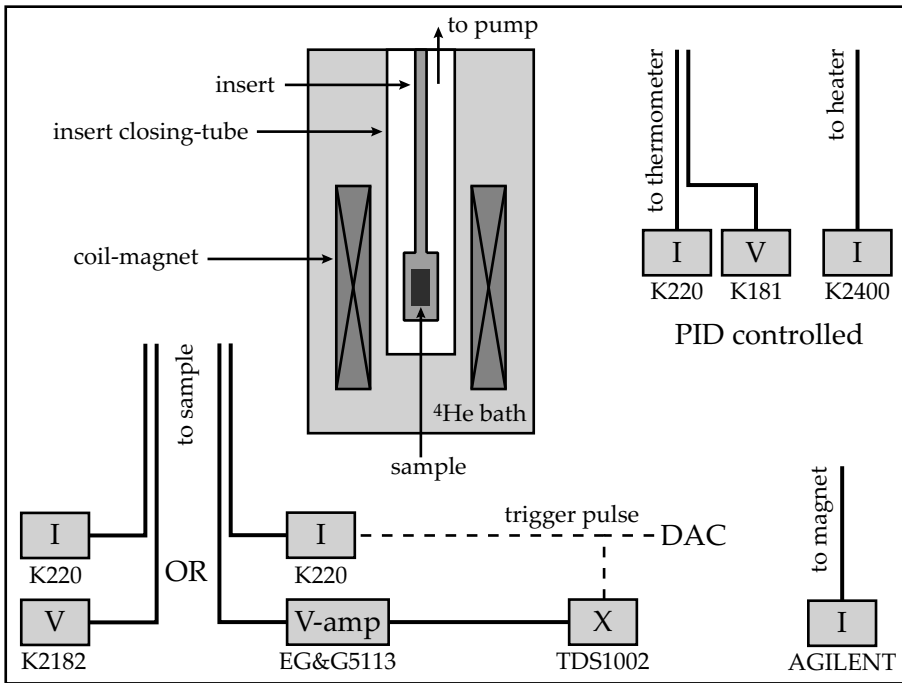


Figure 3.3: Schematic of the measurement setup.

for both positive and negative current and taking the average), with a current density of the order $2.5 \times 10^8 \text{ A/m}^2$. The sample is measured using a Keithley K2182 nanovolt meter and Keithley K224 programmable current source. For the critical current measurements we make use of a pulsed current technique. By applying short current pulses, Joule heating of the sample is minimized and the critical current can be determined much more accurately. We used 3 ms current pulses, with an interval of several seconds between the pulses and an increasing amplitude until the critical current is reached and the superconductor is driven into the normal state. The samples are initially cooled down in zero field condition and the first measurement at a fixed temperature always starts in zero applied field. The current pulse generates a voltage pulse across the voltage probes of the sample, which is amplified and measured with an oscilloscope. An external trigger pulse is used to synchronize the current pulse with the measurement time-window of the oscilloscope to catch the voltage pulse. The voltage amplifier is an EG&G 5113 differential amplifier with incorporated band filters and the oscilloscope is a digital Tektronix TDS1002. The external trigger is generated by a standard DAC-interface and all equipment is GPIB controlled.

Chapter 4

Superconducting spin-valve: weak ferromagnetic case

4.1 Introduction

A superconductor (S) and a ferromagnet (F) both show a mean-field order for the electron spin. In the ferromagnet the ordering is in real-space and the exchange field (H_{ex}) (or exchange energy E_{ex}) favors one spin direction, while in the superconductor the ordering is in k-space and the order parameter (Δ) is built up from Cooper pairs consisting of electrons with opposite spins. Bringing these antagonistic types of order into close proximity leads to a complex interplay with new possible ground states, and possible consequences for the superconductivity as well as for the magnetism [41, 42, 31]. The foremost characteristics of the S/F proximity effect in the case of homogeneous H_{ex} are the oscillatory decay of the induced order parameter in the F metal and the emergence of spin triplet correlations. In special cases this could enable the formation of the spin equal (long range) components of the triplet, in particular for inhomogeneous exchange fields [39] or halfmetallic ferromagnets [43]. The oscillatory order parameter brings about an oscillation of the superconducting transition temperature T_c as function of the F layer thickness, which has been observed in various experiments [44, 45]. This phenomenon is reasonably well understood and described by theoretical models. As for the existence of long range triplet components, two experiments has been reported thus far [29, 30], but their existence is not yet fully accepted.

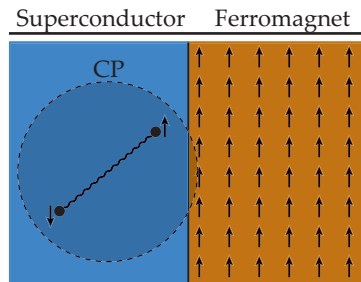


Figure 4.1: Spin ordering of the two electrons of a Cooper pair (CP) in the superconductor, and of the lattice points in the ferromagnet.

Two main consequences of the interplay between magnetism and superconductivity are the S/F/S π -junction, and the F/S/F superconducting spin-valve. In the π -junction the order parameter oscillation in the F metal yields a phase change of π between the superconducting banks, which was demonstrated to exist both by transport experiments [46] and in measurements of the density of states on the F-side of and S/F sandwich [47]. The spin-valve exhibits (in theory) re-entrant superconductivity by switching the magnetization of the F banks from parallel (P) to anti-parallel (AP), which would lead to a controllable supercurrent through a small field manipulation [9, 10]. Theory describing both phenomena is well developed for the case of weak ferromagnetism with homogeneous exchange fields, as then the quasiclassical

Green functions adequately describe the transport probability of electrons and Cooper pairs. However, inhomogeneities in H_{ex} , in particular from domains or domain walls, still pose difficulties for both experiment and theory. Moreover, for ferromagnets with strong exchange fields, where E_{ex} is no longer much smaller than the Fermi energy E_F , or with non-zero polarization of the electronic spin bands, the current framework is not suitable as it does not incorporate these effects. For the case of the spin-valve effect, which is strongest close to T_c where superconductivity is still weakly developed, magnetic domains could also have a significant effect on the superconducting gap and thus on the working of the superconducting spin-valve. This is the issue we address in this and the following chapter, where here we deal with weak ferromagnetism and in the next chapter with strong ferromagnetism.

4.2 The superconducting spin-valve

The conventional superconducting spin-valve structure is a system where two ferromagnetic layers are separated by a superconducting spacer. It was first proposed by Tagirov [9] (and similarly by Buzdin and co-workers [10]) who calculated, using linearized Usadel equations, the superconducting transition temperature of the S-layer as function of F-layer thickness, for both the parallel (P) and antiparallel (AP) direction of exchange fields. It was shown that for weak ferromagnets, T_c for the anti-parallel configuration is always higher than for the parallel case, where a weak ferromagnet really means a ferromagnet with $E_{\text{ex}} \ll E_F$ and a polarization close to zero. This change in T_c becomes more interesting when the thickness of the F layers becomes of the order of the coherence length in F, since there exist a (small) thickness range of the F layers where it should be possible to fully suppress superconductivity in the parallel configuration, while having a finite T_c in the anti-parallel configuration. It should thus be possible to switch between the normal and superconducting state, and hence "valving" a supercurrent, if the direction of the exchange fields can be controlled. The spin-valve can only work if there is a coupling between the two F layers which additionally couples to the order parameter, since it is the order parameter which should differentiate between a parallel or anti-parallel alignment. This coupling is provided by Cooper pairs and therefore the thickness of the S layer should be limited to several times the superconducting coherence length. When this condition is met, Cooper pairs in the superconductor can touch both the F layers (i.e. one of the electrons is "close" to one of the F layers, and the other electron is "close" to the other F layer). Due to the non-local nature of the Cooper pairs (and the Andreev reflection process), the Cooper pair can leave the superconductor such that

the two electrons enter a different F layer. In the anti-parallel alignment of the direction of exchange fields, the two electrons enter identical spin bands. However, this is not true for the parallel alignment. In that case, there is a potential difference between the electrons which is balanced by a difference in kinetic energy (just as for the standard S/F proximity). This kinetic momentum difference leads to additional dephasing of the induced "pair", which in turn results into a lowering of the Cooper pair density. The final result is thus an additional lowering of T_c in case of parallel alignment. This mechanism of the (weak-limit) spin-valve is illustrated in Fig. 4.2. Dipolar fields were not taken into account in theoretical model, and thus an argument of the kind "In an anti-parallel alignment the dipolar fields create a more natural environment compared to the parallel alignment" to explain the T_c difference is, although correct, not what the weak-limit models are about. When the thickness of

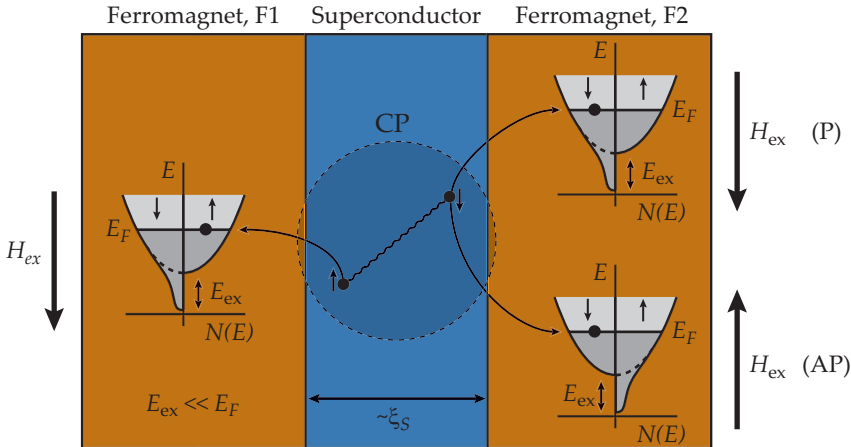


Figure 4.2: Comparing the parallel (P) and anti-parallel (AP) configuration of the ferromagnetic exchange fields H_{ex} in a superconducting spin-valve. Here, a Cooper pair (CP) couples the two ferromagnetic layers F1 and F2, with ξ_S the superconducting coherence length. In F1 the orientation of H_{ex} is "down" while in F2 the orientation is either "up" (AP configuration) or "down" (P configuration). The presented electron band structures are impressions of how a weak ferromagnet is treated in the theoretical framework: as a normal metal with identical spin bands near the Fermi energy E_F (and thus no spin polarization) and a weak exchange field $E_{\text{ex}} \ll E_F$, making the distortion to the spin bands very small

the F layer becomes of the order of the coherence length in the ferromagnet (ξ_F), the induced oscillating order parameter in F reaches its outer boundary. This results in a back-reflection of the oscillation and causes self-interference. This is the origin of the minimum in Fig. 1.4, and thus of the re-entrance effect.

By now, various spin-valve systems has been measured. A number of them have Nb as superconductor in combination with weakly magnetic CuNi [48, 49] or stronger magnets such as Ni [50], Ni₈₀Fe₂₀ (Permalloy, Py) [51, 52, 53], Co and Fe combined [54] or Co [55]. Moreover, the systems do not only differ in type of magnet, also the method to obtain switching is different. Some use a spin-valve stack with antiferromagnetic Fe₅₀Mn₅₀ adjacent to one of the F layers in order to pin its magnetization, while the magnetization of the other layer can rotate freely. This is the case in the reports on Nb/CuNi [48, 49], Nb/Ni [50], Nb/Py [52]. The other experiments rely on the difference in thickness of the F layers in order to obtain different coercive fields, as in the reports on Nb/Py [51, 53], Nb/(Co,Fe) [54] and Nb/Co [55]. The experiments using a pinning layer confirm the general prediction for the superconducting spin-valve: in the P alignment of the two F layers, the transition temperature T_c^P is slightly lower than T_c^{AP} in the AP alignment. The experiments without pinning layer report the reverse behavior, with strong indications that now stray fields and magnetic coupling of the F layers play a role. Taken together, the literature data seem to suggest that the presence of the pinning layer makes a distinction in the outcome of the experiments by suppressing secondary stray field effects originating from local inhomogeneities (like domain walls). We are not aware that this observation has been made before, but it makes it possible to understand all the different reports in a unified way. There is, however, another issue which has not been fully resolved: the size of the apparent spin-valve effects are small compared to theoretical predictions. Changes in T_c are mostly less than 10 mK, and in bilayer experiments involving Py it was demonstrated that the relative enhancement of superconductivity over domains walls resulted in a similar-sized increase in T_c [56]. For the weak ferromagnets such as Cu_{1-x}Ni_x (with x in the range 0.5 - 0.6), which played such an important role both in demonstrating π -junctions and (apparent) spin switching, it was not yet investigated whether domains in the F layer can enhance superconductivity in a similar way. In this chapter, we report on a study of Nb/Cu₄₃Ni₅₇ bilayers and trilayers where we compare anisotropic magnetoresistance (AMR) effects in the normal state with the magnetoresistance in the superconducting transition and measurements of the depairing (critical) current I_{dp} below T_c , both for microstructured and large-scale samples. We show that in bilayers enhanced superconductivity is indeed found when the F-layer is in a domain state. In the transition this is seen as a decrease in resistance in the field range where domains occur according to AMR. Below the transition it is seen as a maximum in I_{dp} as function of the in-plane magnetic field. Interestingly, the maximum occurs at significantly higher field values than where the domain

state occurs above or in the transition, suggesting that the well-developed superconductivity now influences the mechanism of magnetization rotation in the F layer. Finally, in trilayers we basically make the same observations. A domain-state dominated mechanism for spin-valve effects therefore cannot be ruled out.

4.3 Sample details

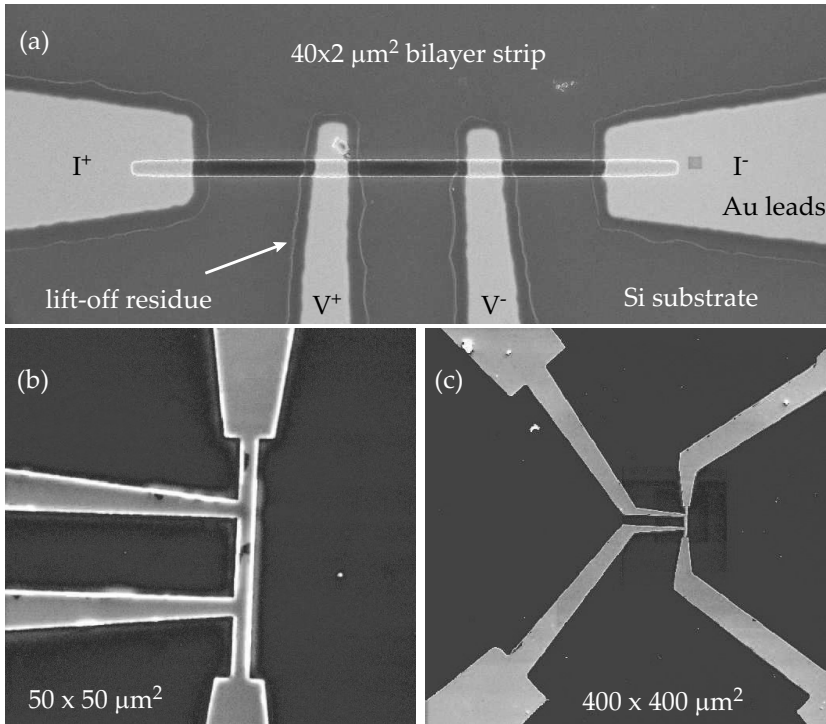


Figure 4.3: SEM images of $40 \times 2 \mu\text{m}^2$ bilayer devices (a) standard 4-probe device, (b) contact included device and (c) bonding pads and leads. In (a), the bright colored Au leads were deposited using a lift-off mask technique, leaving typical Au residues. The geometry of (c) is used for all devices.

Nb/Cu₄₃Ni₅₇ layers were grown onto Si(100) substrates by DC magnetron sputtering in a ultra high vacuum chamber with a background pressure of 10^{-9} mbar and an Ar pressure of $4 \mu\text{bar}$ with Nb as bottom layer (see Ch. 3.1 for additional details). The Cu₄₃Ni₅₇ thickness was kept at 10 nm for all samples, while the Nb layers are 20 nm for the bilayers, and 25 nm for the trilayers.

Also all devices have an additional Nb capping layer (of 1-2 nm thick) on top of the $\text{Cu}_{43}\text{Ni}_{57}$ top layer. The ratio Cu/Ni in the target is 50/50 (atomic percentage), which results in an approximate 43/57 ratio at the sample. The Curie temperature of the $\text{Cu}_{43}\text{Ni}_{57}$ is around 150 K, and it has a degree of polarization close to zero (making it a model weak ferromagnet). The purity of the Nb target is 99.95% which yields a T_c of 9.1-9.2 K. Different samples were used for different bridge widths, although sometimes two bridges were patterned and measured on the same sample. Standard electron beam lithography was used to pattern micro-sized strips with a length of 40 μm and a width ranging from 1 to 4 μm . These strips were etched with Ar ion-etching (at 2.5 μbar Ar pressure) in a background pressure of 10^{-6} mbar. Au contacts were sputtered in a second deposition step using a lift-off resist-mask technique, with a few monolayers of Ti used as an adhesion layer for the Au. The contact geometry is 4-probe with 10 μm spacing between the voltage probes. Fig. 4.3a shows SEM (scanning electron microscope) images of $40 \times 2 \mu\text{m}^2$ bilayer strips. The contour lines surrounding the high contrast Au leads are Au lift-off residues. Trilayers and macroscopic sized samples were made using the same recipe, where for the latter the strip dimensions are $2000 \times 200 \mu\text{m}^2$ with 1000 μm spacing between the voltage probes. The superconducting transition temperature for the bilayer samples, measured after structuring was 6.5 K, except for the 40×1 sample where it was 7.5 K, probably due to a slightly thicker Nb layer. For the trilayers it was 5.9 K. The thickness dependence of T_c for plain Nb films and for Nb/F and F/Nb/F are presented in earlier works [57, 58]. The two-step process in order to make separate electrical Au contacts to the strips, rather than etch out a full geometry including contacts, is crucial for the experiments, since otherwise the influence of the (magnetic) contact areas can be significant as we show in Ch. 4.5. For those devices with 'contacts included', strips including leads to the bonding pads are all etched down during one step of Ar ion-etching.

The micron sized lateral dimensions bring along two main advantages: it promotes probing states with only few domains, avoiding a large spaghetti of domain states, and the resistance c.q. the cross-section is sufficiently high for anisotropic magnetoresistance (AMR) measurements and critical current (I_c) measurements. The AMR measurements play a key role in our experiments since they allow to determine if and when domains appear in the ferromagnet just above T_c . This can then be compared to the response of the superconductor to an applied field in and below the transition. Resistance measurements were done in a standard ^4He cryostat with magnetic shielding to provide a low-noise environment, and a superconducting coil to provide the magnetic field

(ranging up to 1 T). All field measurements are performed with the externally applied field directed along the strips, which implies the current is parallel to field. For CuNi this should result in a resistance *decrease* when domains are being formed in a initially homogeneous state, similar to the behavior of the elemental transition metals Fe, Co and Ni. At temperatures well below T_c we performed I_c measurements, which probe the gap amplitude in the superconductor. The method for such measurements makes use of pulsed currents, and was described in Ref. [59].

4.4 Results

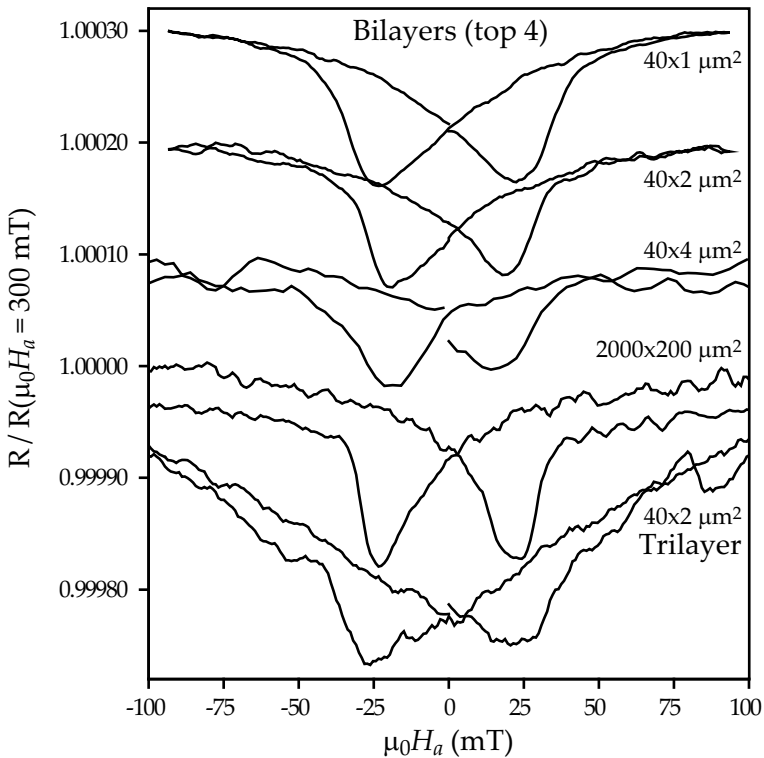


Figure 4.4: Resistance normalized to the value at 300 mT as function of an in-plane applied field H_a on Nb/Cu₄₃Ni₅₇ bilayer strips of 40×1 , 40×2 , 40×4 and $2000 \times 200 \mu\text{m}^2$. Temperatures were in a range between 7.5 K and 9 K for the different datasets. The curves are shifted for clarity, each with a value of 1×10^{-4} with respect to the one below. Also shown are data on a $40 \times 2 \mu\text{m}^2$ Cu₄₃Ni₅₇/Nb/Cu₄₃Ni₅₇ trilayer strip (all with Nb in normal state); these data are not shifted.

Data were obtained for samples with different bridge widths, as well for temperatures above and below T_c , and we present them in the following way. We first give a brief overview of the behavior of the different samples. We then concentrate on the $40 \times 2 \mu\text{m}^2$ bilayer strip, which best illustrates most of the physics, before coming back to the samples with different bridge widths. The results of the field-dependent resistance measurements $R(H)$ at a temperature just above T_c are presented in Fig. 4.4 for bilayer strips with a width of $1 \mu\text{m}$, $2 \mu\text{m}$ and $4 \mu\text{m}$, as well as for the large bilayer structure ($2000 \times 200 \mu\text{m}^2$), and for a $40 \times 2 \mu\text{m}^2$ trilayer strip. The resistance values are normalized to the value measured at 300 mT. The data clearly show hysteresis and resistance dips. The relative resistance change is of order 10^{-4} and the minimum of the dips is close to a field of ± 22 mT. This field we call the dip-field $H_{\text{dip},n}$ (n meaning the normal state) and is generally taken as the coercive field of the ferromagnetic layers. The width of the hysteretic parts is about 50 mT. All bridges show similar values for $H_{\text{dip},n}$ and the hysteretic width, and they lead to the conclusion that domains are forming in all our ferromagnetic layers, despite the parallel field alignment and narrow strips with high aspect ratio.

4.4.1 Results on the $2 \mu\text{m}$ bridge

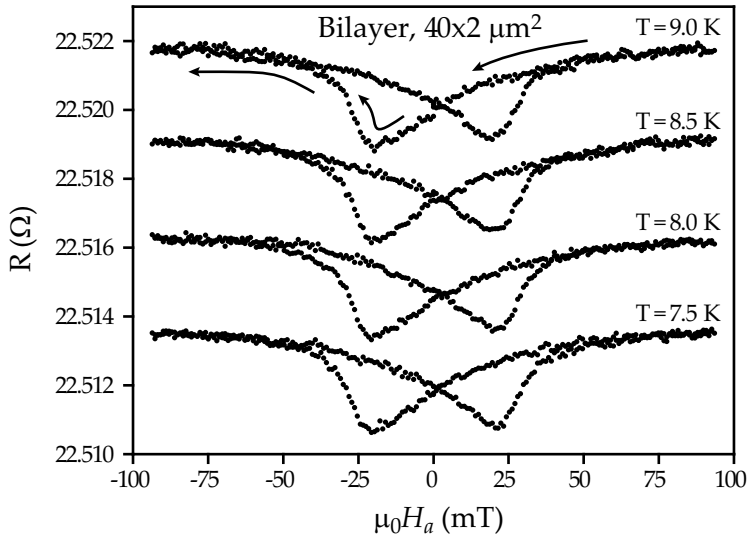


Figure 4.5: Resistance R versus in-plane applied field H_a on a $40 \times 2 \mu\text{m}^2$ Nb/Cu₄₃Ni₅₇ bilayer strip at several temperatures above the superconducting transition. Arrows in the top curve show the direction of the field sweep starting from high fields.

Results of $R(H)$ on a $40 \times 2 \mu\text{m}^2$ bilayer strip for several temperatures $T > T_c$ are presented in Fig. 4.5 and illustrate that the values $H_{\text{dip},n}$ are independent of temperature in the range of a few Kelvin above T_c . The same measurements are repeated for $T < T_c$ and shown in Fig. 4.6, where the resistance is normalized to the value at zero field. The measured signal now comes predominantly from the superconducting layer, which is shorting the ferromagnetic layer by percolation paths. The $R(H)$ are measured at var-

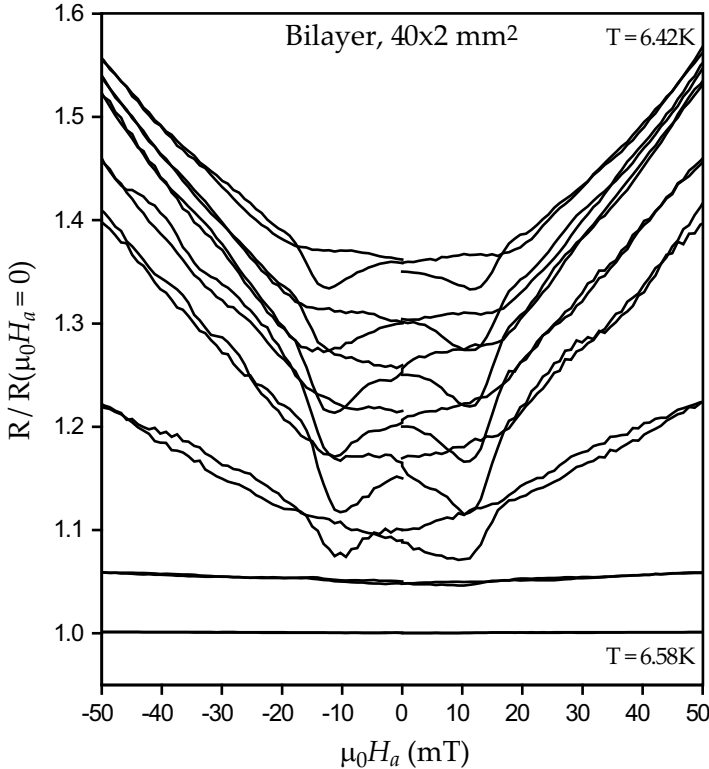


Figure 4.6: Resistance normalized to the value at zero field on a $40 \times 2 \mu\text{m}^2$ Nb/Cu₄₃Ni₅₇ bilayer strip at several temperatures in the transition curve (Nb in superconducting state). The bottom curve is for $T = 6.58$ K. Each subsequent curve is shifted by $+0.05$ with respect to the previous one, with corresponding temperatures 6.55, 6.52, 6.50, 6.48, 6.46, 6.44 and 6.42 K (top curve).

ious temperatures along the transition curve shown in Fig. 4.7, which has an approximate width of 100 mK. The 100 mK width makes that a relative resistance change of 10^{-4} (our typical result in the AMR measurements) corresponds to a temperature change of 0.01 mK. This is below our measurement

accuracy, so we loose track of any AMR features while in the transition area. Again there are two clear dips visible as well as a parabolic shaped response at higher fields, for all measurement except for the one very near the top of the transition curve at 6.58 K. That one gives a straight line; apparently the superconductor is driven into the normal state by the measurement current which in all measurements was of the order 2.5×10^8 A/m². The relative resistance change $(\delta R)/R$ in the dips is now of order of percents, much larger than the observed AMR effect. Moreover, the size of the dip, meaning the maximum value of the resistance difference δR between forward and backward sweeps, goes through a maximum. Fig. 4.7 shows δR taken from the unnormalized data as function of temperature. It peaks at 6.52 K, which is about halfway in the transition in the steepest part. We can related this to a shift in T_c according to $\delta R = \delta T_c(\partial R/\partial T)$ which comes to a few mK. Looking more carefully

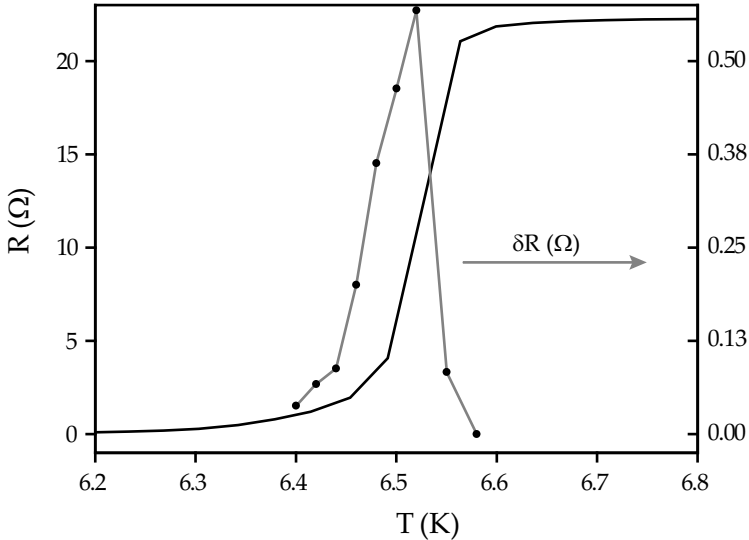


Figure 4.7: Temperature variation of the resistance of the device from Fig. 4.6 in the transition (left-hand scale), which is a typical result for all our devices. It also shows the temperature variation of the magnitude of the resistance dip δR (right-hand scale).

at the $R(H)$ curve we notice that (coming from positive fields) the parabolic shaped curve, which reflects the standard response of the superconductor on a magnetic field, first makes an upward oriented kink around $H = 18$ mT before it arrives at the dip, with $H_{\text{dip,s}} = -12$ mT (s denoting the superconducting state). The location of the dips and their normalized sizes do not show a

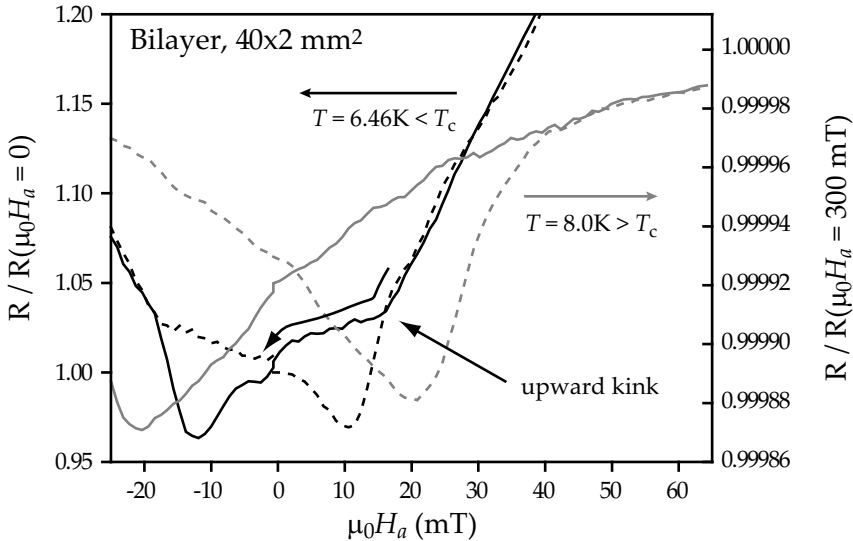


Figure 4.8: Comparison of the field dependence of the resistance R for a $40 \times 2 \mu\text{m}^2$ Nb/Cu₄₃Ni₅₇ bilayer strip, with T above T_c (right-hand scale) and below T_c (left hand scale). The solid lines are data taken with *decreasing* field starting from +300 mT, as shown by the arrows; The dashed lines are data taken with *increasing* field starting from -300 mT. The upward kink in the decreasing-field data below T_c is also indicated.

strong temperature effect, which is a clear sign that the development of the superconducting gap is not significantly changing the ferromagnetic domain structure. Important to remark, however, is that the dip fields $H_{\text{dip},s}$ are almost a factor two smaller than the dip fields $H_{\text{dip},n}$. We come back to this below, but for the moment we assume that they are still due to the domain state occurring in the Cu₄₃Ni₅₇ layer. The dips reflect an enhancement of the (emerging) superconducting state, and therefore indicate that T_c is shifting towards higher values in the domain state, just as seen in previous work on Nb/Py bilayers. In Fig. 4.8 we show a comparison of the $R(H)$ measurements (on our $40 \times 2 \mu\text{m}^2$ bilayer) above and below T_c . It illustrates the difference in dip fields, but more important is to establish that the upward kink seen below T_c in the decreasing field data is still at positive fields in a regime, according to the AMR data, where domains are growing. On the other hand, no similar feature is detected in the AMR data.

We now want to discuss the observations with respect to the dip fields and the upward kink. Firstly, it is important to realize that the resistance dip occurring in the AMR effect is due to the fact that the resistance in the

ferromagnet depends on the angle between the local magnetization M and the current I with, for the case of CuNi, the lowest resistance when $M \perp I$ [34]. The resistance minimum found when changing the direction of the magnetization then signifies the maximum amount of domains with a direction perpendicular to the current and the bridge. In the superconducting state, however, the resistance minimum comes about by a different mechanism, since it is determined by the average exchange field sampled by a Cooper pair of characteristic length ξ_S , which can be quite large close to T_c . There is no reason why the two types of averaging over a domain configuration would yield the same resistance minimum; for instance, a configuration where all of the magnetization is perpendicular to the current would give a strong minimum in AMR, but no resistance lowering in the superconducting state, since the exchange field in that case is homogeneous. It is interesting to remark that this difference would not be observable in Nb/Py, since in that case the switching was in such a small field range (order 10^{-4} T) that a possible averaging difference would go unnoticed [56].

That leaves an explanation for the kink feature in $R_s(H)$. Looking again at Fig. 4.8, it does not seem a coincidence that the kink in the decreasing field data occurs around the coercive field in the increasing field part of the loop. In very similar measurements ($R(H)$ in the resistive transition) on Nb/Py [56] a small increase in R was found at this field point in the hysteresis loop, although it was not visible in the magnetization that domains started to form. Apparently, domain formation starts when the field value comes inside the hysteresis loop even for quite square loops. Here we believe that the domain formation accelerates and starts to produce stray fields (either perpendicular, or in-plane), resulting in the kink because they act as Cooper pair breakers.

4.4.2 Other bilayers and trilayers

The 2 μm wide bilayer strips clearly show a decrease in resistance of the superconductor in the domain area of the ferromagnet. The results for other strip widths, specifically for 1 μm and 'large' (200 μm wide, 2 mm long) are given in Fig. 4.9, together with the result on a $40 \times 2 \mu\text{m}^2$ trilayer. These presented curves are all below the steep part of the transition curve. They basically confirm the 2 μm data, but there are some differences. First of all, in the narrower 1 μm strip the resistance dips have completely disappeared, while the AMR data of Fig. 4.4 definitely indicate the presence of domains. Instead, only the parabolic feature remains here. On the other hand, for the larger widths the resistance dips are present at the same field value or a bit lower but now a new sharp dip appears, precisely coincident with the upward

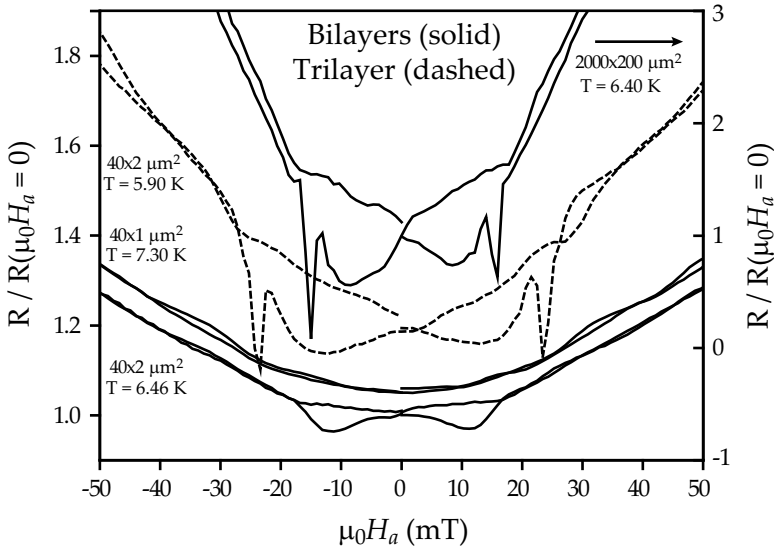


Figure 4.9: Normalized resistance measurements on a 40×1 , 40×2 and $2000 \times 200 \mu\text{m}^2$ Nb/Cu₄₃Ni₅₇ bilayer (first one shifted by +0.05) and a $40 \times 2 \mu\text{m}^2$ Cu₄₃Ni₅₇/Nb/Cu₄₃Ni₅₇ trilayer strip (shifted by +0.2). Temperatures are all below the steep part of the corresponding transition curves.

kink discussed in the previous paragraph. Important of course is that also the new dip signifies lowering of resistance and is therefore not due to stray field enhancement. Without more precise knowledge of the size and shape of the domains and their evolution, it is difficult to give a solid explanation for these observations. What is known from decoration experiments with magnetic particles is that the typical domain size on large samples is of the order of $0.5 \mu\text{m}$ [60]. Still, we perceive a hierarchy of events. For the smallest strip AMR detects the occurrence of domains with a component of their magnetization perpendicular to the current, but with a magnetization spread that is not large enough to significantly change the average field that Cooper pairs experience. For the $2 \mu\text{m}$ strip the domain configuration in the switching is apparently different, and leads to a smaller averaged exchange field. For wider strips the domain state passes through even more configurations. In particular around the coercive field there probably is a large number of small domains, which leads to a sharp resistance dip.

Fig. 4.9 also shows a measurement on the trilayer structured as a $40 \times 2 \mu\text{m}^2$ strip. The data show both the shallow dips and the sharp dips, similar to the

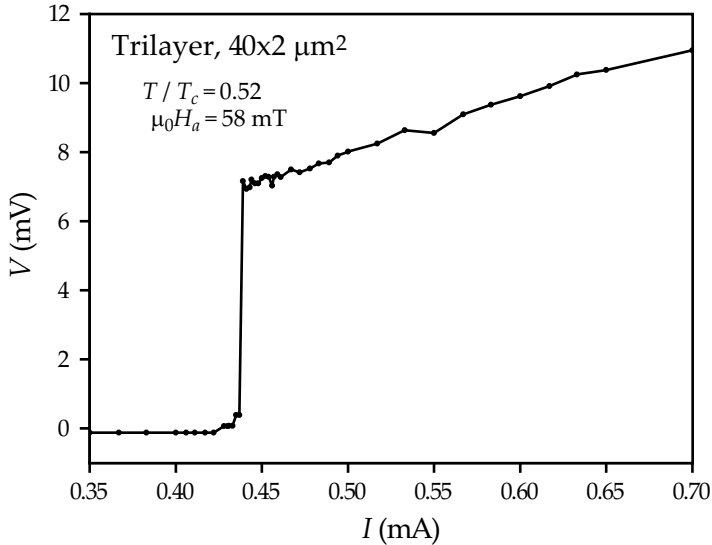


Figure 4.10: Voltage V versus current I measured on a $40 \times 2 \mu\text{m}^2$ $\text{Cu}_{43}\text{Ni}_{57}/\text{Nb}/\text{Cu}_{43}\text{Ni}_{57}$ trilayer strip at 4.3 K and 58 mT. The sharp jump at 0.44 mA is taken as a measure for the critical (depairing) current.

bilayers with wider bridge widths. The bilayer results exclude that the two dips are due to different switching fields for the two layers, but in the spirit of the hierarchy sketched above, the domain state in the trilayer seems to resemble those of wider bilayers, which suggest a form of coupling between the two layers. From the size of the dip in $R_s(H)$, and the steepness of the transition curves at that temperature, we can estimate the corresponding T_c shift. For all our devices this results in an approximate shift of few mK. We also measured the transition curve at H_{dip} for the cases that the field was set from high positive fields (corresponds to the parabola) and from high negative fields (corresponds to the dip). In this way we found a shift in T_c of about 1.5 mK, which is hardly different from the values reported for the CuNi-based spin-valve in Ref. [49].

4.4.3 $I_c(H)$ well below T_c

So far we focussed on transport measurements around the transition, which consistently show an enhancement of T_c in the domain state of the F layers. To see what happens below T_c we conducted a series of critical current measurements as function of applied field, $I_c(H_a)$ by measuring the current I -

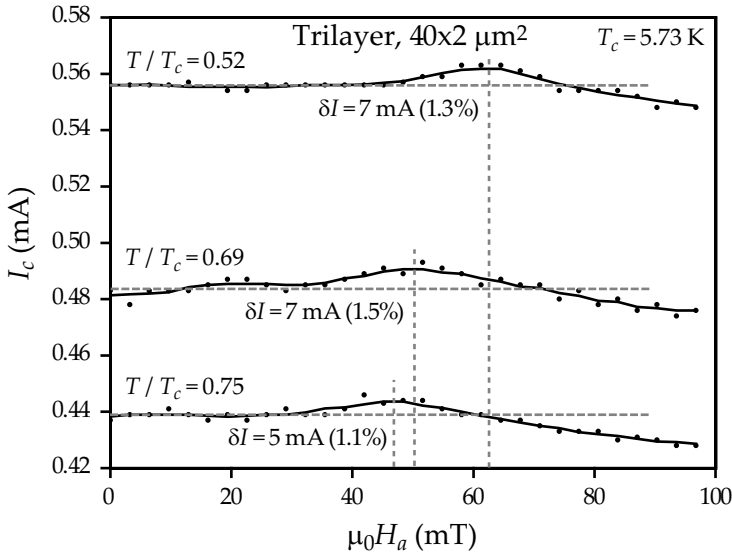


Figure 4.11: Critical current measurements I_c as function of applied magnetic field H_a on a $40 \times 2 \mu\text{m}^2$ $\text{Cu}_{43}\text{Ni}_{57}/\text{Nb}/\text{Cu}_{43}\text{Ni}_{57}$ trilayer strip for different reduced temperature T/T_c as indicated. The value of T_c is 5.73 K. Dotted vertical lines indicated the positions of the maxima in I_c ; dotted horizontal lines show the average value of I_c around zero field as reference for the indicated values of increase in I_c at the maximum.

voltage V characteristic. We used 3 ms current pulses, with an interval of several seconds and increasing in amplitude until the critical current is reached and the superconductor is driven in the normal state. The sample is initially cooled down in zero field condition and the first measurement at a fixed temperature always starts in zero applied field. The I - V curves all showed a sharp jump from almost zero voltage to the normal state, as we found before on S-films and S/F bilayers [59, 57]. An example is given in Fig. 4.10. The jump indicates that we are measuring a depairing current rather than the onset to vortex flow, which means that the measurement is directly sensitive to the superconducting gap. Also, the value of I_c is well defined due to the sharp transition. The results for the $40 \times 2 \mu\text{m}^2$ $\text{Cu}_{43}\text{Ni}_{57}/\text{Nb}/\text{Cu}_{43}\text{Ni}_{57}$ trilayer are shown in Fig. 4.11, for three temperatures well below T_c , in terms of the reduced temperature $t = T/T_c$ down to $t = 0.5$. All data show the same behavior, with initial constant I_c for increasing H_a , followed by a small maximum of the order of 1 %, before a decrease sets in. The field values where the maximum occurs, H_{max} , are in the range 50 mT - 60 mT and increase with decreasing temperature. The uncertainty in the determination of

I_c is basically the step size for the increase in current ($1.8 \mu\text{A}$) and therefore significantly below the enhancement of I_c we find around H_{max} . We interpret the enhanced I_c as an enhancement of the superconducting gap, and note that the percentage change is similar to the observed shifts in T_c . The peaks, however, do appear at fields higher than the observed dip fields in our $R(H)$ measurements. In Fig. 4.12 we combine the values for H_{dip} and H_{max} for the $40 \times 2 \mu\text{m}^2$ $\text{Cu}_{43}\text{Ni}_{57}/\text{Nb}/\text{Cu}_{43}\text{Ni}_{57}$ trilayer. It shows the constant value for $H_{\text{dip,n}}$, the jump to a lower value in the transition, and then the significant increase well below T_c .

We interpret the maximum in I_c as still caused by the domain state of the F layers. We do not know of similar data in the regime below $T = 0.9$, except for a report on Nb/Co bilayers where an increase in I_c of almost 50 % was found at around $t = 0.5$ [61]. Such a large value may well be an artefact caused by the sample geometry. As mentioned in Ch. 4.3, the geometry used here consists of simple bars with Au contacts. When the contact pads are included in the etching, all observations can change significantly, and in particular for the I_c enhancement we also find an increase of over 60 % as will be shown in Ch. 4.5. The smaller value (of order 1 %) also seems intuitively reasonable, since the superconducting order parameter is now well developed and the superconducting coherence length is small, making the sampling of the domain state by the Cooper pair less efficient. That leaves the question of the increase in coercive fields to values above 60 mT. In order to set these in perspective, we can estimate the maximum coercive field $H_{c,m}$ as expected for coherent rotation of the magnetization in the framework of the Stoner-Wohlfart model [34, 62]. For the field along the easy axis of magnetization, $H_{c,m}$ equals the anisotropy field $H_{an} = 2K_a/(\mu_0 M_s)$, with K_a the anisotropy constant and M_s the saturation magnetization. Taking a value of $6 \times 10^3 \text{ J/m}^3$ for K_a [63] and a value of 0.1 T for $\mu_0 M_s$ [58] leads to roughly $\mu_0 H_{an} = 0.1 \text{ T}$, still above the value we find for the coercive fields. This indicates that the superconducting state has a significant effect on the domain structure during the rotation of the magnetization, going in the direction of coherent rotation. As that would mean that the amount of domain walls becomes less, it would be another ground for the small effects observed in the superconductor far below T_c . Incidentally, similar effects of the superconductor on the magnetic state have been reported before. Magnetization measurements using a microfabricated Hall probe on Al/Ni submicron samples showed that shielding currents can reshuffle magnetic domains [64]. Similarly, magnetization measurements by SQUID magnetometry on S/F multilayers demonstrated changes in the magnetic state of the F layers in response to the onset of superconductivity

[65, 66].

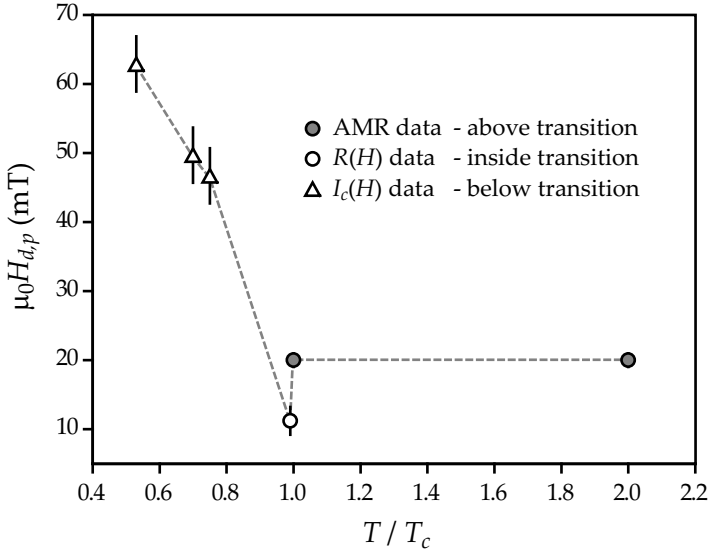


Figure 4.12: Collection of the measured dip and peak fields $H_{d,p}$ in our devices as function of temperature.

4.5 The influence of magnetic contacts

In measurements on the effects of stray fields and the spin-valve mechanism in F/S/F trilayers different sample geometries are used. In particular for lithographically structured samples it is tempting to include contact pads in the layout, since then only a single etch step is needed to fabricate the full device. Here we show that such a 'contact-included' geometry behaves very differently from a simple strip which has been contacted with Au leads. A SEM image of a contact included strip is shown in Fig. 4.3b, and Fig. 4.3c shows the geometry of the bonding pads and leads to the strip. Field-dependent resistance measurements on a contact-included $40 \times 2 \mu\text{m}^2$ bilayer for $T > T_c$ and $T < T_c$ are shown in Fig. 4.13 and Fig. 4.14 respectively, where they are compared

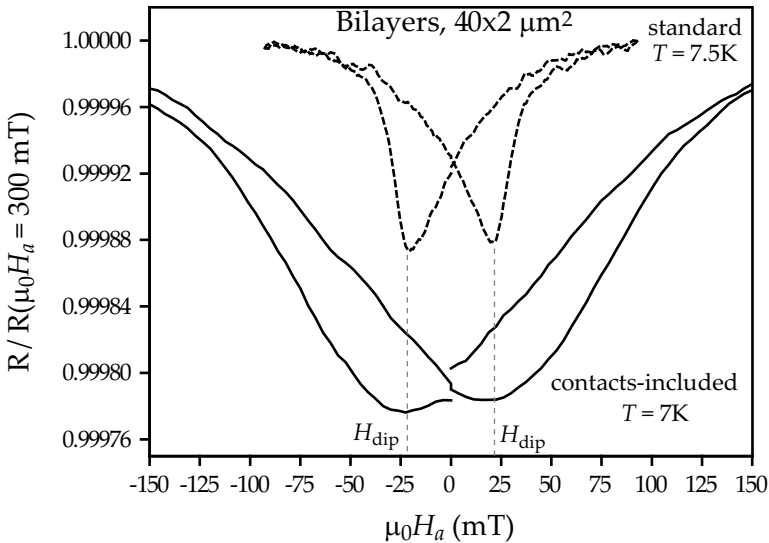


Figure 4.13: Resistance measurements on a contact-included $40 \times 2 \mu\text{m}^2$ Nb/Cu₄₃Ni₅₇ bilayer strip, compared to a strip-like standard device of similar size (Nb in the normal state). The temperatures of the measurements (7.5 K and 7 K) are just above T_c for both devices. The values of the dip field are indicated with the dotted lines.

to the results obtained on our standard bilayer strip. Above T_c the AMR dip shows a large broadening of about a factor 4, while the coercive field value is about the same with a value close to ± 22 mT. Below T_c the results are not very different, except that the location of the dip has shifted to a higher value coinciding with the observed coercive field. From these resistance measurement the "malfunctioning" of the device is not clear, but it does point towards a coercive-field dominated working of the device, from which we have shown is not the underlying mechanism in our strips. In Fig. 4.15 we show critical current measurements on a contact-included $40 \times 2 \mu\text{m}^2$ trilayer and compare them to the results obtained on the standard trilayer strip. The obvious difference is the size of the peak, which now shows an increase of nearly 60 percent! The location of the peak compares very well to the ones found on the standard device. Most likely, the T-shaped contact areas create a bottleneck for the supercurrent. Due to that shape, the magnetic anisotropy energies are likely to dominate the formation process and induce a very inhomogeneous magnetic profile localized near the contacts. This explains the large broadening of the AMR curve. Furthermore, this complex domain structure (or rather the stray fields produced by it) strongly suppresses the gap, an effect which apparently

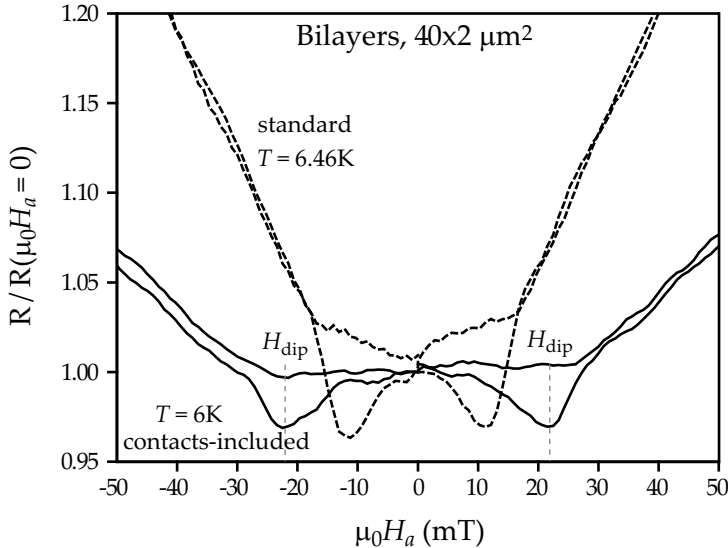


Figure 4.14: Resistance measurements on a contact-include $40 \times 2 \mu\text{m}^2$ Nb/Cu₄₃Ni₅₇ bilayer strip, compared to a strip-like standard device of similar size (Nb in the superconducting state). The temperatures of the measurements (6.46 K and 6 K) are in the resistive transition for both devices. The values of the dip field are indicated with the dotted lines.

disappears at higher fields, resulting in a large increase in critical current.

4.6 Conclusions

In conclusion, we investigated the effect of magnetic domains on a superconductor for the case of weakly ferromagnetic Cu₄₃Ni₅₇ by comparing magnetotransport measurements above and below the superconducting transition, both for bilayers and for trilayers resembling a spin-valve geometry, and for small structures as well as for large samples. We generally find that above the transition the resistance change is dominated by the AMR effect of the ferromagnetic layer (with a relative change of order 10^{-4}), while in the transition it is dominated by changes in the superconducting gap (with a relative change of order 10^{-1}). The AMR measurements show that domains are appearing in all our devices even down to the smallest bridges of $1 \mu\text{m}$ wide, with nearly identical hysteretic behavior and a coercive field value of 22 mT. In the samples with a $2 \mu\text{m}$ bridge a small but clear enhancement of T_c is found inside the transition which we claim to be due to the presence of mag-

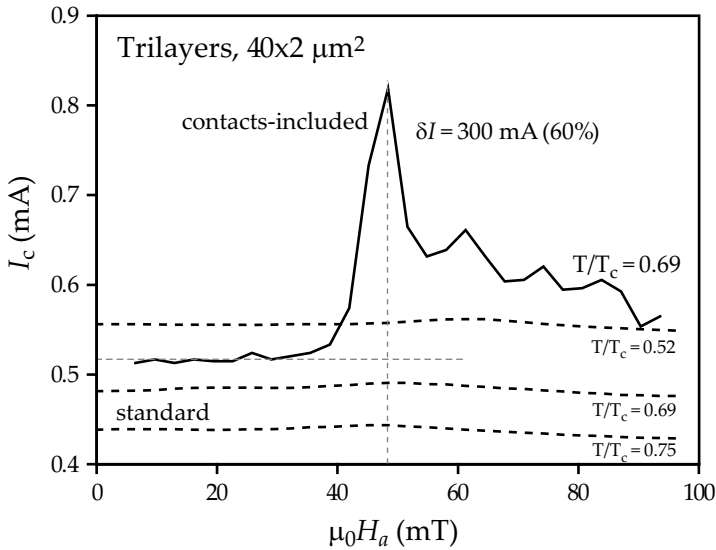


Figure 4.15: Critical current measurements I_c as function of applied magnetic field H_a on a contact-included $40 \times 2 \mu\text{m}^2$ $\text{Cu}_{43}\text{Ni}_{57}/\text{Nb}/\text{Cu}_{43}\text{Ni}_{57}$ trilayer strip, for a reduced temperature $T/T_c = 0.69$. The dashed lines show the data from the standard devices displayed in Fig. 4.11. Also indicated is the critical current increase in the peak as compared to the zero-field value.

netic domains. This enhancement is present in a limited field range, somewhat smaller than the range over which domains are present in the ferromagnetic layers. Still in the transition, the largest effect on the resistance is at a different field than the largest dip in the AMR. We believe that this reflects the difference in mechanisms giving rise to the two effects; on the one hand magnetization perpendicular to the current, on the other optimal sampling when the superconducting coherence length and the ferromagnetic domain sizes are of similar order. In samples with wider bridges even two dips are found in the transition, which is qualitatively ascribed to the evolution of domain states which appears to be possible in these wider samples. By going to lower temperatures and measuring the critical current (as a measure of the strength of the superconducting gap) we see that this enhancement is still present but the field at which it appears is shifting towards significantly higher values. This we attribute to the increasing strength of the superconductor which is forcing the ferromagnet to switch in a more single domain type of manner. The results on our micro-structured bilayers are very similar to the ones on our large-scale bilayer and micro-structured trilayers. All different measurement

show enhancement of the superconducting gap with a relative size of a few percent. This is very similar to all previous works on spin-valves involving weakly ferromagnetic CuNi, where the mechanism was believed to be the parallel vs anti-parallel orientation of the exchange fields. In view of our results, domain formation in the individual F-layers should be considered at least as an effect of similar importance.

Chapter 5

Superconducting spin-valve: strong ferromagnetic case

5.1 Introduction

To grasp the differences between the weak ferromagnetic based spin-valves, as discussed in the previous chapter, and the strong ferromagnetic based spin-valves, which are the main ingredient of this chapter, let us start by highlighting the key aspects of the former, in particular, the mechanisms involved in the working of the spin-valve device. The term "weak" in this context means not only that the ferromagnetic exchange energy E_{ex} is much smaller than the Fermi energy E_F , but additionally assumes identical spin bands (to achieve zero spin polarization) and neglects contributions from the dipolar fields generated by the magnetization resulting from E_{ex} . These two assumptions seem to be reasonable for small and homogenous exchange field H_{ex} , and for these systems, experimental data confirm the theoretical predictions [48, 49]. For the spin-valve system in the weak limit with homogeneous H_{ex} , the driving mechanism that leads to the T_c difference between the parallel (P) and anti-parallel (AP) alignment of the exchange fields, is based on enhanced dephasing of the induced pairs in P alignment. This originates from the momentum difference the induced pair obtains if the system is in P alignment, which it does not obtain in AP alignment (see Fig. 4.2). The enhanced dephasing causes a lowering of the Cooper pair density near the interface which leads to a T_c lowering. Inhomogeneities in H_{ex} , especially in the form of magnetic domains and domain walls, make that at a single S/F interface anti-parallel regions exist. The alignment is no longer purely parallel, and all the non-parallel fractions/regions contributes to a T_c enhancement. It is still the Cooper pair which needs to provide this coupling (and sample different directions of the exchange fields) and therefore, just as in the spin valve where the two F layers should not be separated more than a few times the superconducting coherence length ξ_S , the distance over which the inhomogeneity should appear (to make a difference) is also limited to a few times ξ_S . The use of weak limit theory is actually a forced restriction. The theoretical framework based on the quasi-classical Green functions is unable to deal with correlation between particles which are separated by energies of the order of E_F . This limit the models to ferromagnets with $E_{\text{ex}} \ll E_F$. Secondly, incorporating non-identical spin-bands (to deal with polarization) into the model gives severe mathematical difficulties, and thus identical (normal metal) spin bands are used, which is another reason to remain in the limit for weak ferromagnetism. What can be included are dipolar fields and inhomogeneities, and especially the latter has been included in the form of domain walls in S/F [41] or non-collinear magnetization in spin-valves [67]

In the previous chapter we studied Nb/CuNi devices, and in particular

the influence of the domains on the superconducting state. We found a contribution from these domains equally important as that from the P versus AP state in real spin-valve devices. However, a dominant contribution from dipolar fields, generated by those domains, was not found in any of the devices. In this chapter we continue this study on Nb/Py spin-valves, where the dipolar fields are much stronger. As we will show, in these devices the dipolar fields may become a dominant contribution and couple the magnetic states of both the Py layers in the spin-valve. Before we show the results obtained on the various devices, we first discuss what the effects of non-identical spin bands, encountered in "real" (or strong) ferromagnetic materials, on the superconducting spin-valve will be, on a qualitative level.

5.2 Polarized spin bands

We consider a thin layered F/S/F spin-valve in the dirty limit (i.e. all relevant length scales are much longer than the electron mean free path). The ferromagnets are homogeneously magnetized (single domain) and the exchange fields of the two ferromagnets are directed along the interfaces in either a parallel (P) or anti-parallel (AP) configuration. The dipolar fields of the ferromagnets are assumed to be much lower than $H_{c\parallel}$ (the parallel critical field strength) and do not affect the superconducting state (i.e. their pair breaking strength is zero). The exchange energies of the ferromagnets are neither in the so called weak-limit ($E_{\text{ex}} \ll E_F$) or the strong-limit ($E_{\text{ex}} \sim E_F$), so we have $E_{\text{ex}} < E_F$. As a result, the spin bands cannot be considered to be identical (weak limit) or decoupled ("perfect" strong limit). This, in consequence, gives rise to a spin dependent density of states, Fermi velocity, diffusion constant, etc. The (much) increased strength of the exchange field, compared to the weak limit, results in an enhancement of the suppression of the superconducting state. However, there is also an opposite effect due to the polarization of the spin bands. The Andreev reflections at a single interface become suppressed due to the presence of the minority spin band, more Cooper pairs are confined inside the superconductor, and the polarization therefore leads to a *reduced* suppression of the superconducting state. For the spin-valve, the essential process is the *crossed* Andreev reflection, in which the two electrons of the pair are removed in the opposite ferromagnetic banks. In the P configuration this always includes a minority spin band, while in the AP configuration both electrons can be accommodated in the majority bands. This means the AP configuration is now less confining and more efficient as pair breaker. In the limit of full spin polarization Cooper pairs have become fully confined in the P configuration, but still *can* leave the superconductor by crossed Andreev

reflections in the AP configuration. In other words, for weak magnets the P configuration suppresses superconductivity more strongly, but in the case of strong spin polarization it is the AP configuration, opposite to the weak limit result!

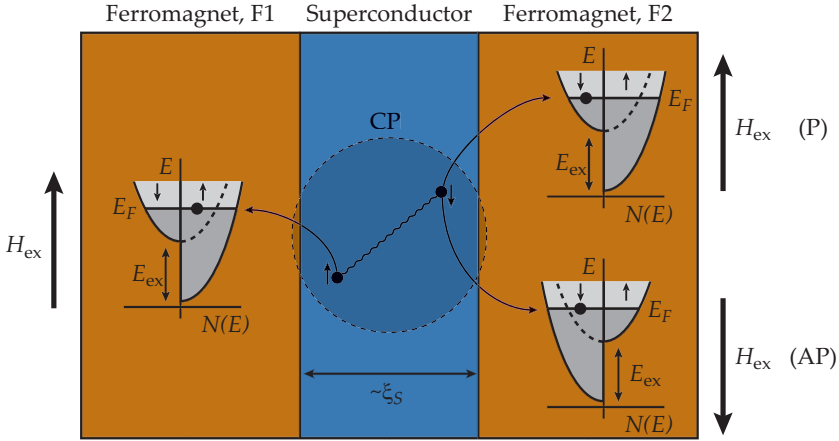


Figure 5.1: Comparing the parallel (P) and anti-parallel (AP) configuration of the ferromagnetic exchange fields H_{ex} in a superconducting spin-valve. Here, a Cooper pair (CP) couples the two ferromagnetic layers F1 and F2, with ξ_S the superconducting coherence length. In F1 the orientation of H_{ex} is "down" while in F2 the orientation is either "up" (AP configuration) or "down" (P configuration). The presented electron band structures represent strong ferromagnets with non-zero polarization.

A crossover from the established weak limit result to a reversal of the effect for strongly spin polarized ferromagnets is thus expected, but no theoretical predictions nor experimental data are available to confirm or refute this. To complicate matters, a relative increase of resistance when switching the magnetization may also be due to a change in the stray fields coming from the F layers. These issues are reflected in the literature. Results obtained on weak ferromagnet based spin-valves are all in line with the theoretical predictions, but that is not the case for systems involving strong magnets, such as Ni [50], $\text{Ni}_{80}\text{Fe}_{20}$ (Permalloy, Py) [51, 52, 53], Co and Fe combined [54] or Co [55]. In a number of these experiments, a *reversed* behavior is observed, giving a higher T_c in the parallel alignment. This is the case in reports on Nb/Py[51, 53], Nb/(Co,Fe)[54] and Nb/Co[55]. What all these reports have in common is that they do not make use of an anti-ferromagnetic pinning layer to pin the magnetization direction of one of the two F layers. The other experiments using strong ferromagnets all *do* use such pinning layer, improving the qual-

ity of the AP state, and there the "standard" spin-valve working is obtained. The non-pinned devices make use of F layers which intrinsically have different switching fields in order to switch them separately and create the AP alignment. This can be obtained by using different materials or thicknesses for the two F layers. The reports showing the reversed behavior do not agree on the suggested dominant mechanism, although most are in favor of a stray field based explanation, which in weak ferromagnetic based spin-valves was shown not to be (dominantly) present at all. A plausible argumentation is that the absence of a (strong) pinning layer (the switch field for the pinned AFM layer is quite a bit higher than the switch field of the F layer) leads to a less well defined AP state, where domains are present. The dipolar fields coming from these domains then have to overpower the effect of exchange field averaging, which is the standard (weak limit) mechanism. This fits with the following reports, which are all based on macroscopic sized samples. In the work of Stamopoulos *et al.* [53] a stray field coupling between the F layers is claimed, which act as source for the reversed behavior. In the work of Steiner *et al.* [54] it is concluded that the results strongly favor an explanation based on local stray fields. In the work of Carapella *et al.* [55] it is claimed that stray fields create a glassy vortex state, which is responsible for the reversal. A different mechanism connected to the polarization of the spin bands was claimed by Rusanov *et al.* [51] who used microscopic sized samples and was the first to observe this reversal. For such small samples, a deviant working of the device is not unexpected due to the lateral sizes competing with domain formation and switching.

To determine the T_c shift one typically measures the transition curve $R(T)$ from normal to superconducting state, and compares the P and AP alignments (preferably at equal but opposite external field). To gain more insight in the working of the device, a full field sweep at a fixed temperature on the transition curve can be made. The resistance ideally would remain constant until the device switches states, at which the resistance jumps to its different value. Especially in the work of Rusanov *et al.* [51] such (almost perfect) jumps/blocks were found and it was assumed this was directly related to a switching between the states (P and AP). However, the lowest resistance (highest T_c) was found in the P configuration, meaning a reversed result compared to the weak limit result. In this work we re-examined this issue.

Here we present a series of measurements on Nb/Py bilayers and spin-valve devices where we compare anisotropic magnetoresistance (AMR) effect in the normal state with the magnetoresistance measurements in the superconducting

state. We also present measurements of the depairing (critical) current I_{dp} far below T_c , and we explore both large scale devices (which were commonly used in previous works) and micro-sized devices. In particular we show that a dipolar coupling between the two Py layers disturbs the AP configuration in the spin-valve, and that the suppression of the stray fields outweighs the domain averaging effect of Cooper pairs.

5.3 Experimental details

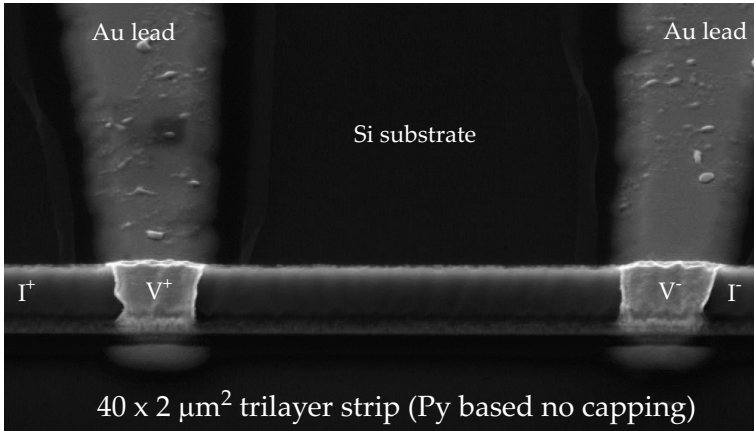


Figure 5.2: SEM image of a 4-probe $40 \times 2 \mu\text{m}^2$ spin-valve device. The distance between the voltage probes (V^+ and V^-) is $10 \mu\text{m}$ and the full length of the spin-valve wire is $40 \mu\text{m}$. Similar Au contacting leads for the current probes are at the end points of the wire (not shown).

Nb/Py layers were grown on Si(100) substrates by DC magnetron sputtering in a ultra high vacuum chamber with a background pressure of 10^{-9} mbar and an Ar pressure of $4 \mu\text{bar}$ for the Nb and $2.5 \mu\text{bar}$ for the Py, with Nb as bottom layer (see Ch. 3.1 for additional details). The substrate holders were equipped with a small magnet to determine the direction of easy axis for the Py layers and enhance the fast switching properties. The Nb layer thickness was kept at 50 nm for all samples, while for the Py layers thickness we used 20 nm and 50 nm. For our Py/Nb/Py spin-valve devices the bottom Py layer is 50 nm thick and the top Py layer is 20 nm thick. All devices have an additional 2 nm Nb capping layer added on top to prevent oxidation of the top Py layer. In Ch. 5.4.4 we show that not adding such a protective layer leads to a exchange-biased Py layer, likely due to anti-ferromagnetic iron-oxide formation. The Py has a degree of polarization close to 45 % and

a Curie temperature around 900 K. The purity of the Nb target is 99.95 % which yields a T_c of 9.1-9.2 K. Standard electron beam lithography was used to pattern both the micro-sized strips, with a length of 40 μm and a width of 1 to 4 μm , and the large scale devices ($2000 \times 200 \mu\text{m}^2$). In all cases, the direction of the strips is aligned with magnetic easy axis of the Py layer. The strips were etched using Ar ion-etching at an Ar pressure of 3 μbar with a background pressure of 10^{-6} mbar. Au contacts were sputtered in a second deposition step using a lift-off resist mask technique. A few nanometers of Ti were sputtered as adhesion layer for the Au. The contact geometry is 4-probe, with 10 μm spacing between the voltage probes for the micro-sized strips and 1000 μm for the large scale structures. Fig. 5.2 shows a SEM (scanning electron microscope) image of a $40 \times 2 \mu\text{m}^2$ spin-valve. This recipe is used for both bilayer and spin-valve, both for micro-sized and macro-sized devices. Typical

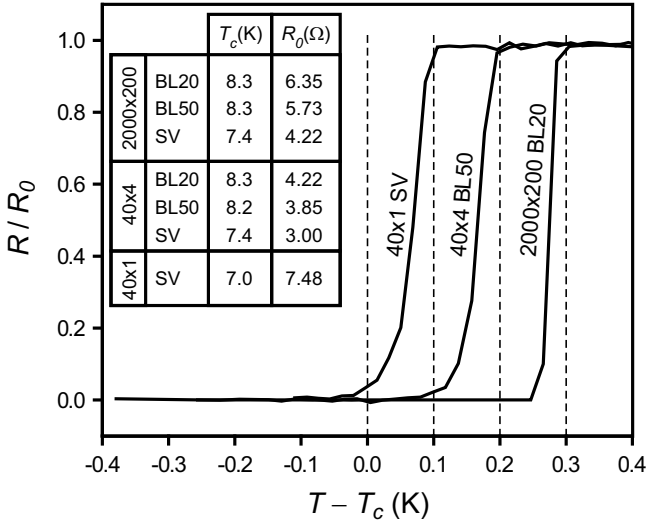


Figure 5.3: Temperature variation of the resistance around the transition temperature T_c (plotted as $T - T_c$) for (from left to right) a Py(50)/Nb(50)/Py(20) spin-valve (SV), a Nb(50)/Py(50) bilayer (BL50) and a Nb(50)/Py(20) bilayer (BL20), with numbers representing the layer thickness in nm. Resistance is normalized to the low temperature resistance R_0 and curves are shifted along temperature for clarity. Lateral dimensions of the devices are given in the graph in units of μm^2 . The table shows T_c and R_0 of all devices presented in this chapter.

transition curves (resistance R versus temperature T around T_c) for several of our devices are shown in Fig. 5.3, where curves are represented as $T - T_c$ (with T_c defined as the midpoint of the transition) and shifted for clarity. The

typical width of the transition is 50 to 100 mK. Also shown in the figure are all T_c 's and low temperature normal state resistances (R_0) for our devices. Note the difference in T_c between bilayers and spin-valves. The choice for the different layer thicknesses for the Py in the spin-valve device is to establish different coercive fields, making the device switchable from parallel to anti-parallel. The coercive fields of the 20 and 50 nm thick micro-sized Py strips are expected to be in the range from 0 to 20 mT [51] with a wider strip leading to a lower coercive field value (a large Py thin film of 20 nm thickness was measured to have a coercive field less than 0.5 mT). For our typical micro-sized strips (1 to 4 μm wide) we have always found a difference of about 5 mT between the two different thicknesses. However, as we will show later, the mutual influence of the exchange fields prevents a clean switching. The micro-sized elongated structures were chosen to promote single domain switching. They also have sufficiently large cross-sectional resistance to perform critical current (I_c) measurements. We performed anisotropic magneto-resistance (AMR) measurements (mainly at low temperature) just above T_c to see if and when domains appear in our Nb/Py bilayer systems, and then compare this to the AMR signal of the trilayer to see if the Py layers become coupled through their dipolar fields. The response of the superconductor is found by comparing these AMR measurements to the magnetoresistance measurements in the transition. All measurements were done in a standard ^4He cryostat with magnetic shielding to provide a low-noise environment. It is equipped with a superconducting coil to generate magnetic fields up to 1 T. All field measurements are performed with the direction of the applied field H_a along the long side of the strip, which implies $H_a \parallel I$ (the measurement current). The critical current (I_c) measurements are performed well below T_c , and probe the gap strength, enabling a comparison between P and AP below the transition area. A pulsed current method was used for these measurements, which is described in Ref. [59].

5.4 Results

5.4.1 $R(H)$ for $T > T_c$

Fig. 5.4 shows the result of $R(H)$ measurements on large scale Nb/Py bilayers and a Py/Nb/Py spin-valve, all with lateral dimension $2000 \times 200 \mu\text{m}^2$ and at a temperature of 9 K (Nb in normal state). All devices show the characteristic AMR dip, with a relative resistance change close to 0.06 percent. The spin-valve and bilayer with the thick Py layer (50 nm) show a very similar hysteretic curve with a coercive field value close to 1 mT, however, the bilayer with the thin Py layer (20 nm) shows a much broader dip with a coercive field close

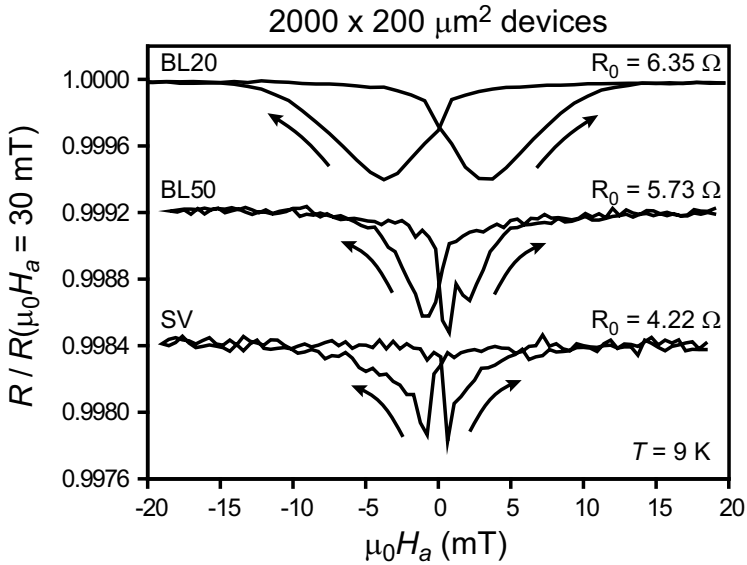


Figure 5.4: Resistance normalized to the value at 30 mT (called R_0 in the figure) as function of the in-plane applied field H_a on large scale devices with lateral dimension $2000 \times 200 \mu\text{m}^2$, all at temperature $T = 9 \text{ K}$. From top to bottom, a Nb(50)/Py(20) bilayer (BL20), a Nb(50)/Py(50) bilayer (BL50), and a Py(50)/Nb(50)/Py(20) spin-valve (SV), with numbers representing the layer thickness in nm. The BL50 and SV curves are shifted by respectively -0.0008 and -0.0016 .

to 3 mT. The same measurements but now on micro-structured strips, all with lateral dimension $40 \times 4 \mu\text{m}^2$, are shown in Fig. 5.5. For the spin-valve, block-shaped hysteretic dips appear with switches near $\pm 1 \text{ mT}$ and $\pm 3 \text{ mT}$, and with (again) a relative resistance change of 0.06 percent. For both the 50 nm thick and 20 nm thick bilayer we do not see any AMR dip coming out of the measurement noise, pointing towards a single domain type of switching. The noise level is similar for all three devices and about 0.01 percent, which is 0.3-0.4 m Ω in terms of absolute resistance value. It is significantly worse than the large scale devices and suggests that contacts to the strip are of lesser quality.

The appearance of this (seemingly) 2-step switch process in the micro-sized spin-valve is very different from the large scale spin-valve. Yet, the size of the resistance change is similar in both cases, and the observed switching fields of the blocks coincide with the coercive fields of the two different large scale bilayers (1 mT and 3 mT, respectively). To further explore this 2-stepped type

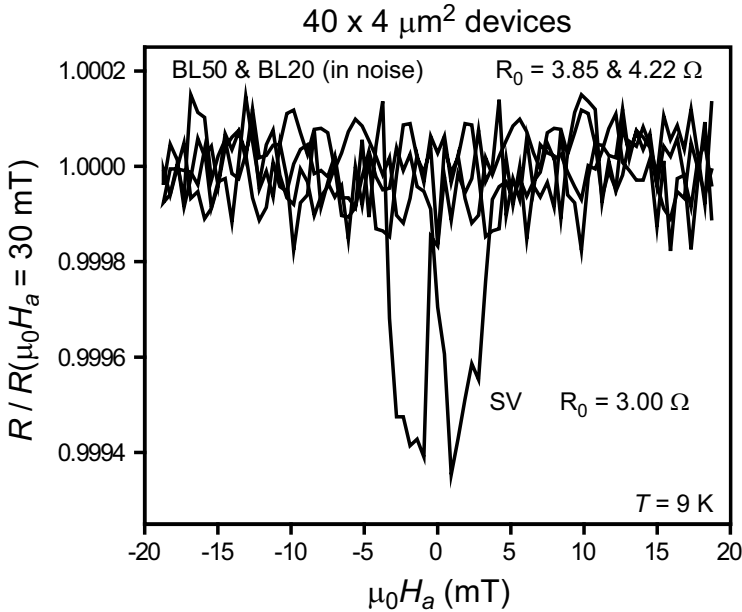


Figure 5.5: Resistance normalized to the value at 30 mT (called R_0 in the figure) as function of the in-plane applied field H_a on micro-sized devices with lateral dimension $40 \times 4 \mu\text{m}^2$, all with temperature $T = 9 \text{ K}$. The presented curve is from a Py(50)/Nb(50)/Py(20) spin-valve, while the results on the Nb(50)/Py(20) and Nb(50)/Py(50) bilayers (BL20 and BL50) are "flat" and within the noise of the spin-valve, with numbers representing the layer thickness in nm.

of switching we fabricated a narrower bridge ($1 \mu\text{m}$ wide) increasing the shape anisotropy energy, thus enhancing its importance in determining the possible domain states in the strips. Results are presented in Fig. 5.6 and show a series of $R(H)$ measurements at constant temperature ($T = 9 \text{ K}$) above T_c . Although no two curves are identical, there seem to be only a limited number of values for the applied field where a jump in resistance is seen, and also the size of those jumps take only few different values. The range over which hysteresis is found goes from $\pm (4 \text{ to } 14) \text{ mT}$, which is significantly higher than in the other devices. Also the size of the resistance change is about $10 \times$ higher than in our wider devices, implying more dense, and/or more perpendicular domains (perpendicular to the current direction).

In all the large scale devices (bilayer and spin-valve) domains appear during the switching, with a lower coercive field for a thicker Py layer. However,

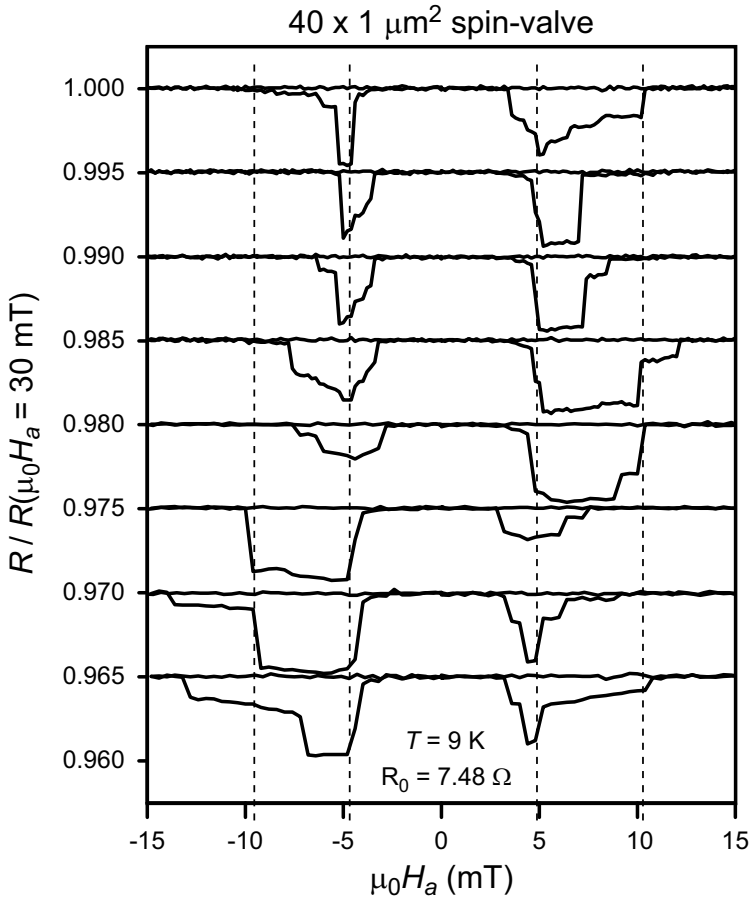


Figure 5.6: Resistance normalized to the value at 30 mT (called R_0 in the figure) as function of the in-plane applied field H_a on a $40 \times 1 \mu\text{m}^2$ Py(50)/Nb(50)/Py(20) spin-valve, with numbers representing the layer thickness in nm. All curves have a different magnetic history and are repeatedly shifted by -0.005. For all measurements the temperature was 9 K.

while the F layers in the bilayer devices can apparently switch freely, they evidently become magnetically coupled in the spin-valve device. This coupling appears to be such that a switching in the thinner layer (highest coercive field) is triggered by the switching of the thicker layer (lowest coercive field). In the $40 \times 4 \mu\text{m}^2$ bilayer strips, the switching is no longer accompanied by the formation and movement/rotation of domains over a relative broad field range, but rather makes a fast single switch. Most likely this is due to the enhanced shape anisotropy which favors single domain switching. In a spin-

valve device of the same lateral dimension the F layers become coupled, just as in the large scale spin-valve. Only now, the intrinsic type of switching of the separate layers is different, and this results in a two-stepped switch process for the spin-valve. We recall that a dip in the resistance of the AMR signal (in our devices) is representative for the appearance of inhomogeneities (domains) in the magnetization. Therefore, rather than a switch from parallel to anti-parallel, the blocks in the AMR signal indicate a switch from parallel to a domain state. The measurements on the $40 \times 1 \mu\text{m}^2$ spin-valve show that a variety of possible domain states exists, which can be entered during the two-stepped type of switching. In wider strips we have never observed such behavior.

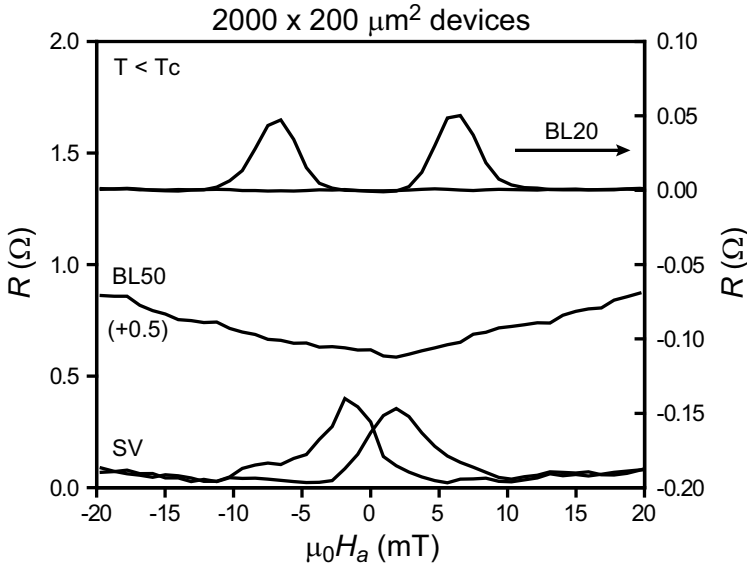


Figure 5.7: Resistance as function of the in-plane applied field H_a on large scale devices with lateral dimension $2000 \times 200 \mu\text{m}^2$, at temperatures on the low-end of the transition curve (Nb in superconducting state). From top to bottom, a Nb(50)/Py(20) bilayer (BL20), a Nb(50)/Py(50) bilayer (BL50) and a Py(50)/Nb(50)/Py(20) spin-valve (SV), with numbers representing the layer thickness in nm. The BL50 curve is shifted by +0.5 and the BL20 curve is on the right-hand scale.

5.4.2 $R(H)$ for $T < T_c$

A similar set of measurements is performed inside the transition, with Nb superconducting. The $R(H)$ are all taken at temperatures near the low-end

of the transition curve to improve temperature stability. The measured signal now comes predominantly from the superconductor which is shorting the ferromagnetic layers by percolation paths. Furthermore, any AMR features are no longer visible due to the (relative) high $\partial R/\partial T$ in the transition. Our typical 100 mK transition width, combined with a 10^{-4} relative resistance change corresponds to a temperature change of 0.01 mK, which is below our measurement accuracy of about 0.3 mK. Fig. 5.7 shows the result of $R(H)$

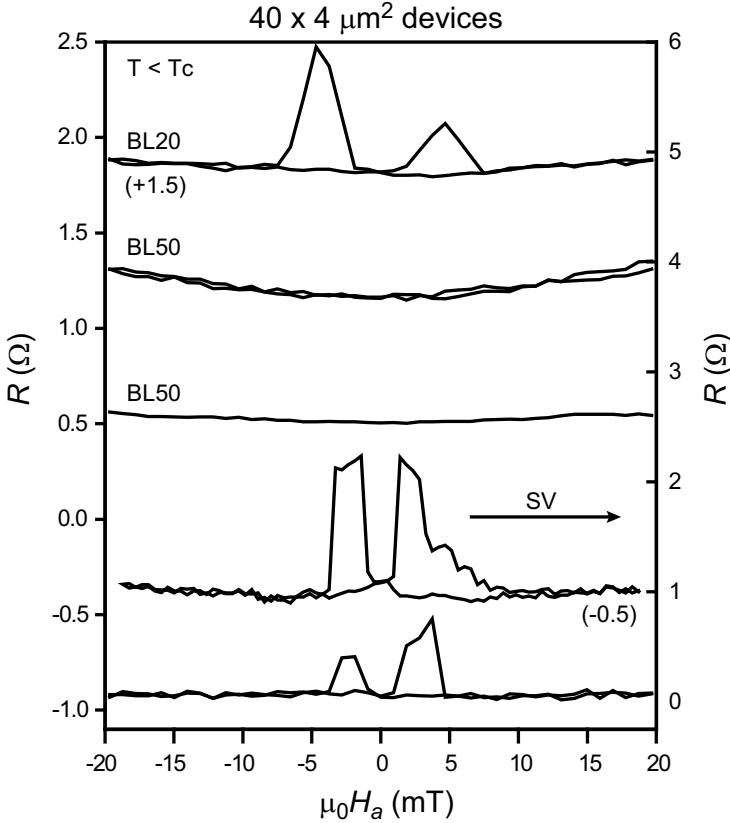


Figure 5.8: Resistance as function of the in-plane applied field H_a on micro-sized devices with lateral dimension $40 \times 4 \mu\text{m}^2$, at temperatures on the low-end of the transition curve (Nb in superconducting state). From top to bottom, a Nb(50)/Py(20) bilayer (BL20), 2x a Nb(50)/Py(50) bilayer (BL50), and 2x a Py(50)/Nb(50)/Py(20) spin-valve (SV), with numbers representing the layer thickness in nm. Two curves are shifted (by -0.5 and +1.5) as indicated. The SV curves are on the right-hand scale.

measurements on the large scale devices ($2000 \times 200 \mu\text{m}^2$). While the bilayer with the 50 nm thick Py layer does not show any hysteric feature at all, the

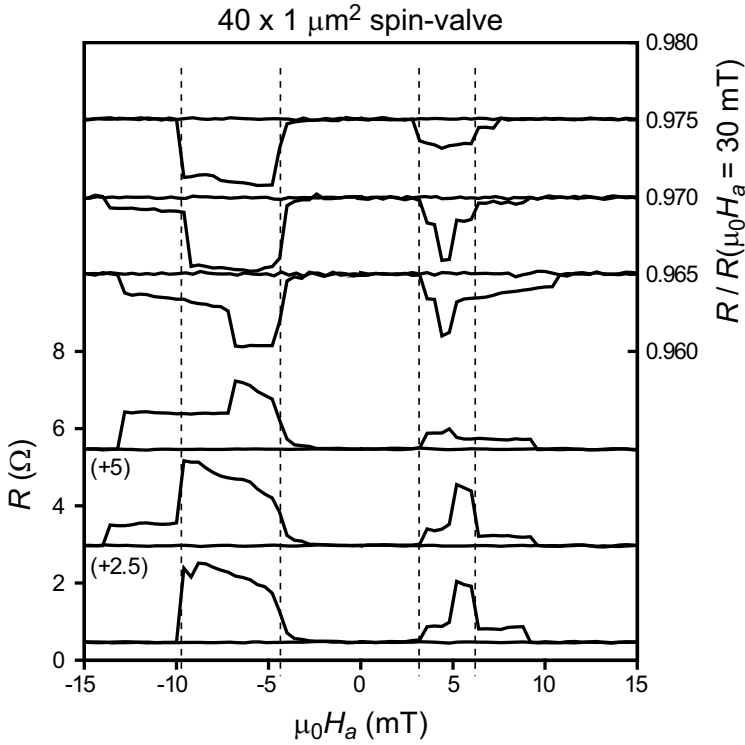


Figure 5.9: Comparison of the resistance as function of the in-plane applied field H_a on a $40 \times 1 \mu\text{m}^2$ Py(50)/Nb(50)/Py(20) spin-valve (numbers representing the layer thickness in nm) between temperatures on the low-end of the transition curve (Nb in superconducting state) and above the transition temperature T_c (Nb in normal state). All curves have a different magnetic history. Left-hand scale: results for $T < T_c$ with curves repeatedly shifted by +2.5 as indicated. Right-hand scale: results for $T > T_c$ taken from Fig. 5.6.

bilayer with the 20 nm thick Py layer shows clear hysteric peaks. The location of these observed peaks are around ± 6 mT, which is significantly higher than the corresponding AMR dips (in the same device) which are at ± 3 mT. Also the spin-valve shows such hysteric peaks, but located at lower fields around ± 2 mT (the corresponding AMR dips in the same device are at ± 1 mT). For the micro-sized devices ($40 \times 4 \mu\text{m}^2$) the same trend is observed (see Fig. 5.8) with again no hysteric feature in the bilayer with the 50 nm thick Py layer, while the bilayer with the 20 nm thick Py layer and the spin-valve both do show hysteric peaks. In case of the bilayer, the peaks are located at ± 4 mT (a lower value compared to the large scale devices) and still resemble the shape

of peaks. For the spin-valve the peaks are now really block-shaped, indicating again a 2-stepped type of switching, and have switching fields at ± 1 mT and ± 4 mT. In Fig. 5.9 we present the $R(H)$ measurements on the thinner spin-valve ($40 \times 1 \mu\text{m}^2$), and make a direct comparison with the obtained $T > T_c$ results (of the same sample, see Fig. 5.6). Block-shaped peaks are observed with switches at ± 4 and ± 10 mT (or ± 14 mT). Furthermore, there is a striking resemblance between the observed blocks for $T > T_c$ (dips) and $T < T_c$ (peaks). All observed switching fields in the $R(H)$ measurements on the large scale and micro-sized devices are collected in Table I:

	2000 \times 200			40 \times 4			40 \times 1
	SV	BL50	BL20	SV	BL50	BL20	SV
$T > T_c$	1	1	3	1-3	-	-	4-14
$T < T_c$	2	-	6	1-4	-	4	4-14

Table I: Switching fields in mT for the various structures and samples, both above and below T_c .

5.4.3 $I_c(H)$ for T well below T_c

The presented transport measurements so far, all focus on temperatures closely around the transition ($T \sim T_c$). To study the working of the spin-valve well below T_c we conducted a series of critical current measurements as function of applied field, $I_c(H_a)$ by measuring the current I - voltage V characteristic. We used 3 ms current pulses, with an interval of several seconds and increasing in amplitude until the critical current is reached and the superconductor is driven in the normal state. The sample is initially cooled down in zero field condition and the first measurement at a fixed temperature always starts in zero applied field. The obtained I - V curves all showed a sharp jump from almost zero voltage to the normal state, which indicates that we are measuring a depairing current rather than the onset to vortex flow. This we (consistently) found before on S-films and S/F bilayers [59, 57, 68]. The measurement is thus directly sensitive to the amplitude of the superconducting gap, which limits the critical current. Additionally, the value of I_c is well defined due to the sharp transition. The results for the $40 \times 4 \mu\text{m}^2$ Nb/Py spin-valve are shown in Fig. 5.10, where $I_c(H)$ curves are presented at four temperatures well below T_c , which, in terms of the reduced temperature $t = T/T_c$ go down to $t = 0.5$. All data show a block-like dip for the increasing applied field (coming from negative saturation) with switching fields around 0.5 mT and 3.5 mT, after which the curve becomes constant. The observed switching fields of the blocks do not show a temperature dependence, but do show a diminishing effect for

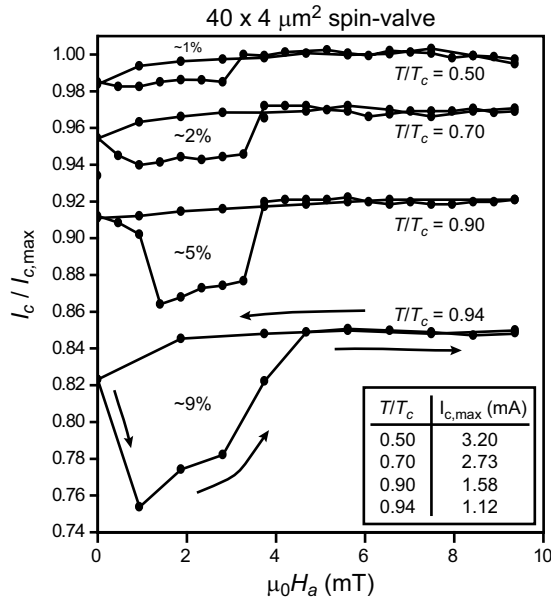


Figure 5.10: Critical current measurements I_c , normalized to the maximum observed value $I_{c,max}$ per temperature, as function of the in-plane applied field H_a on a $40 \times 4 \mu\text{m}^2$ Py(50)/Nb(50)/Py(20) spin-valve. The curves represent different reduced temperatures T/T_c and are shifted for clarity by -0.03, -0.08 and -0.15. The indicated percentages are the relative sizes of the dips.

decreasing temperature. The uncertainty in the determination of I_c is about the step size for the increase in current ($1 \mu\text{A}$). We interpret the decrease of I_c in the hysteretic region as a suppression of the superconducting gap. Because the gap increases in strength for lower temperature, it is not strange to see a diminishing effect of the percentage change. The switching fields coincide with the values found in the transport measurements close to T_c (see Fig. 5.5 and Fig. 5.8). Fig 5.11 shows the $t = 0.94$ curve up to higher field values, and the standard decrease of I_c due to applied field becomes visible. Additionally, the inset shows the actual $I - V$ measurement at the highest used field (125 mT).

5.4.4 Exchange biased Py

All presented data so far has been on devices where the top Py layer is covered by a thin Nb layer to protect it from oxidizing. Magnetoresistance measurements on a $40 \times 2 \mu\text{m}^2$ bilayer strip *without* such capping layer are presented in Fig. 5.12, where $R(H)$ at room temperature ($T = 300 \text{ K}$) is compared with

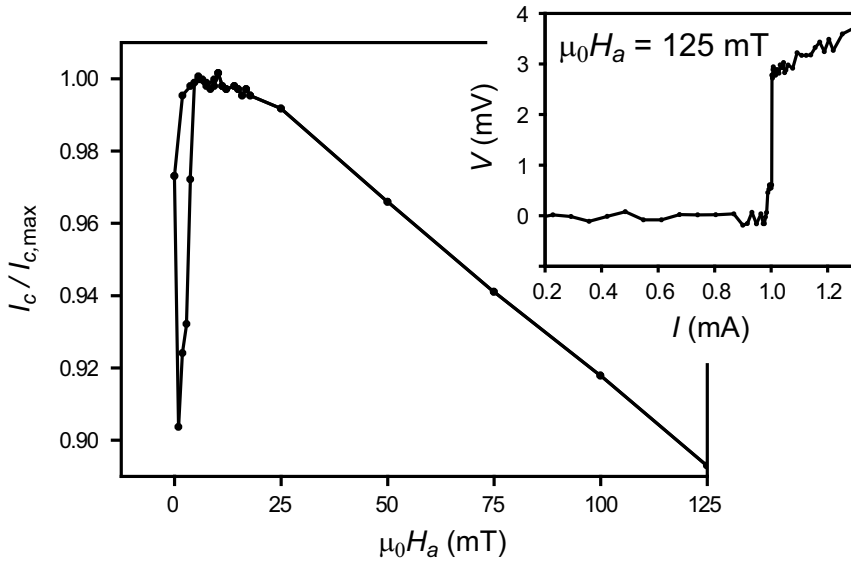


Figure 5.11: High field behavior of the $T/T_c = 0.94$ critical current measurement as presented in Fig. 5.10. The inset shows the current voltage measurement of the curve for $\mu_0 H_a = 125$ mT.

low temperature ($T = 10$ K). At room temperature the AMR signal contains the typical dips. They are symmetrical around zero field, with a coercive field of ± 6 mT, and with a relative resistance change of 0.005. At low temperature the dips have become broader, the coercive fields have become larger, but the curve is no longer symmetric around zero field. The coercive fields are now at -14 mT and 9 mT, which indicates an exchange bias of 2.5 mT (such that unbiased the coercive fields would be symmetric again at ± 11.5 mT). We expect this exchange bias to be the result of the formation of anti-ferromagnetic Fe_2O_3 in the Py layer.

5.5 Discussion and conclusion

Combining the results from all measurements above, the data sketch a coherent picture of the behavior of Py/Nb/Py spin-valve structures. For temperatures *above* the transition (Nb in normal state) we find that the resistance changes are dominated by the AMR effect of the Py layers, with a relative resistance change of order 10^{-4} . In large scale devices, where domain formation is not limited by the size of the sample, the observed resistance dips in the bilayers with 20 nm and 50 nm thick Py appear at different fields. For the spin-

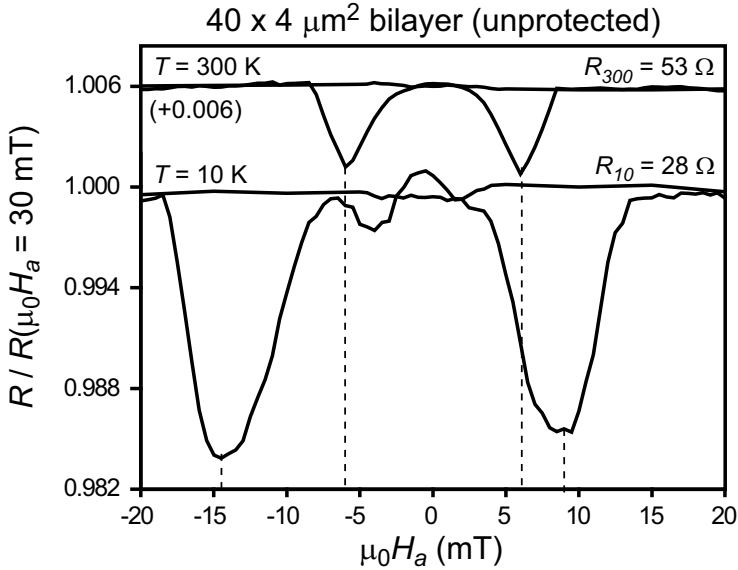


Figure 5.12: Resistance normalized to the value at 30 mT as function of the in-plane applied field H_a on a $40 \times 4 \mu\text{m}^2$ Nb/Py bilayer, for $T = 300$ K and $T = 10$ K. The respective resistances are indicated by R_{300} and R_{10} . Both the Nb layer and Py layer are 20 nm thick.

valve structure we then expect to see all four resistance dips in the AMR, however, we observe a behavior very similar to the bilayer with 50 nm thick Py. Going to the microscopic regime, we no longer observe any dips at all in the AMR signal of the bilayers, pointing towards a fast single domain type of switching. Surprisingly, in the spin-valve we *do* observe resistance changes in the AMR signal. A 2-stepped switching has appeared by going from large scale to micro-sized spin-valves, most strongly pronounced in the thinnest ($1 \mu\text{m}$ wide) spin-valve structure. We believe this is a strong indication for a magnetic coupling between the two Py layers by dipolar/stray fields, which are locking domains into a (meta)stable configuration. For temperature *below* the transitions (Nb superconducting) we observe peaks in the resistance now dominated by changes in the superconducting gap, with a relative resistance change of order 10^{-1} . Especially in the $1 \mu\text{m}$ wide spin-valve, these peaks are mirror images of the dips in the corresponding AMR signals. This implies that 1) the superconductor does not influence/change the switching behavior of the spin-valve, and 2) suppression of the superconductor is a direct effect of the presence of the stray fields connecting the two Py layers. Such coupling between the two F layers has not been found in any of the experiments using

antiferromagnetic pinning layers. In the bilayers we only observe these peaks in the devices with 20 nm thick Py (and not in the devices with 50 nm thick Py). This we attribute to different types of domain walls. It is known that for very thin Py layers the domain wall becomes of the Néel type, while for thicker Py layers it is Bloch type [69]. The crossover between the two is around a Py thickness of 35 nm, implying Néel walls in our 20 nm thick Py bilayer and Bloch walls in our 50 nm thick Py bilayers. Calculations on stray fields generated by domain walls shows a significantly higher magnitude for Néel walls than for Bloch walls [70], which we believe is the source of the observed difference in our bilayers. No traces are found of an enhancement of the superconductivity by domain averaging from Cooper pairs, which we *did* observe in our CuNi based devices and is the established weak limit result. We thus conclude that the stray field contributions coming from the domains dominate over this averaging effect. By going to lower temperatures and measuring the critical current, which is a direct measure for the superconducting gap strength, we observe that the suppression of superconductivity is still present. The fields at which the suppression occurs overlaps with the peaks in the magnetotransport measurements and do not change with temperature. This indicates that also a well developed gap is not changing the switching of the Py layers, and likely the spin-valve is still dominated by the stray fields. In our $I - V$ measurements we do not see traces of a vortex flow, while the stray fields connecting the two F layers should result in vortices. However, since the domain state seems to be unaffected by the gap, we believe it strong enough to keep any vortices in place. Effectively, all vortices generated by the stray fields are strongly pinned by the (rigid) domain state itself.

Chapter 6

Probing reversed proximity in the spin-valve using LE- μ SR

6.1 Introduction

The main characteristics of the (superconducting) proximity effect of the S/F interface are the emergence of spin triplet correlations and the oscillatory nature of the induced order parameter in F. For these interfaces, the key parameters of S are the superconducting gap energy Δ and the superconducting coherence length ξ_S , while in F they are the exchange energy E_{ex} (of the exchange field H_{ex}) and coherence length ξ_F . For thin film, where we usually are in the dirty limit, the layer thicknesses become important as well and the following relations apply: $\xi_S = \sqrt{\hbar D_S / \Delta}$ and $\xi_F = \sqrt{\hbar D_F / E_{\text{ex}}}$, where D_S and D_F are the diffusion constants of the S and F layer respectively. While usually the focus is on the leaking of Δ (superconducting correlations) in F, the inverse process occurs as well, which is the leaking of E_{ex} (ferromagnetic correlations) in S. This would lead to a certain amount of magnetization in the S layer. Calculations performed recently indicate that this can be a measurable effect [31]. However, the commonly used measurement techniques, such as transport measurements or surface probing, are unsuited for detecting the reversed proximity effect, at least, in the way they are conventionally applied. The mechanism of the reversed proximity essentially is a form of spin polarization, or actually a spin dependent suppression, of the Cooper pairs near the S/F interface. For the Cooper pairs which have an electron impinging the F layer, the pair breaking strength experienced is lowest if the electron spin is aligned with the exchange field. The result is that more (a higher density) of these aligned Cooper pairs remain compared to the other orientations. This (partial) alignment of the Cooper pair is in real space and when the electron with parallel spin direction is near the interface, the other electron of the Cooper pair (which has an anti-parallel spin direction) is roughly at a distance ξ_S from the interface. In the situation where the parallel electron is mainly located on the F side of the interface, the S side of the interface will have a higher density of anti-parallel electrons, while in the situation that the parallel electron is still mainly on the S side, the net spin polarization oscillates from parallel (near the interface) to anti-parallel (at roughly ξ_S from the interface), and back to neutrality (at roughly few times ξ_S away from the interface). This mechanism is shown in Fig. 6.1.

To investigate this (possible) induced magnetism in the superconductor we need a measurement technique that can locally probe the magnetic moments in the superconductor near the F/S interface, "near" meaning down to the scale of ξ_S , which is about 10 nm in our devices. Low energy muon spin rotation

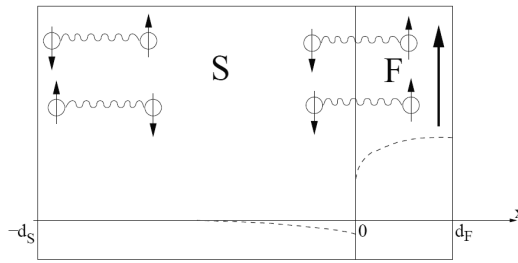


Figure 6.1: Schematic of the inverse proximity resulting in polarized Cooper pairs. The dashed lines indicate the field profile. Figure taken from [31].

(LE- μ SR) is one such technique, other are e.g. the (optical) Kerr effect, and Nuclear Magnetic Resonance, and both these techniques have recently been used to investigate the inverse proximity effect [71, 72]. We come back to this in the discussion. LE- μ SR makes use of spin polarized muons, which act as local magnetic field probes when implanted into a sample. The implantation (or stopping) profile depends on the muon energy and becomes broader for higher energies. Low energy muons mean energies in the keV range, which allows for probing down to the nanometer scale. All our LE- μ SR measurements were done at the Paul Scherrer Institut (PSI) in Villigen (Switzerland) in collaboration with S. Lee and co-workers from St. Andrews University (Scotland). The LE- μ SR technique is a rather recent development, developed at PSI in early 2000 (see [73] for a review on this). A nice demonstration of this technique on related spin-valve samples are the experiments conducted on Fe/Ag/Fe [74] and Fe/Pb/Fe [75] thin films. The first experiment revealed the existence of a spin density wave across the normal metallic Ag spacer layer. The second experiment showed that such spin density wave still exists when the spacer layer becomes superconducting (Pb has a bulk superconducting transition temperature of 7.2 K). These spin density waves stretch across the full spacer layer making it ideal for LE- μ SR. The spin density wave is also a manifestation of spin polarization but now from the conduction electrons. Two important differences between a spin density wave and the inverse proximity effect are the length over which the effect takes place, and the number of oscillation they produce in the spin polarization profile. The spin density wave easily covers the full S layer thickness while making multiple oscillations (order of 10), while the inverse proximity effect is focussed near the interfaces and makes a half to a full oscillation.

low energy muon spin resonance and low energy muon-spin relaxation are also commonly used for this abbreviation

6.2 Description of the measurement technique

In this section we first introduce the principle of the muon spin rotation technique, and then give a detailed description of the working of the experimental setup.

6.2.1 Principle of muon spin rotation

The essential principle of the muon spin rotation technique comes down to be able to follow the time evolution of a single muon spin. In the presence of a local magnetic field (B), the muon starts to precess around this field (Lamor precession) with a frequency (ω_μ) given by:

$$\omega_\mu = \gamma_\mu B \quad (6.1)$$

where $\gamma_\mu = 851 \text{ MHz T}^{-1}$ is the gyromagnetic ratio for the muon. When the muon decays it emits a positron at an angle θ with respect to the momentary muon spin direction (which is the most preferred direction). The probability distribution for this angle is given by:

$$W(\theta) = 1 + \frac{1}{3} \cos(\theta) \quad (6.2)$$

which is an energy averaged value of the positron spectrum. By detecting the emitted positron, (a fraction of) information is recovered about the muon spin at the moment of the decay. When placed between two positron counter detectors, the value of the magnetic field (B) can be recovered by making a large number of single muon measurements (events), by simply counting the positrons and record the time span of each event. Two main prerequisites are that each event should be about identical in the starting situation (such that the results can be added) and the muon has to be detected before entering the sample to start the measurement timer. Thus, a monochromatic spin-polarized muon beam is essential for the experiment. Fig. 6.2 shows a simplified schematic of the muon spin rotation setup. The initial muon spin direction at $t = t_0 = 0$ is pointing towards the left positron counter detector and the corresponding angle is ϕ_0 , with a anticlockwise precession direction of frequency ω_μ . At a certain time $t > t_0$, the muon spin has rotated over an angle $\omega_\mu t$ and the muon spin direction has become $\phi(t) = \omega_\mu t + \phi_0$. The chance that the muon decays at that instance is given by $(1/\tau_\mu)e^{-t/\tau_\mu}$, with τ_μ the muon lifetime. Throughout this chapter we use the convention that t_0 signals the moment that the actual precession starts with ϕ_0 being the starting angle of the muon spin, measured with respect to the muon spin pointing towards the left detector (in the figure this implies $\phi_0 = 0$). Furthermore, the starting time is set to zero, $t_0 \equiv 0$. The detectors do not cover all possible angles, leaving a range of angles for which the emitted positron will not be detected,

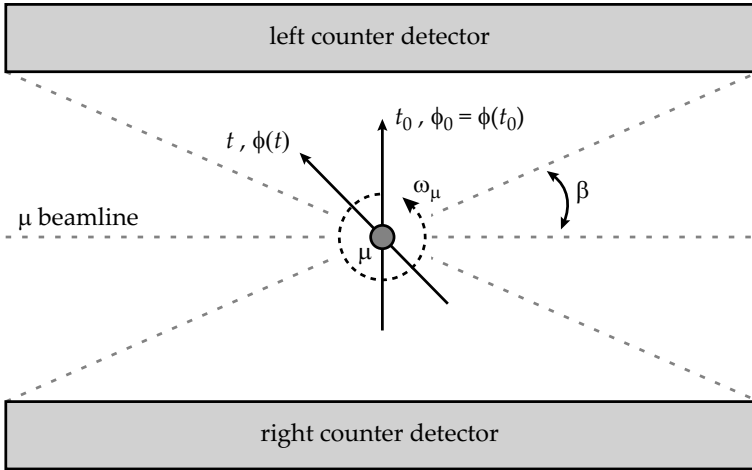


Figure 6.2: Basic setup of the muon spin rotation experiment. Here t_0 and ϕ_0 are the initial time and starting angle of the muon (μ) spin. At time $t > t_0$ the spin direction has rotated anticlockwise with frequency ω_μ and has now angle ϕ .

this "dark-angle" is parameterized by β . To calculate the probability that at t a positron is detected on the left (right) detector we need to integrate the positron emission angle probability function $W(\theta)$ over all values of theta that cause the positron to arrive at the left (right) detector, and multiply by the chance that the muon actually decayed at that time. These probabilities are given by:

$$\begin{aligned}
 P_L(t) &= \frac{1}{2\pi\tau_\mu} e^{-\frac{t}{\tau_\mu}} \int_{\theta=\theta_1}^{\theta_2} \left(1 + \frac{1}{3} \cos(\theta)\right) d\theta = \frac{\beta'}{\tau_\mu} (1 + A_0(t)) e^{-\frac{t}{\tau_\mu}} \\
 P_R(t) &= \frac{1}{2\pi\tau_\mu} e^{-\frac{t}{\tau_\mu}} \int_{\theta=\theta_1+\pi}^{\theta_2+\pi} \left(1 + \frac{1}{3} \cos(\theta)\right) d\theta = \frac{\beta'}{\tau_\mu} (1 - A_0(t)) e^{-\frac{t}{\tau_\mu}} \\
 A_0(t) &= \frac{P_L(t) - P_R(t)}{P_L(t) + P_R(t)} = -\frac{1}{3} \frac{\sin(\phi(t) - \pi\beta') - \sin(\phi(t) + \pi\beta')}{2\pi\beta'} \\
 \theta_1 &= -\phi(t) + \beta - \pi/2, \quad \theta_2 = -\phi(t) - \beta + \pi/2 \\
 \beta' &\equiv \frac{\pi - 2\beta}{2\pi}, \quad \phi(t) = \omega_\mu t + \phi_0 = \gamma_\mu B t + \phi_0
 \end{aligned} \tag{6.3}$$

Here, the pre-factor $1/(2\pi)$ is to normalize the probability function $W(\theta)$ and β' is the angular fractional covering of a detector plate. Furthermore, $A_0(t)$ is the so-called asymmetry signal which weighs the difference between counted event on the left and right detector. It contains all physical information about the muon precession, and thus the magnetic structure, and plays an important role in the data analysis. In the limit of full covering detector plates ($\beta \rightarrow 0$) the asymmetry value has a maximum of ± 0.21 , while in the limit of point detectors ($\beta \rightarrow \pi/2$) it has a maximum value of ± 0.33 . Although the asymmetry is improved for a point-like detector, the counts per second on the detector

will be much decreased. Model detector signals and asymmetry are plotted

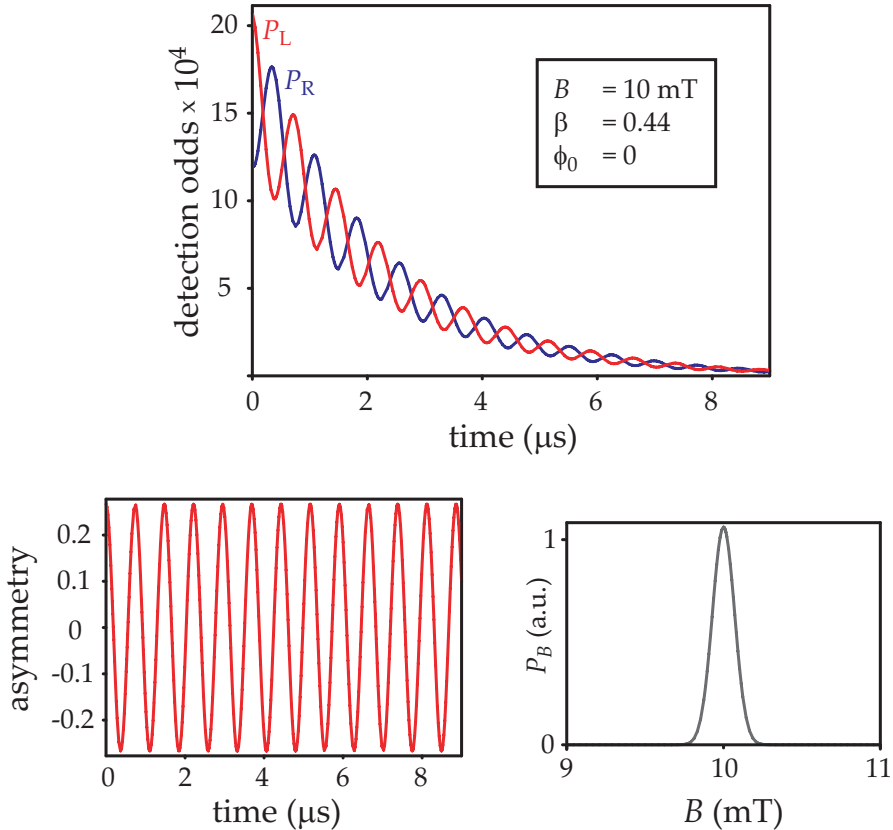


Figure 6.3: The model detector signals P_L and P_R , the asymmetry between them A_0 , and the Fourier transform of the asymmetry which gives the distribution of the field

in Fig. 6.3 for parameter values as given in the plot. Also shown is that by making a Fourier transform of the asymmetry signal, the muon frequency (or frequencies in general) is (are) recovered and appear as peaks in the spectral plot. This is a way to find out which dominating frequencies (and thus local magnetic field strengths) are present in the sample. In practice, the more advanced "maximum entropy based spectral analysis" (maxent) is used to recover this frequency spectrum. In the real experiment, the muon is implanted into the sample and is not located at a precisely known position. Instead, it has a probability to be at a certain position which depends on the muon energy. These probability profiles can be calculated. So, not only do we need

multiple measurements to collect data from muons which decayed at different times (to follow the spin rotation), we also need a large number of measurements to probe the full spatial distribution of the implanted muons. A typical order of events to count is 10^6 and curves similar to the model signals are then obtained in the form of histograms originating from the counted events at the positron counter detectors. An important difference with the real experiment is that the muons/experiment are/is subjected to decoherence, which results in a damping of the asymmetry signal. Although the frequency spectrum of the asymmetry signal gives important information about the dominating frequencies (local magnetic fields), it does not tell from which part of the sample they originate. The spatial information is lost! Reconstructing the spatial distribution of the magnetic moments inside the sample from the raw data is thus not possible, and the game to play is: assume a certain distribution, calculate the corresponding frequency spectrum (or asymmetry signal), and test how well this fits the measured data.

6.2.2 Experimental setup

At PSI, the muons for the experiment are generated in a secured area and are then directed to the different measurement setups via the main muon transport line. A schematic of the experimental setup is shown in Fig. 6.4, where the entrance point of the muons to the setup is the moderator chamber. The muon transport line and the connecting lines/chambers are all pumped down to a pressure of about 10^{-7} to 10^{-8} mbar.

Generation of the muons

Muons (μ) are unstable elementary particles, decaying in vacuum with a lifetime of $2.2 \mu\text{s}$. They are spin-1/2 particles and are positively or negatively charged, with an elementary charge of e . Effectively, the negative muon is like a heavy electron with a mass about 207 times larger, while the positive muon is like a light proton with a mass about 9 times smaller (both types are unstable though). They can be observed in cosmic rays with typical energies in the GeV to TeV range at a (very low) rate of about 100 muons penetrating a square meter every second at sea level. The muon originates from the decay of pions (π), which in accelerators can be produced by bombarding a light nuclear target with high energy protons. Charged pions decay into a muon and neutrino (ν):

$$\begin{aligned}\pi^+ &\rightarrow \mu^+ + \nu_\mu \\ \pi^- &\rightarrow \mu^- + \bar{\nu}_\mu\end{aligned}\tag{6.4}$$

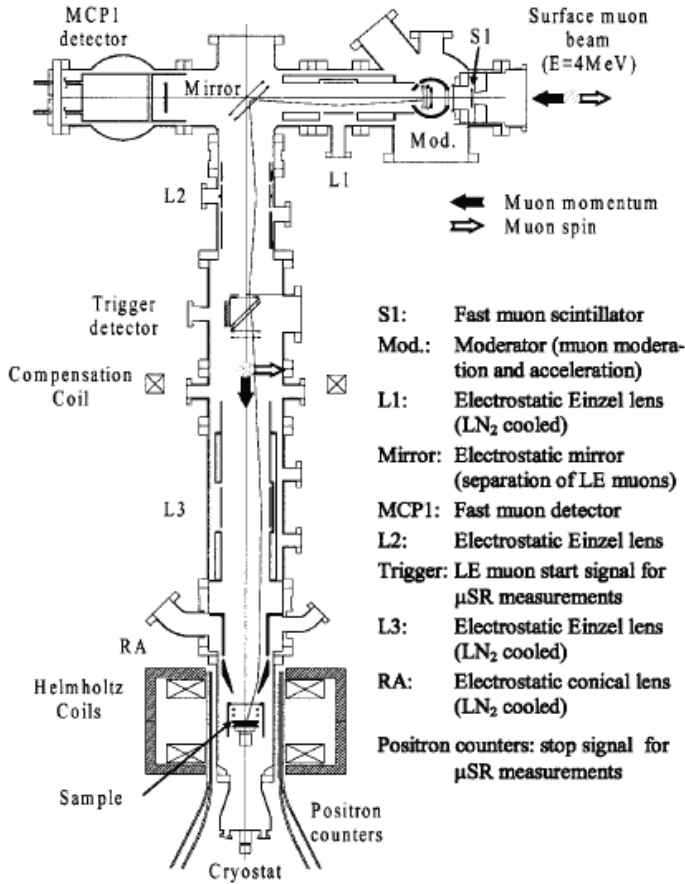


Figure 6.4: The measurement setup area/unit, taken from [73]. Starting from the entrance point for the muon beam, it shows the moderation chamber, the mirror, the trigger chamber and sample chamber, all connected by electrostatic lenses to direct and focus the muon beam.

Due to conservation laws, the produced positive muon (μ^+) has its spin antiparallel to its momentum, while for the negative muon (μ^-) they are parallel. It is possible to create a nearly monochromatic beam of nearly 100 % spin polarized positive muons by selecting the so-called surface muons. These muons are produced by positively charged pions that lost all their energy during the proton bombarding processes and decayed at rest near the surface. The reason that those muons form a near monochromatic beam is that they all have a unique energy of 4.1 MeV and a momentum of 29.79 MeV/c. This process is not possible for the negative muon because the produced π^- particles are

captured much faster inside the target material. Such a monochromatic beam of positively charged, spin polarized surface muons is directed to the measurement area where the muons are implanted into a sample to perform the actual measurement. The energy of 4.1 MeV of these surface muons is sufficiently low for measuring bulk samples, but the stopping profile (the implantation depth distribution) is far too broad (about 0.1 to 1 mm) to investigate thin films. For that, the energy needs to be lowered down to the keV range.

Moderating the muon energy

In the measurement area the incoming surface muons first arrive in the moderator chamber, where a fraction of the muons become trapped into the moderation shield. This shield is a thin layer of a condensed Van der Waals gas (typically argon, neon or N₂ cryosolids) deposited on a much thicker Aluminum foil (about 100 μm thick). In our experiment we used a Ar/N₂ shield with thicknesses of 10 nm and 1.2 nm respectively, at a temperature of 10 K which is necessary for the stability of the shield. The purpose of this shield is to lower the energy of the trapped surface muons down to about 10 eV. The energy lowering mainly takes place in the (relative thick) Aluminum foil, while the deposited Ar/N₂ layer creates a minimum threshold value for the energy of the outgoing muons because of its insulating nature, with a bandgap of 10 to 20 eV. Afterwards they get accelerated again and reach an energy up to about 15 keV. The muon beam (which now consists of surface muons and low energy muons) then gets focussed by an electrostatic Einzel lens onto an electrostatic mirror. This mirror separates the low energy muons (about 15 keV) from the surface muons (about 4 MeV), since it only reflects muons with energies up to few 10s of keV. Muons with higher energies pass straight through it, and are absorbed by the fast muon MCP1 detector. The mirror reflects the momentum, but not the spin of the muon, which remains pointing into the initial direction.

The trigger chamber

The now monochromatic beam of low energy, positively charged, spin polarized muons is focussed by a second electrostatic Einzel lens onto the trigger detector. This detector contains a thin carbon web which emits some electrons whenever a muon passes through and such trigger signals the start of a (new) single measurement. This measurement is completed when a positron counter detector (surrounding the sample space) counts the positron which is emitted by the muon when it decays. The rate at which muons pass through the trigger detector was about 750 per second during our experiments, which gives an

approximate average time window of 1 ms between subsequent passing muons. This is much larger than the muon life time ($2.2 \mu\text{s}$) so in most cases the single measurement is complete before a new incoming muon is detected in the trigger chamber. The waiting for the positron detection is actually aborted if either a second muon passes the trigger detector or a time window of about $12.5 \mu\text{s}$ has passed, and the event is discarded.

The sample chamber

To focus the muons onto the sample, a final electrostatic Einzel lens is used. The sample itself is mounted such that it is electrically insulated and can be set to a high voltage (up to $\pm 12 \text{ kV}$) in order to accelerate or decelerate the muons before implantation. In this way the energy of the muons can be fine-tuned and the appropriate stopping profile can be selected. Fig. 6.5 shows the stopping profile for the actual sample we measured, which was a Si/Py(50)/Nb(50)/Py(20)/Nb(2) thin film, where numbers represent the layer thickness in nm. The depth is measured starting from the top surface of Nb(2) layer, meaning that the center of the Nb layer is at a depth of 47 nm. As can be seen, a muon energy of 5 keV has the main peak just inside the Nb and thus focusses on the interface region. Increasing the muon energy shifts and broadens this main peak, such that for energies of 10 keV to 15 keV the full Nb layer is probed, with a focus near the central part of the layer. The muon energy thus takes the role of the spatial coordinate directed normal to the surface, and ideally, the magnetic moments in the sample only vary along this normal direction. The experiment is performed in the presence of an applied magnetic field which is homogeneous across the sample space and parallel to the sample plane. Fig. 6.6 shows a top-view of the sample space where the incoming muon μ^+ arrives from the left side (with momentum p and spin s). The magnetic field bends the muon flight path through the Lorentz force it exerts on them. This is compensated for by the transverse electrical field E set by the high voltage potentials RAL and RAR. These voltages needs to be fine-tuned such that the spot of the muon beam is at the center of the sample and not towards one of the two positron detectors. In practice the spot is always slightly more on one of the two sides such that the detector on that side detects more then the other detector. This affects the asymmetry but that can be corrected for (in the limit of small displacement error) by multiplying one of the two counter detector signals to re-balance this difference. For our experiments, this adjusting parameter α for the left counter detector was about 0.99, indicating a fairly good alignment of the muon beam. For the applied magnetic field we used 10 mT directed along the vertical. This field sets a base frequency of $f = 1.35 \text{ MHz}$ for the muon precession which comes down

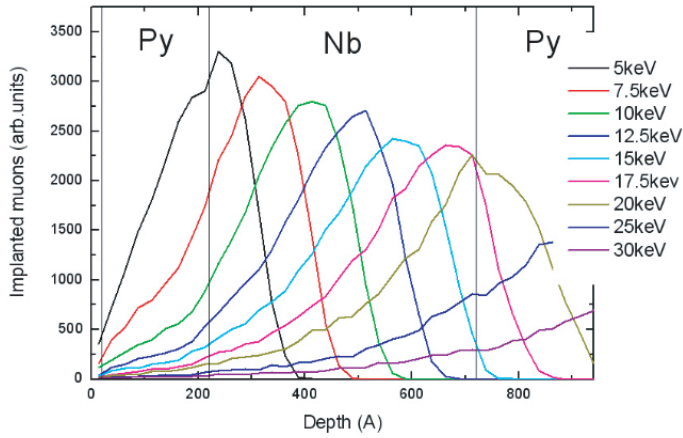


Figure 6.5: Calculated muon stopping profile for a Nb(2)/Py(20)/Nb(50)/Py(50) layered sample (numbers representing the layer thickness in nanometer) for different implantation energies. The depth = 0 is at the top surface of the Nb(2) layer.

to almost 3 rotations per τ_μ , making it a reasonable base frequency to follow.

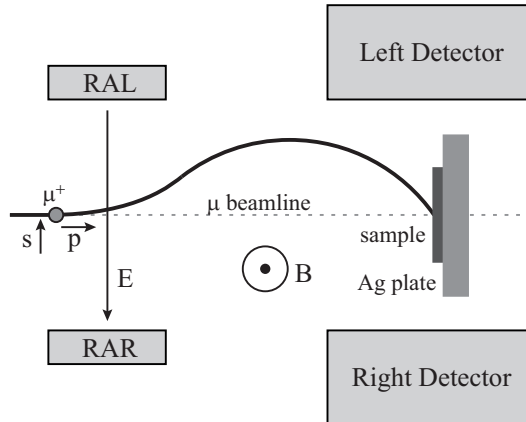


Figure 6.6: Top-view schematic of the sample space showing the muon path of flight, which is centered onto the sample by the electrical field E and induced magnetic field B . RAL and RAR are high voltage potentials creating E .

Implanting a muon

The muon is now adjusted for implantation energy and focussed at the sample center. It penetrates the sample (or the Ag backing plate, because the spot is slightly larger than the sample itself) and comes to rest at time t_0 , measured with respect to the moment it passed the trigger chamber. Subsequently, it starts precessing around the local field it experiences until the moment it decays into a positron (and a muon antineutrino and electron neutrino). The measurement stops when this positron is detected by any of the positron counter detectors (which are outside the UHV area). The direction in which the positron is emitted is preferentially along the momentary spin direction of the muon, but its distribution is energy dependent with the energy-averaged form given by Eq. 6.2. Due to the near monochromatic near 100 % polarized muon beam, the initial spin and momentum state of all incoming muons are practically identical, and all the single measurements (events) are thus coherent and can be added. Typically several million of events are necessary to obtain high enough statistics for further data analysis (i.e. for each depth to be probed by enough muons to cover the spread in the positron emission angle). The primary sources of decoherence of the muons are fluctuations in the local field (changes to the sample) and the momentum spread of the beam itself (changes to the muon), which is supposed to be some 10s of eV. The field fluctuations disturb the precession frequency itself which directly leads to decoherence if it is significant compared to the local (average) value. A direct implication of the momentum spread of the beam is a spread in the time-of-flight, resulting in a spread of some 10s of nanoseconds in the time t_0 . The result is a sharp non-exponential decay of detector signal during the first to 20 to 30 ns after t_0 . Therefore, data collected during these early times are left out of the data analysis. The time resolution of the detection system is close to 200 ps, which is the used size for the time bins. A valid positron count adds 1 count to the time bin which contains the relative time of decay (relative to the moment the muon was detected in the trigger detector). To give an idea of the histogram filling, a time span of 2.2 μ s (the muon life time) is divided in 11000 time bins of 200 ps, and the full time window of the measurement contains about 66000 time bins. Collecting 10^7 events (our typical measurement statistics) then gives an average filling of about 75 events per time bin per detector, which means about 450 events in the early time bins of the detector (when taking an exponential decay with a characteristic time of 2.2 μ s).

6.3 Results

6.3.1 Experimental details

The sample used for the LE- μ SR measurements is a Py(50)/Nb(50)/Py(20) trilayer thin film, with the numbers representing the layer thickness in nm. To cover a large fraction of the sample plate, 16 pieces of $1 \times 1 \text{ cm}^2$ were put together forming a $4 \times 4 \text{ cm}^2$ mosaic (see Fig. 6.7). All pieces were made under identical conditions, with the same deposition parameters as for the Py/Nb/Py spin-valve devices (see Ch. 5). The pieces are glued to the sample plate with conducting Ag-paste, all with the orientation of the easy axis aligned with the applied field during the measurement. This conducting Ag-paste is also used to electrically connect the top layers of the individual samples to ground them to the sample plate (such that the final implantation energy of the muons can be tweaked by setting a high potential). With this covering, it is expected

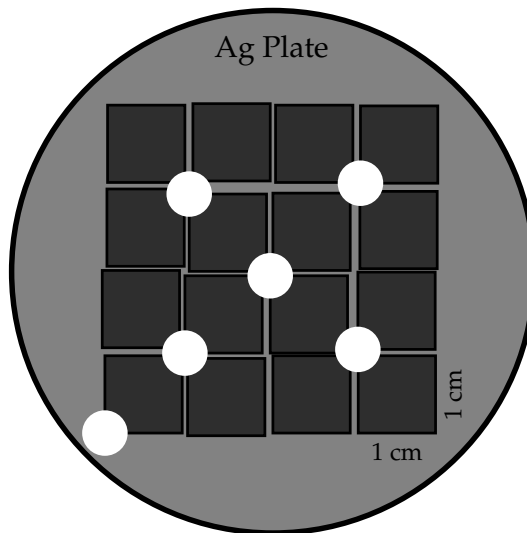


Figure 6.7: Sketch of the sample pieces forming a 4×4 mosaic, glued on the round sample plate. White dots represent the conducting Ag-paste, electrically connecting all pieces to the sample plate.

that around 90 % of the incoming muons will hit the sample [76]. The rest of the muons gets implanted into the Ag backing plate, where only the external field is probed. The sample plate is mounted into the sample chamber with its surface perpendicular to the incoming muon beam. The sample pieces are oriented such that the easy axis of the Py is aligned along the setup vertical, which is parallel to the external field direction, which is significantly

higher than the coercive fields of the thin Py films, which are close to 0 mT. During the experiment the applied field was 10 mT directed from bottom to top. The corresponding muon precession frequency is 1.35 MHz with a anticlockwise rotation direction when looking from above. The rotation plane is perpendicular to the field direction and the initial spin direction points towards the left counter detector (see Fig. 6.6). Measurements were performed at two different temperatures, either at $T = 10$ K (Nb in normal state) or $T = 4.5$ K (Nb in superconducting state). For each temperature, the sample is probed at eight different muon implantation energies, $E_{\text{muon}} = 5, 5.5, 6, 6.5, 7, 7.5, 10$ and 12 keV. The lowest muon energy has its stopping distribution focussed near the S/F interface, while the highest two covers the full sample, with a focussed near the center of the Nb layer. Furthermore, for $T = 4.5$ K we did the measurements for both a "field cooled (FC)" and "zero field cooled (ZFC)" treatment. For FC the applied field was kept on during cooldown from normal state to superconducting state, for ZFC the fields was switched off during cooldown. In total we thus have 24 data sets, where for each data set we collected 10^7 counts (positron detections). In terms of pure measurement time these 10^7 counts comes down to almost 4 hours of measuring (at a rate of 750 incoming muons per second).

6.3.2 Fitting of the data

To obtain information about the magnetic profile we attempt to fit the measured detector signals (the real-time raw data) rather than analyzing the Fourier transform of the asymmetry data (the frequency spectrum). An example of a maxent analysis (Fourier transform of the asymmetry signal) is given in Fig. 6.8, where the data is from a muon energy of 5 keV with $T = 10$ K. As is clear from the graph, no outstanding features appear other than the main peak which is centered at a field of 9.79 mT. This is the main reason why we focussed our data analysis on the real-time data. The strategy we applied starts by making a best fit to the raw detector data using the Levenberg-Marquardt algorithm [77]. Including the spatial dependence of the magnetic profile is not possible (each location should then be parameterized by an unknown precession frequency), instead a simple uniform profile is used.

The fit functions

The detector signals as derived before (Eq. 6.3) give the fractional chance of counting the positron at time t . This is for a single muon at a fixed position. When adding these contributions from many (coherent) muons we have to correct for decoherence (or dephasing). Taking a (standard) exponen-

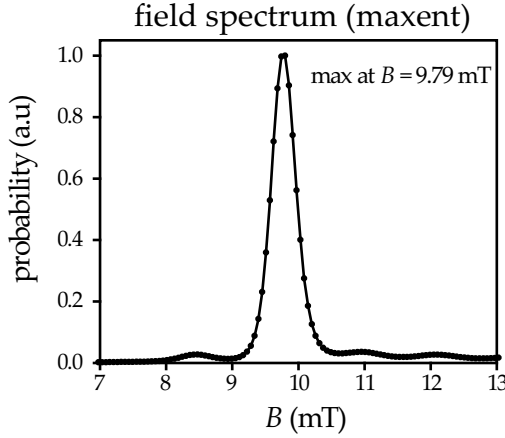


Figure 6.8: Probability distribution of the local fields in the Nb layer, for the data set with muon energy of 5 keV and temperature of 10 K. Results are obtained using a maximum entropy (maxent) analysis.

tial dephasing for the asymmetry with a characteristic time τ_θ , the fractional counting probabilities become:

$$P_{R,L}(t) = \frac{\beta'}{\tau_\mu} \left(1 \mp A_0(t) e^{-\frac{t}{\tau_\theta}} \right) e^{-\frac{t}{\tau_\mu}} \quad (6.5)$$

Furthermore, the incoming muon is implanted in one of the following 3 areas: 1) the Ag backing plate, 2) the Nb layer, or 3) the Py layer. Although we cannot include a full spatial dependence into the fitting, it is rather straightforward to distinguish between these three areas, all characterized by a single average field B_i , with i being the label of the area. These areas then all have a different asymmetry function A_0^i and a fractional chance for the muon to stop in that area of P_i , with $P_{Ag} + P_{Nb} + P_{Py} = 1$. The muons implanted in the Ag backing plate and the Nb layer all experience a field equal to, or close to the applied field and are expected to experience a very similar dephasing. However, in the Py the internal field is orders of magnitude larger than the applied field. In fact, it is far above the maximum detectable frequency of 50-70 kHz of the LE- μ SR setup, and thus can be treated as instantly dephased ($\tau_\theta \rightarrow 0$). Adding this the fractional chances become:

$$P_{R,L}(t) = \frac{\beta'}{\tau_\mu} \left(1 \mp \left(P_{Ag} A_0^{Ag}(t) + P_{Nb} A_0^{Nb}(t) \right) e^{-\frac{t}{\tau_\theta}} \right) e^{-\frac{t}{\tau_\mu}} \quad (6.6)$$

In the correct case, the detector detects the positrons coming from the decay of the muon under investigation. However, this signal is polluted by anomalies

(like scattered positrons). This we model by adding a (small) time independent probability of such fake events which turns out to work very well. The final fit equations, the number of counted events as function of time, are obtained by simply multiplying by the fractional numbers by a general amplitude N_0 (which is not exactly equal to the total number of counted event due to re-normalization).

$$\begin{aligned}
 N_R(t) &= N_0\beta' \left(1 - \left(P_{\text{Ag}}A_0^{\text{Ag}}(t) + P_{\text{Nb}}A_0^{\text{Nb}}(t) \right) e^{-\frac{t}{\tau_\theta}} \right) e^{-\frac{t}{\tau_\mu}} + N_{f,R} \\
 N_L(t) &= \frac{1}{\alpha}N_0\beta' \left(1 + \left(P_{\text{Ag}}A_0^{\text{Ag}}(t) + P_{\text{Nb}}A_0^{\text{Nb}}(t) \right) e^{-\frac{t}{\tau_\theta}} \right) e^{-\frac{t}{\tau_\mu}} + N_{f,L} \quad (6.7) \\
 A_0^i &= -\frac{1}{6\pi\beta'} (\sin(\phi(t) - \pi\beta') - \sin(\phi(t) + \pi\beta')) \\
 \phi(t) &= \gamma_\mu B_i t + \phi_0
 \end{aligned}$$

Here $N_{f,R}$ and $N_{f,L}$ account for the pollution, and we incorporated the setup alignment factor α to correct for the misalignment of the muon spot (see text related to Fig. 6.6). When we subtract the linear offsets $N_{f,R}$ and $N_{f,L}$, the asymmetry signal becomes very simple:

$$A(t) = \frac{\alpha N_L(t) - N_R(t)}{\alpha N_L(t) + N_R(t)} = \left(P_{\text{Ag}}A_0^{\text{Ag}}(t) + P_{\text{Nb}}A_0^{\text{Nb}}(t) \right) e^{-\frac{t}{\tau_\theta}} \quad (6.8)$$

Details of the fitting

The parameters to fit can be divided into the following groups: (i) P_{Ag} , β' , τ_θ , α , the setup/system constants; (ii) B_{Nb} , P_{Nb} , ϕ_0 , the implantation energy (and system temperature) dependent parameters; and (iii) N_0 , $N_{f,L}$, $N_{f,R}$, the amplitudes of the signal. The parameter $\tau_\mu = 2.197 \mu\text{s}$ is a natural constant with a well determined value and for the applied field we use $B_{\text{Ag}} = 9.79 \text{ mT}$, which we found was the actual value of the applied field (see Fig. 6.8, which is taken at low muon energy where the contribution of the background is dominant over the sample contribution). The main strategy we follow is to first determine the fit parameters of group (i) by stacking all data sets (to improve the accuracy) and next to fix those values and fit the individual data sets to determine the parameters of group (ii) as function of the implantation energy. By fitting the stacked data, we also obtain values for the parameters of group (ii); however, these values represent some average value for the different implantation depth. The parameters of group (iii), although not depending on the implantation energy, also have to be determined for each individual data set because they directly depend on the number of counts, and this number is close to 10^7 , but not exactly the same for all sets.

Before fitting we re-bin the original time bins with a factor of 32, such that now each bin is approximately 6.4 ns. This we mainly do to smooth the raw data. Furthermore, we adopted the convention for the fit functions to set the time at the starting of the precession (t_0) to zero. However, this time is not precisely known and neither is it the same for different implantation energies. This (small) time deviation leads to a small difference in the starting angle ϕ_0 , which thus must be a free parameter during the fitting. For all fits, we use the $t = 650$ ns after triggering as the t_0 time, while we start the fitting at $t = 750$ ns. All presented data have the time such that $t = 0$ is at the moment of the trigger detection. The fitting follows an iterative process which minimizes the sum of the squared errors according to the Levenberg-Marquardt algorithm. Let $y(x_i)$ be the measured data at discrete points x_i , with an experimental error that can be approximated by a Gaussian distribution with standard deviation σ_i . If the fit to this data is given by $y_{\text{fit}}(x_i)$, then the statistical (total) error of the fit is given by $\text{Err} = \chi^2/x_N$, with x_N the number of points to fit, and χ^2 defined by:

$$\chi^2 = \sum_i (y_{\text{fit}}(x_i) - y(x_i))^2 / \sigma_i^2 \quad (6.9)$$

With this definition of the total error, a value close to 1 means in general a good fit. This is because in that case, the difference between the fit and the real data is on average within the error of the experimental data itself.

Fitting the stacked data

Fig. 6.9 shows the fit result of the stacked detector data. Blue and red dots are the measured right and left detector signals respectively and the fits to them are the solid black lines. The inset shows a zoom-in of a part of the main plot (numerical values along the axis are in the same units as the main plot). Also shown in the inset are the values obtained of the fit parameters of group (i) and the errors of the fits. The values of the parameter of group (ii) are not shown here, instead they are slightly more accurately determined in a next fitting shown in the Fig. 6.10. In general, all obtained values are very reasonable and the quality of the fit is good. At $t = 0$ the muon is detected and the initial flat part is the time it takes for the muon to get implanted. The contribution to the signal coming from the Ag backing plate $P_{\text{Ag}} = 20.2\%$ is a bit more than the expected 10%, which is likely due to our pieces not closing perfectly and having several big silver-paste drops on top for the grounding. The value of β implies an effective angular covering of about 70%, the dephasing time is close to $1\ \mu\text{s}$, which is equivalent to about 1.4 periods of a muon in the applied field. A value of 0.988 for the correction parameter α means a well-centered

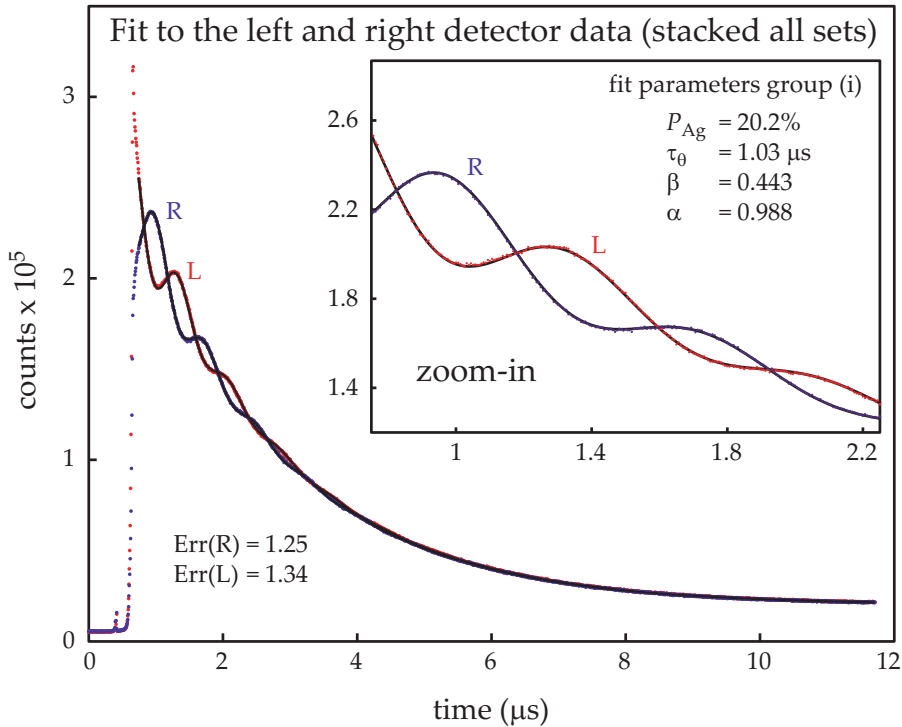


Figure 6.9: Best fit for the stacked detector signals. Blue/red dots are the measured right/left detector data, with the solid black lines the obtained best fits with errors $\text{Err}(R)/\text{Err}(L)$. The inset is a zoom-in and also shows the values of (part of) the fit parameters (the ones independent on the muon implantation energy).

beam (about 1 % misalignment). These parameter values are from here on fixed for all further fitting.

From the left and right detector signals the asymmetry signal is constructed (see Eq. 6.8) and the fit results are given in Fig. 6.10, where an additional linear offset is included to ease the fitting to correct for the remaining misalignment. The red dots are the asymmetry signal with the fit given by the solid black line. The values obtained for the fit parameters are given in the plot and the most interesting one is B_{Nb} which apparently (on average) is *lower* than the background field of 9.79 mT. An additional comparison fit (grey line) is made with fixed $B_{Nb} = B_{Ag} = 9.79$ mT. Although the visible change is small, the error of the fit has drastically worsened. The value for P_{Nb} seems very reasonable comparing to the muon implantation profile and the value for ϕ_0 corresponds to a starting angle of about 21° (which would take a muon pre-

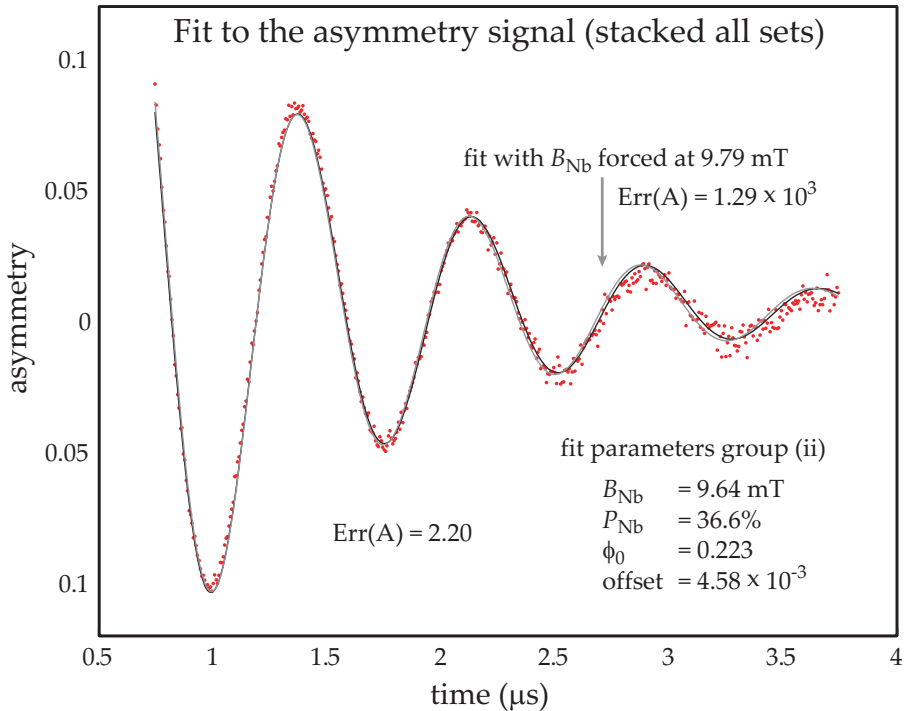


Figure 6.10: Asymmetry signal of Fig. 6.9. The solid black line is the best fit with error and parameter values as given in the plot. A second fit (grey line) is made with $B_{Nb} = B_{Ag}$ from which only the error is given.

cessing in the applied field about 40 ns). These extracted values are *averages* and we will make fits to the single data sets to obtain the muon-energy dependence of these parameters, which correlates to the spatial dependence of the parameters. In total, from the stacked fittings we have obtained:

setup constants		parameters to fit (obtained averages)	
P_{Ar}	= 20.2 %	$\langle P_{Nb} \rangle$	= 36.6 %
τ_θ	= 1.03 μs	$\langle B_{Nb} \rangle$	= 9.64 mT
β	= 0.443 rad	$\langle \phi_0 \rangle$	= 0.223 rad
α	= 0.988		

Fitting the individual data sets

For each individual data set, fits are made to the asymmetry signals. For muon energies of 5 keV and 10 keV, these fits are shown in Fig. 6.11, where from top to bottom we have the $T = 4.5$ K (ZFC), $T = 4.5$ K (FC) and $T = 10$ K

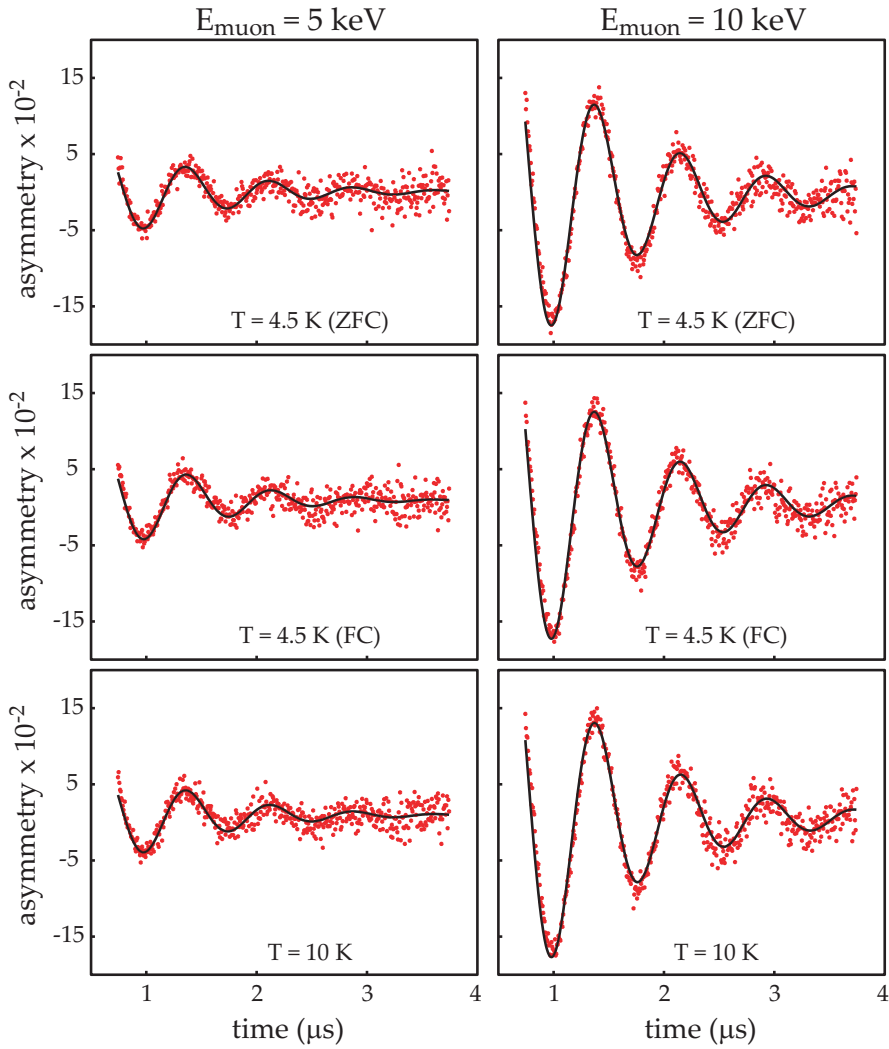


Figure 6.11: Fits to the asymmetry data with muon energies of 5 and 10 keV, taken at temperatures of 10 K and (2x) 4.5 K, one with field cooled (FC) conditions and one with zero field cooled (ZFC) conditions.

data sets. The results obtained for the parameters P_{Nb} and B_{Nb} are shown in Fig. 6.12 and for ϕ_0 and the total error in Fig. 6.13, all as function of the muon energy. For all graphs the green lines are from the data at $T = 10$ K. The red and blue lines are from the data at $T = 4.5$ K, with red for the FC treatment and blue for the ZFC treatment. The results for P_{Nb} are in accordance with

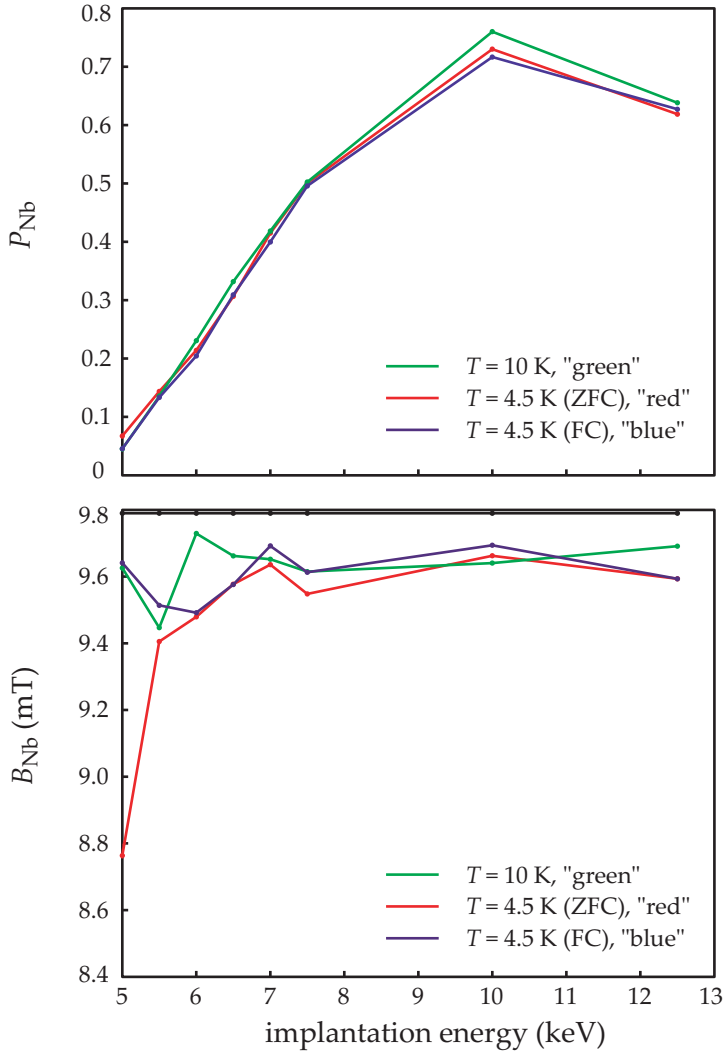


Figure 6.12: Fit parameters P_{Nb} and B_{Nb} as function of the implantation energy of the muons, with green: $T = 10$ K, red: $T = 4.5$ K (field cooled) and blue: $T = 4.5$ K (zero field cooled). Also shown is the value of the applied field of 9.79 mT

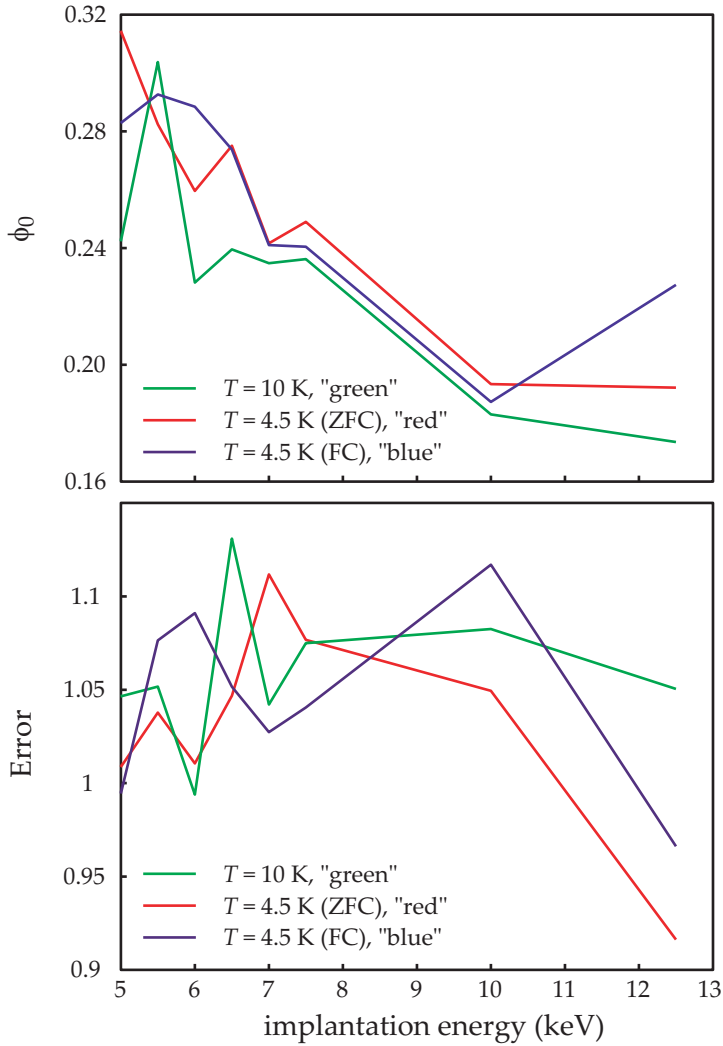


Figure 6.13: Fit parameter ϕ_0 and the error as function of the implantation energy of the muons, with green: $T = 10$ K, red: $T = 4.5$ K (field cooled) and blue: $T = 4.5$ K (zero field cooled).

the stopping profile showing a decrease for lower implantation energies. Also, the three separate curves don't vary much from one to another. The results for B_{Nb} are the most interesting ones because it contains information about the field profile which we try to unravel. It shows that the green (10 K data) and blue (ZFC data) curve are about the same, while the red one (FC data) comes down at the lowest energy. We believe that this decrease to a significantly lower local field value observed for the lowest implantation energy (= closest to the interface) is a signature of the reverse proximity effect. However, we are left with several questions. Why do the ZFC data not show this lowering, why are the all lines significantly below the background field of 9.79 mT, and why do normal state data not really differ from the data taken in the superconducting state.

6.3.3 Discussion and conclusion

To start the discussion with the $T > T_c$ data, it can be surmised that the (global) stray fields coming from the F layers will curl into the Nb layer where they are now directed anti-parallel to the applied field. They exit the Nb layer at the opposing side and curl back into the F layer. This leads to a lowering of the field in the Nb layer. Making a model calculation of the induced field B coming from a homogeneously magnetized squared plate with surface area $L \times L$ and thickness $d \ll L$, we find that at a distance $x_0 \ll L$ away from the surface center (along the surface normal) B approximately is given by:

$$B(x_0) \sim \frac{\mu_0 m_0}{\pi} \left(\arctan\left(\frac{x_0}{\sqrt{2}L}\right) - \arctan\left(\frac{x_0+d}{\sqrt{2}L}\right) \right) \sim -\frac{\mu_0 m_0}{\pi} \frac{d}{\sqrt{2}L} \quad (6.10)$$

where m_0 is the density of magnetic moments inside the plate (in units of A/m) and $\mu_0 = 4\pi \cdot 10^{-7} \text{ N/A}^2$ the magnetic constant. The result is independent of x_0 and the minus sign means a direction opposite to the magnetic moments in the F layer. Consequently, in our F/S/F devices we can expect a global lowering of the field inside the Nb layer. However, inserting the numbers $L = 1 \text{ cm}$, $d = 70 \text{ nm}$ and $m_0 = 0.834 \times 10^6 \text{ A/m}$ (using an atom density of $0.899 \cdot 10^{29} \text{ m}^{-3}$ and an average moment per atom of $1.1\mu_B$), gives a value of $\sim 1.8 \mu\text{T}$, which is significantly less than what we observed. For the $T < T_c$, both the FC and ZFC data are not significantly different from the normal state data for the higher energies. This indicates that no Meissner screening is taking place in the superconducting state. Furthermore, in the ZFC case, the magnetization in the F layer is inhomogeneous because the coercive field for such macroscopic sample is very close to zero (of the order of 0.1 mT). A complex domain state will appear with stray fields connecting the two F layers

across the Nb layer. When such state is frozen during the cool down, it brings vortices crossing the Nb layer, which might in turn pin the domain state in the F layers. Essentially we now have created inhomogeneous magnetization at the interface. This will *reduce* the polarization of the Cooper pairs and is in line with the disappearance of the dip in the fit results. It stands to reason therefore that only the FC state creates the circumstances in which the inverse effect is to be found, and then only for the lowest implantation energies. If there is any effect to see, it is close to the limit of the accuracy of the measurements. Furthermore, it is only for the lowest implantation energy that we are probing close enough to the interface to detect a possible inversion effect. On the other hand, a consistent picture starts to form. In recent works, by different measurement techniques, indications for the existence of the reverse proximity effect have been observed as well [71, 72]. To claim any real sign of the "polarization of the Cooper pairs", more data analysis is needed, where special attention should be paid to the surface roughness of the interface, which smears out the effect due to lateral inhomogeneity in the local fields.

Chapter 7

Critical voltage of a mesoscopic superconductor

This chapter was in a slightly different form published as "Critical Voltage of a Mesoscopic Superconductor, *Phys. Rev. Lett.* 96, 147002 (2006)", with R. S. Keizer and M. Flokstra as equally contributing first authors.

7.1 Introduction

The energy distribution function of quasiparticles in a normal metal is under equilibrium conditions given by the Fermi-Dirac distribution $f_{\text{FD}} = \frac{1}{e^{(\beta\varepsilon)} + 1}$ with $\beta \equiv 1/(k_B T)$ and ε the energy of the quasiparticle measured with respect to the Fermi energy. In recent years it has been demonstrated that in a voltage (V)-biased mesoscopic wire (length L) a two-step non-equilibrium distribution develops [78] with additional rounding by quasiparticle scattering due to spin-flip and/or Coulomb interactions [79]. Figure 7.1a shows the distribution, which resembles two shifted Fermi-Dirac functions:

$$f(x, \varepsilon) = (1 - x) f_{\text{FD}}(\varepsilon + eV/2) + x f_{\text{FD}}(\varepsilon - eV/2) \quad (7.1)$$

with x the coordinate along the wire. For strong enough relaxation ($L \gg L_\phi$, with L_ϕ the phase coherence length) and/or high temperatures ($k_B T \gg eV$) the distribution returns to a Fermi-Dirac distribution with a local effective temperature.

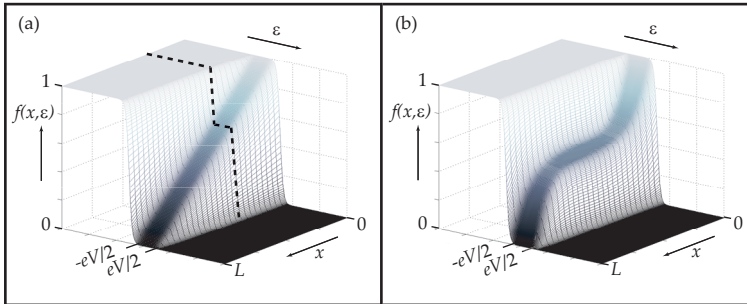


Figure 7.1: Quasiparticle distribution function $f(x, \varepsilon)$ as function of energy ε and position x for a normal wire (a) and a superconducting wire (b) between normal metallic reservoirs for $k_B T \ll eV < \Delta_0$. The dashed line showing the two-step distribution at a fixed location along the wire.

If the normal wire is replaced by a superconducting wire, the attractive interaction between electrons leads to the superconducting state. The questions we address here are how the distribution function inside the superconducting wire is modified (for a typical result see Fig. 7.1b) and how this affects observable properties such as the current-voltage characteristics of the system and the breakdown of the superconducting state. To relate the distribution function to observable quantities, it is convenient to separate the symmetric part f_L (energy mode) from the asymmetric part f_T (charge mode). Here, the

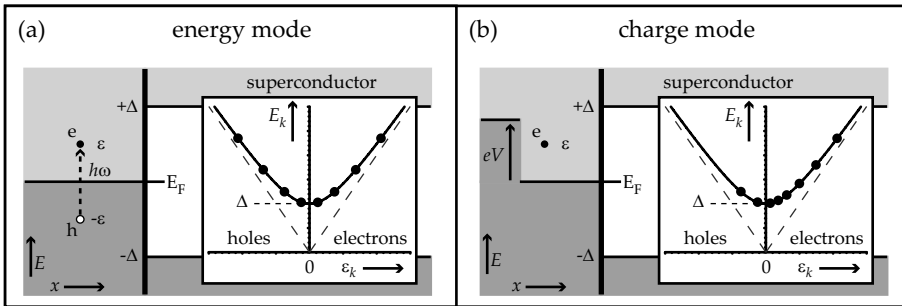


Figure 7.2: An electron excitation in a normal metal created by (a) radiation (of energy $h\omega$) and (b) a potential difference eV (from a connecting reservoir). The excitation in (a) is symmetric in terms of electrons and holes and contributes to the energy mode. The excitation in (b) is antisymmetric and contributes to the charge mode. The insets in both graphs show how these two modes occupy states in the excitation energy spectrum E_k of the superconductor. Here, $E_k = \sqrt{\Delta^2 + \varepsilon_k^2}$ where Δ is the gap energy and ε_k the energy of the single electron state with wave vector \mathbf{k} .

symmetry is in terms of electrons versus holes. In a normal metal, an electron that is excited above the Fermi level at energy ε leaves a hole below the Fermi level at energy $-\varepsilon$. This contributes to the energy mode, and common sources for such symmetric excitations are temperature and radiation (see Fig. 7.2a). The charge mode is asymmetric in electrons and holes. It counts the number of excess electrons or holes in the system. Such asymmetric excitations are created by electrical potential differences (see Fig. 7.2b). The energy mode and charge mode each have a different spatial and spectral form. The decomposition of the typical result shown in Fig. 7.1b into the energy mode and charge mode is shown in Fig. 7.3. The exchange of electrons between the normal metal (reservoir) and the superconducting wire is for sub-gap energies controlled by the Andreev reflection process. The question we thus address is how f_L and f_T enter/ behave in the superconductor, and how that changes its transport properties. In particular, we investigate how the breakdown of the superconducting state occurs.

The transport and spectral properties of dirty superconducting systems ($\ell_e \ll \xi_0$, with ℓ_e the elastic mean free path and ξ_0 the superconducting phase coherence length) are described by the quasiclassical Green functions obeying the Usadel equation [19]. For out of equilibrium systems we use the Keldysh technique in Nambu (particle-hole) space, neglecting spin dependent interactions and assuming conventional superconductivity. Furthermore, we ignore inelastic scattering in the wire and use the time independent formalism. We assume this to be an acceptable simplification at temperatures far below

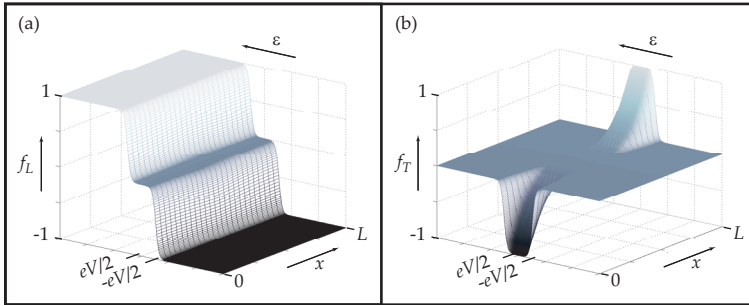


Figure 7.3: Decomposition of the quasiparticle distribution function $f(x, \varepsilon)$ as shown in Fig. 7.1b into the energy mode f_L and charge mode f_T .

the critical temperature T_c , and for large enough wire cross section. In this way the role of thermally activated and respectively quantum phase slips is ruled out [80, 81].

7.1.1 Usadel equation using Keldysh technique

The Keldysh technique is based upon a special ordering of the Green functions, and the main result is that the Green functions are split into three parts. The retarded (\check{G}^R) and advanced (\check{G}^A) parts describe the propagation of particles (electrons and holes) in respectively positive and negative time direction, while the Keldysh (\check{G}^K) part describes the non-equilibrium part of the system. As long as a system is in equilibrium (i.e the quasiparticles are distributed like a Fermi-Dirac distribution with an effective temperature), it is fully characterized by the retarded Green functions, and we can calculate the density of states, electrical current, etc. with the knowledge of the retarded Green functions alone. This changes when the system is driven out of equilibrium, for then we also need to know which energy states are accessible. In other words, we need to know the non-equilibrium distribution function of the quasiparticles. In that case we need to solve the Keldysh Green functions, for which in turn we need both the retarded and advanced Green functions. The latter is actually only necessary when the time symmetry of the system is broken, for example, due to magnetic fields. Otherwise, it follows straightforwardly from the retarded Green functions. Each of these three parts are Nambu \otimes spin space matrices (for their elements see Eq. 2.9 - 2.10), and can be collected together into the Keldysh space effectively creating a matrix Green function of dimension 8×8 . This new matrix Green function then replaces the matrix Green function in the Usadel equation, and the remaining Nambu \otimes spin space

matrices of the Usadel equation are projected onto the 2×2 unity matrix $\hat{1}$ in Keldysh space. However, in the absence of spin dependent interactions the spin space effectively drops out of the equation and the retarded, advanced, and Keldysh matrix Green function reduce to 2×2 matrices in Nambu space (denoted by a hat). The time independent Usadel equation for an s-wave superconductor (see Eq. 2.20) using the Keldysh technique then takes the form:

$$\hbar D \nabla (\check{G} \nabla \check{G}) = -i [\check{H}, \check{G}] \quad (7.2)$$

where D is the diffusion constant and ∇ is the spatial derivative [82]. Furthermore, the spin-flip part vanished because we ignore spin-flip processes in the wire. The elements of \check{G} and \check{H} are 2×2 matrices in Nambu space:

$$\check{G} = \begin{pmatrix} \hat{G}^R & \hat{G}^K \\ 0 & \hat{G}^A \end{pmatrix}, \quad \check{H} = \begin{pmatrix} \hat{H} & 0 \\ 0 & \hat{H} \end{pmatrix} \quad \text{with} \quad \hat{H} = \begin{pmatrix} \varepsilon & -\Delta \\ \Delta^* & -\varepsilon \end{pmatrix} \quad (7.3)$$

where the chosen gauge is such that the pair potential Δ is in equilibrium a real quantity, $\Delta = \Delta^*$. Inserting these Keldysh space matrices into the Usadel equation results in three equation:

$$\begin{aligned} \hbar D \nabla (\hat{G}^R \nabla \hat{G}^R) &= -i [\hat{H}, \hat{G}^R] \\ \hbar D \nabla (\hat{G}^A \nabla \hat{G}^A) &= -i [\hat{H}, \hat{G}^A] \\ \hbar D \nabla (\hat{G}^R \nabla \hat{G}^K + \hat{G}^K \nabla \hat{G}^A) &= -i [\hat{H}, \hat{G}^K] \end{aligned} \quad (7.4)$$

The first two equations are the retarded and advanced part of the Usadel equation. The third equation is the kinetic part of the Usadel equation, describing the non-equilibrium. The retarded, advanced and Keldysh matrix Green functions are connected to each other by the normalization condition for the matrix Green function in the Keldysh space: $\check{G}^2 = \check{1}$. Apart from this condition, there is also a direct connection between the retarded and advanced matrix Green function, which differ only in the time direction of the propagation of the particles. In the absence of time symmetry breaking, the two are related through:

$$\hat{G}^A = -\tau_3 (\hat{G}^R)^\dagger \tau_3 \quad (7.5)$$

and thus finding the retarded Green functions is sufficient to know the advanced Green functions as well. From the normalization condition for \check{G} one obtains $\hat{G}^R \hat{G}^R = \hat{G}^A \hat{G}^A = \hat{1}$ and $\hat{G}^R \hat{G}^K + \hat{G}^K \hat{G}^A = \hat{0}$. These two conditions make that \hat{G}^K can be parameterized as:

$$\hat{G}^K = \hat{G}^R \hat{f} - \hat{f} \hat{G}^A \quad (7.6)$$

It was shown by Schmid and Schön [83], and Larkin and Ovchinnikov [84] that \hat{f} can be chosen as the diagonal generalized distribution number matrix of the quasiparticles in Nambu space: $\hat{f} = f_L(x, \varepsilon) \tau_0 + f_T(x, \varepsilon) \tau_3$, with f_L the symmetric part (energy mode) and f_T the antisymmetric part (charge mode) of the quasiparticle distribution function. The full distribution function is retained by: $2f(x, \varepsilon) = 1 - f_L(x, \varepsilon) - f_T(x, \varepsilon)$. For a bulk superconductor in equilibrium, this distribution function equals the Fermi-Dirac distribution: $f(x, \varepsilon) = f_{\text{FD}}(x, \varepsilon)$

7.1.2 Working out the equations

The retarded matrix Green function in terms of the position and energy dependent normal $g(\varepsilon, x)$ and anomalous $F_i(\varepsilon, x)$ Green functions is (see Eq. 2.21):

$$\hat{G}^R = \begin{pmatrix} g(\varepsilon, x) & F_1(\varepsilon, x) \\ F_2(\varepsilon, x) & -g(\varepsilon, x) \end{pmatrix} \quad (7.7)$$

where it was used that $\bar{g} = -g$, which one obtains from the normalization condition $\hat{G}^R \hat{G}^R = \hat{1}$. The normalization condition also leads to $g^2 + F_1 F_2 = 1$. Substituting all this in the retarded part of the Usadel equation: $\hbar D \nabla (\hat{G}^R \nabla \hat{G}^R) = -i [\hat{H}, \hat{G}^R]$, we find the retarded Usadel equations:

$$\begin{aligned} \hbar D [g \nabla^2 F_1 - F_1 \nabla^2 g] &= -2i \Delta g - 2i \varepsilon F_1 \\ \hbar D [F_1 \nabla^2 F_2 - F_2 \nabla^2 F_1] &= 2i \Delta F_2 + 2i \Delta^* F_1 \end{aligned} \quad (7.8)$$

The second equation is essential when calculating the non-equilibrium properties of superconductors. Its left-hand-side is proportional to the divergence of the spectral (energy-dependent) supercurrent, which is (compared to the equilibrium case) no longer a conserved quantity.

Using the general relation between the advanced matrix Green function and the retarded matrix Green function: $\hat{G}^R = -\tau_3 (\hat{G}^A)^\dagger \tau_3$, the Keldysh matrix Green function \hat{G}^K can be written entirely in terms of g , F_1 , F_2 , f_L and f_T :

$$\hat{G}^K = \begin{pmatrix} (g + g^\dagger) f_+ & F_1 f_- - F_2^\dagger f_+ \\ F_2 f_+ - F_1^\dagger f_- & -(g + g^\dagger) f_- \end{pmatrix} \quad (7.9)$$

where $f_\pm = f_L \pm f_T$. Working out the kinetic part of the Usadel equation: $\hbar D \nabla (\hat{G}^R \nabla \hat{G}^K + \hat{G}^K \nabla \hat{G}^A) = -i (\hat{H}, \hat{G}^K)$ we find (combining the diagonal

components) the kinetic equations describing the non-equilibrium part:

$$\begin{aligned}\hbar D \nabla j_{\text{energy}} &= 0 \\ \hbar D \nabla j_{\text{charge}} &= 2R_L f_L + 2R_T f_T\end{aligned}\tag{7.10}$$

The various elements in Eq. 7.10 are given by:

$$\begin{aligned}j_{\text{energy}} &= \Pi_L \nabla f_L + \Pi_X \nabla f_T + j_\varepsilon f_T \\ j_{\text{charge}} &= \Pi_T \nabla f_T - \Pi_X \nabla f_L + j_\varepsilon f_L \\ \Pi_L &= \frac{1}{4} \left(2 + 2|g|^2 - |F_1|^2 - |F_2|^2 \right) \\ \Pi_T &= \frac{1}{4} \left(2 + 2|g|^2 + |F_1|^2 + |F_2|^2 \right) \\ \Pi_X &= \frac{1}{4} \left(|F_1|^2 - |F_2|^2 \right) \\ j_\varepsilon &= \frac{1}{2} \Re \{ F_1 \nabla F_2 - F_2 \nabla F_1 \} \\ R_L &= -\frac{1}{2} \Im \{ \Delta F_2 + \Delta F_1^\dagger \} \\ R_T &= -\frac{1}{2} \Im \{ \Delta F_2 - \Delta F_1^\dagger \}\end{aligned}\tag{7.11}$$

Equations 7.10 are two coupled diffusion equations for f_L and f_T , describing the divergences in the spectral energy current and the spectral charge current. The total charge current is given by $J = \frac{1}{2e\rho} \int j_{\text{charge}} d\varepsilon$ with ρ the resistivity. The terms Π_L and Π_T can be related to an effective diffusion constant for the energy and charge mode respectively and Π_X as a "cross-diffusion" between them. j_ε is the spectral supercurrent and R_L and R_T describe the "leakage" of spectral current to different energies, where the total leakage-current $\propto \int (R_L f_L + R_T f_T) d\varepsilon$ is zero. In the small signal limit the terms Π_X , j_ε and R_L are small and can in many cases be neglected (linear approach), effectively decoupling f_L and f_T . In this work, we go beyond this limit. The Usadel equation is supplemented by a self-consistency relation:

$$\hat{H}_{(1,2)} = \frac{N_0 V_{\text{eff}}}{4} \int_{-\hbar\omega_D}^{\hbar\omega_D} \hat{G}_{(1,2)}^K d\varepsilon\tag{7.12}$$

Here, N_0 is the normal density of states around the Fermi energy, V_{eff} the effective attractive interaction and the integral limits are set by the Debye energy $\hbar\omega_D$. The resulting equation for Δ becomes:

$$\Delta = -\frac{1}{4} N_0 V_{\text{eff}} \int_{-\hbar\omega_D}^{\hbar\omega_D} \left((F_1 - F_2^\dagger) f_L - (F_1 + F_2^\dagger) f_T \right) d\varepsilon.\tag{7.13}$$

To calculate spectral and transport properties, one needs to know the self-consistent solution of Δ . In most practical cases, this has to be done numerically. A convenient solution scheme is to first find the Green functions of the system by solving the retarded equations for a certain Δ , next to determine the quasiparticle distribution functions by solving the kinetic equations and then calculate a new Δ using the self-consistency relation. This process has to be repeated until Δ converges. As a starting value for Δ we use the BCS form at zero temperature. A typical solution employs a grid of in the order of 10^4 energies, 10^2 spatial coordinates, and 10^3 iterations of Δ . The stability of the solution scheme was tested extensively by inserting different initial values. At all the applied voltages self-consistent steady state solutions are found. To simplify the calculations a parameterization is used that automatically fulfills the normalization condition. It is convenient to take $g = \cosh(\theta)$, $F_1 = \sinh(\theta)e^{i\chi}$ and $F_2 = -\sinh(\theta)e^{-i\chi}$, where θ and χ are position and energy dependent (complex) variables. At the interfaces between the superconducting wire and the normal metallic reservoirs we use the following boundary conditions: $\theta = \nabla\chi = 0$ (retarded equation) and $f_{L,T} = \frac{1}{2}(\tanh \frac{\varepsilon+eV}{2k_B T} \pm \tanh \frac{\varepsilon-eV}{2k_B T})$ (kinetic equation), where the latter are the usual reservoir distribution functions.

7.1.3 Simulation on the NSN system

The transport properties of the NSN system (see Inset Fig. 7.4) can now be calculated with the equations described above. In a previous analysis a finite differential conductance was found at zero bias employing a linear response calculation [85]. With the approach introduced here, the full current-voltage relation can be obtained. The result at several temperatures is displayed in Fig. 7.4, with the voltage normalized to $\Delta_0 (= \Delta_{\text{bulk}, T=0})$ and the current density normalized to the critical current density $J_c \approx 0.75 \frac{\Delta_0}{\xi_0 \rho_e}$ [86], with $\xi_0 = \sqrt{\hbar D / \Delta_0}$. At $T = 0$ we observe a linear resistance at low voltages caused by the decay of f_T (Fig. 7.3b), and a critical point (voltage) above which the resistance is equal to the normal state resistance. At higher temperatures ($T = 0.5 T_c, 0.75 T_c$) a linear approach would only give an adequate approximation in a limited voltage range. We will argue below that the superconductor switches to the normal state by f_L which is controlled by the *voltage* and cannot be interpreted as a critical current. In Fig. 7.5 the electrostatic potential $\phi = \int_0^\infty f_T \Re\{g\} d\varepsilon$ along the wire is shown at zero temperature prior to ($eV/\Delta_0 = 0.013, 0.646$) and immediately after ($eV/\Delta_0 = 0.651$) the transition. The potential can be seen to drop to zero over a distance of the order of the coherence length due to the normal- to supercurrent conversion. This mechanism also gives rise to the finite zero bias resistance. The profile hardly changes

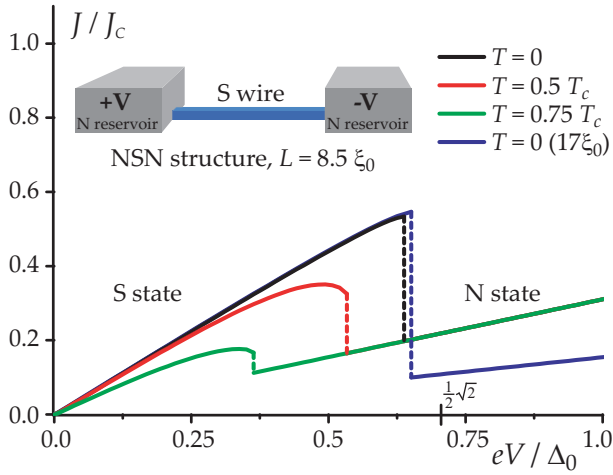


Figure 7.4: The calculated current (J)-voltage (V) relation of a superconducting wire of length $L = 8.5\xi_0$ between normal metallic reservoirs (see inset) at several temperatures, and for a wire of length $17\xi_0$ at $T = 0$. J_c is the critical current density, and Δ_0 the bulk gap energy.

over the full range of voltages, until the critical value is reached, after which the electrostatic potential drops in a linear fashion, indicating the system is in the normal state. The minimal changes emphasize the limited influence of f_T on the superconducting state (i.e. on Δ). The current density at which the

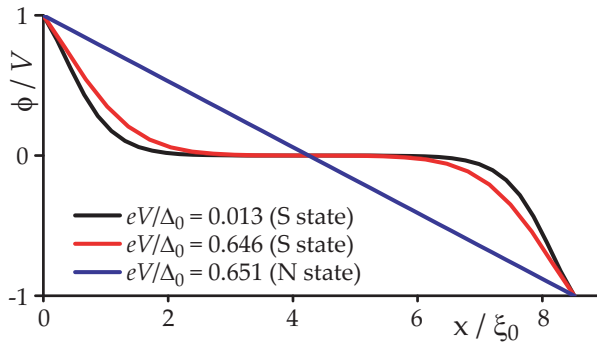


Figure 7.5: The normalized electrostatic potential ϕ as a function of position x along the superconducting wire for bias voltages prior to and immediately after the transition (at $T = 0$).

superconductor switches to the normal state (for $T = 0$) is much smaller than

the critical current density in an infinitely long wire ($J/J_c = 1$). This excludes the depairing mechanism as the (main) cause of the transition. Moreover, it is acceptable to ignore the occurrence of phase slip centers [87], which are time-dependent solutions that are energetically favorable when $J \approx J_c$. Neither is the transition triggered at the weaker superconducting edges as indicated by the shape of the electrostatic potential profile in Fig. 7.5.

7.1.4 Simulation on the non-local system

The parameter that determines whether or not the superconducting state exist is Δ , as follows from Eq. 7.13. The integral in this self-consistency equation sums all pair states (either occupied by a Cooper pair, or empty). F_i gives the Cooper pair density-of-states and f_L and f_T determine which of those states are doubly occupied or doubly empty and which are singly occupied (broken) due to the presence of quasiparticles. In equilibrium at $T = 0$, a switch to the normal state can only be caused by reaching a critical phase gradient, entering Δ via F_i . In the presence of quasiparticles, Δ (and thus potentially the state of the system) is also influenced by the distribution functions. It was noticed above that the charge mode f_T has a very limited influence on Δ . The effect of the energy mode f_L is examined below.

By a small modification of our system to a T-shaped geometry as shown in Fig. 7.6, we can in a direct way disentangle the effects of f_L and f_T on Δ . This setup can be thought of as the connection of the superconducting wire to the center of a normal wire. In the middle of such a wire f_T is equal to zero, but f_L is not. The result for the pair potential at the edge of the superconducting wire as a function of the voltage of the reservoirs is shown in Fig. 7.6. Although there is no net current flowing through the superconductor, at a certain voltage the pair potential collapses. The voltage that is necessary to trigger this transition to the normal state is very close to the transition in Fig. 7.4 (where we used the two terminal setup). Apparently the influence of f_L is important, since it can cause the superconductor to switch to the normal state irrespective of the value of the supercurrent. Clearly the influence of f_L on the state of the superconductor is larger than the influence of the supercurrent on this same quantity.

The quantity that defines the possible states of the system is the free energy. Evidently the superconductor compares two states for the minimization of this free energy: the first state is the superconducting state in which the free energy remains constant as a function of voltage (and independent of the shape of f_L provided this shape does not change for energies larger than the

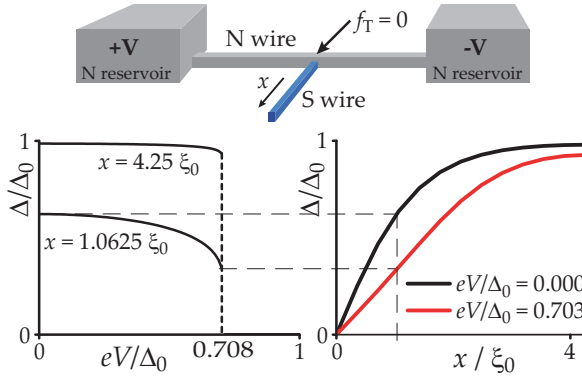


Figure 7.6: Top: T-shaped geometry, bottom: pair potential Δ in the S-wire as function of (left) voltage at two different positions; (right) position at two different voltages. The breakdown voltage is at $eV/\Delta_0 = 0.707$. The wire length is $4.25 \xi_0$

gap). The second possible state is the normal state. At zero temperature, in the absence of a bias voltage, the difference in free energy between the two states is the condensation energy of the superconductor. When the voltage is increased (but still $eV < \Delta$), the free energy of the superconducting state remains constant while the free energy of the normal state decreases since in that case electrons occupy higher energy states due to the applied voltage. To illustrate the effect, we calculate explicitly the (internal) energy difference between the superconducting state (E_S) and normal state (E_N) at zero temperature for both a bulk superconductor (analytically) and the T-shaped structure (numerically) as a function of voltage (which appears in f_L) and Δ . From the analytical calculation for the bulk, following Bardeen [88], we find that f_L changes the energy in such a way that at $eV = \frac{1}{2}\sqrt{2}\Delta_0$ the superconductor undergoes a first order phase transition. For the voltage range $\frac{1}{2}\Delta_0 < eV < \Delta_0$ the state of the system has two solutions (two minima). The energy difference for the bulk superconductor is shown in Fig. 7.7. Numerical results for the energy of the T-shaped geometry are shown as well (both as function of position and as function of voltage). For long wires, the numerical results approach the analytical (bulk) calculation. This indicates that the effect of the bias voltage can indeed be related to the existence of a first order phase transition at zero temperature.

In conclusion, we have studied the role of the energy mode f_L of the quasi-

Hysteretic behavior due to the first order transition is also present in the numerical calculation, for clarity in Fig. 7.4 and 7.6 only the upsweeps are displayed.

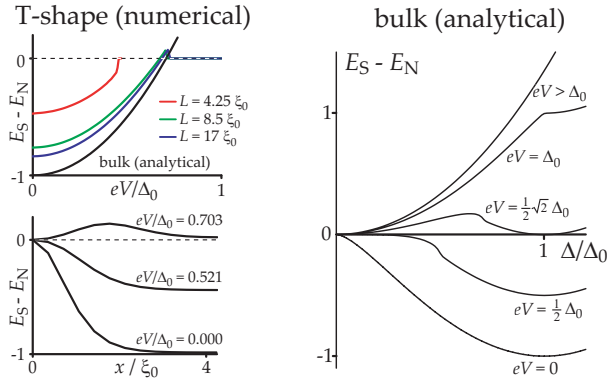


Figure 7.7: Energy difference between the superconducting and normal state. Right: analytical bulk solution showing the bistable voltage range. Left: numerical solutions for (top) increasing wire length as function of voltage and (bottom) for a $4.25 \xi_0$ long wire as function of position (energy thus being a density). Energies are normalized to $H_c^2(0)/8\pi$.

particle distribution on the properties of a superconducting nanowire. We employ a numerical simulation of the Usadel equation in full-response and find a non-thermal distribution for f_L (caused by an applied bias voltage) which drives a first order transition from the superconducting state to the normal state irrespective of the current. A direct calculation on the internal energy of a bulk superconductor confirms that the voltage indeed causes the phase transition. In general, the significant role played by f_L found in these superconducting nanowires stresses the importance of treating f_L and f_T on equal footing.

Bibliography

- [1] H. K. Onnes, Leiden Commun. **119b**, **120b**, **122b**, **124c** (1911).
- [2] J. G. Bednorz and K. A. Müller, Rev. Mod. Phys. **60**, 585 (1988).
- [3] W. Meissner and R. Ochsenfeld, Naturwiss. **21**, 787 (1933).
- [4] R. Meservey, P. M. Tedrow, and P. Fulde, Phys. Rev. Lett. **25**, 1270 (1970).
- [5] P. M. Tedrow and R. Meservey, Phys. Rev. Lett. **26**, 192 (1971).
- [6] P. M. Tedrow and R. Meservey, Phys. Rev. B **7**, 318 (1973).
- [7] M. Tinkham and J. Clarke, Phys. Rev. Lett. **28**, 1366 (1972).
- [8] M. Tinkham, Phys. Rev. B **6**, 1747 (1972).
- [9] L. R. Tagirov, Phys. Rev. Lett. **83**, 2058 (1999).
- [10] A. I. Buzdin, A. V. Vedyayev, and N. V. Ryzhanova, Europhys. Lett. **48**, 686 (1999).
- [11] L. N. Cooper, Phys. Rev. **104**, 1189 (1956).
- [12] J. Bardeen, L. N. Cooper, and J. R. Schrieffer, Phys. Rev. **106**, 162 (1957).
- [13] J. Bardeen, L. N. Cooper, and J. R. Schrieffer, Phys. Rev. **108**, 1175 (1957).
- [14] N. N. Bogoliubov, Sov. Phys. JETP **7** (1958).
- [15] P. G. D. Gennes, *Superconductivity of Metals and Alloys* (Benjamin, New York, 1966).
- [16] G. E. Blonder, M. Tinkham, and T. M. Klapwijk, Phys. Rev. B **25**, 4515 (1982).

-
- [17] A. Kastalsky *et al.*, Phys. Rev. Lett. **67**, 3026 (1991).
- [18] A. A. Abrikosov, L. P. Gor'kov, and I. E. Dzyaloshinski, *Methods of Quantum Field Theory in Statistical Physics* (Dover, 1963, 1963).
- [19] N. Kopnin, *Theory of Nonequilibrium Superconductivity* (Oxford University Press, 2001).
- [20] L. P. Gor'kov, Sov. Phys. JETP **7**, 505 (1958).
- [21] L. P. Gor'kov, JETP **9**, 1364 (1959).
- [22] V. L. Ginzburg and L. D. Landau, JETP **20**, 1064 (1950).
- [23] G. Eilenberger, Zeitschrift für Physik **214**, 195 (1968).
- [24] A. A. Abrikosov and L. P. Gor'kov, JETP **8**, 1090 (1959).
- [25] K. D. Usadel, Phys. Rev. Lett. **25**, 507 (1970).
- [26] P. W. Anderson and P. Morel, Phys. Rev. **123**, 1911 (1961).
- [27] R. Balian and N. R. Werthamer, Phys. Rev. **131**, 1553 (1963).
- [28] A. Leggett, Rev. Mod. Phys. **76**, 999 (2004).
- [29] R. S. Keizer *et al.*, Nature **439**, 825 (2006).
- [30] I. Sosnin, H. Cho, V. T. Petrashov, and A. F. Volkov, Phys. Rev. Lett. **96**, 157002 (2006).
- [31] F. S. Bergeret, A. F. Volkov, and K. B. Efetov, Rev. Mod. Phys. **77**, 1321 (2005).
- [32] P. Fulde and R. A. Ferrell, Phys. Rev. **135**, A550 (1964).
- [33] A. I. Larkin and Y. N. Ovchinnikov, Sov. Phys. JETP **20**, 762 (1965).
- [34] R. O'Handley, *Modern Magnetic Materials* (Wiley and Sons, New York, 2000).
- [35] A. F. Andreev, Sov. Phys. JETP **19**, 1228 (1964).
- [36] M. J. M. de Jong and C. W. J. Beenakker, Phys. Rev. Lett. **74**, 1657 (1995).
- [37] E. A. Demler, G. B. Arnold, and M. R. Beasley, Phys. Rev. B **55**, 15174 (1997).

-
- [38] A. Kadigrobov, R. I. Shekhter, and M. Jonson, *Europhys. Lett.* **54**, 394 (2001).
- [39] F. S. Bergeret, A. F. Volkov, and K. B. Efetov, *Phys. Rev. Lett.* **86**, 4096 (2001).
- [40] M. Eschrig and T. Löfwander, *Nature Physics* **4**, 138 (2008).
- [41] A. I. Buzdin, *Rev. Mod. Phys.* **77**, 935 (2005).
- [42] I. F. Lyuksyutov and V. L. Pokrovsky, *Adv. in Phys.* **54**, 67 (2005).
- [43] M. Eschrig, J. Kopu, J. C. Cuevas, and G. Schön, *Phys. Rev. Lett.* **90**, 137003 (2003).
- [44] Y. Obi, M. Ikebe, T. Kubo, and H. Fujimori, *Physica C* **317**, 149 (1999).
- [45] L. Lazar *et al.*, *Phys. Rev. B* **61**, 3711 (2000).
- [46] V. V. Ryazanov *et al.*, *Phys. Rev. Lett.* **86**, 2427 (2001).
- [47] T. Kontos, M. Aprili, J. Lesueur, and X. Grison, *Phys. Rev. Lett.* **86**, 304 (2001).
- [48] J. Gu *et al.*, *Phys. Rev. Lett.* **89**, 267001 (2002).
- [49] A. Potenza and C. H. Marrows, *Phys. Rev. B* **71**, 180503(R) (2005).
- [50] I. C. Moraru, J. W. P. Pratt, and N. O. Birge, *Phys. Rev. Lett.* **96**, 037004 (2006).
- [51] A. Y. Rusanov, S. Habraken, and J. Aarts, *Phys. Rev. B* **73**, 060505(R) (2006).
- [52] I. C. Moraru, J. W. P. Pratt, and N. O. Birge, *Phys. Rev. B* **74**, 220507(R) (2006).
- [53] D. Stamopoulos, E. Manios, and M. Pissas, *Phys. Rev. B* **75**, 184504 (2007).
- [54] R. Steiner and P. Ziemann, *Phys. Rev. B* **74**, 094504 (2006).
- [55] G. Carapella, F. Russo, and G. Costabile, *Phys. Rev. B* **78**, 104529 (2008).
- [56] A. Y. Rusanov, M. Hesselberth, J. Aarts, and A. I. Buzdin, *Phys. Rev. Lett.* **93**, 057002 (2004).

- [57] C. Cirillo, A. Rusanov, C. Bell, and J. Aarts, Phys. Rev. B **75**, 174510 (2007).
- [58] A. Rusanov, R. Boogaard, M. Hesselberth, H. Sellier, and J. Aarts, Physica C **369**, 300 (2002).
- [59] A. Y. Rusanov, M. Hesselberth, and J. Aarts, Phys. Rev. B **70**, 024510 (2004).
- [60] V. V. Ryazanov, private communication .
- [61] R. J. Kinsey, G. Burnell, and M. G. Blamire, IEEE Trans. Appl. Superc. **11**, 904 (2001).
- [62] E. C. Stoner and E. P. Wohlfarth, Phil. Trans. Roy. Soc. A **240**, 599 (1948).
- [63] A. Ruotolo, C. Bell, C. W. Leung, and M. G. Blamire, Jn. Appl. Phys. **96**, 512 (2004).
- [64] S. V. Dubonos, A. K. Geim, K. S. Novoselov, and I. V. Grigorieva, Phys. Rev. B **65**, 220513(R) (2002).
- [65] H.-Y. Wu, J. Ni, J.-W. Cai, Z.-H. Cheng, and Y. Sun, Phys. Rev. B **76**, 024416 (2007).
- [66] C. Monton, F. de la Cruz, and J. Guimpel, Phys. Rev. B **77**, 104521 (2008).
- [67] Y. V. Fominov, A. A. Golubov, and M. Y. Kupriyanov, JETP Lett. **77**, 510 (2003).
- [68] M. Flokstra and J. Aarts, Phys. Rev. B **80**, 144513 (2009).
- [69] T. Trunk, M. Redjidal, A. K'akay, M. F. Ruane, and F. B. Humphrey, J. Appl. Phys. **89**, 7606 (2001).
- [70] M. Redjidal, J. H. Giusti, M. F. Ruane, and F. B. Humphrey, IEEE Trans. Magn. **39**, 2684 (2003).
- [71] J. Xia, V. Shelukhin, M. Karpovski, A. Kapitulnik, and A. Palevski, Phys. Rev. Lett. **102**, 087004 (2009).
- [72] R. I. Salikhov *et al.*, Phys. Rev. Lett. **102**, 087003 (2009).
- [73] P. Bakule and E. Morenzoni, Contemporary Physics **45**, 203 (2004).

- [74] H. Luetkens *et al.*, Phys. Rev. Lett. **91**, 017204 (2003).
- [75] A. J. Drew *et al.*, Phys. Rev. Lett. **95**, 197201 (2005).
- [76] H. Luetkens, private communication .
- [77] W. H. Press, *Numerical Recipes* (Cambridge University Press, 2007).
- [78] H. Pothier, S. Guéron, N. O. Birge, D. Esteve, and M. H. Devoret, Phys. Rev. Lett. **79**, 3490 (1997).
- [79] F. Pierre *et al.*, Phys. Rev. B **68**, 085413 (2003).
- [80] C. Lau, N. Markovic, M. Bockrath, A. Bezryadin, and M. Tinkham, Phys. Rev. Lett. **87**, 217003 (2001).
- [81] A. D. Zaikin, D. S. Golubev, A. van Otterlo, and G. T. Zimányi, Phys. Rev. Lett. **78**, 1552 (1997).
- [82] Where we introducing the phase χ : $\phi = \chi - \frac{2e}{\hbar} \int_0^L x A(l) dl$.
- [83] A. Schmid and G. Schön, J. Low Temp. Phys. **20**, 207 (1975).
- [84] A. I. Larkin and Y. N. Ovchinnikov, Sov. Phys. JETP **46**, 155 (1977).
- [85] G. R. Boogaard, A. H. Verbruggen, W. Belzig, and T. M. Klapwijk, Phys. Rev. B **69**, 220503(R) (2004).
- [86] A. Anthore, H. Pothier, and D. Esteve, Phys. Rev. Lett. **90**, 127001 (2003).
- [87] J. S. Langer and V. Ambegaokar, Phys. Rev. **164**, 489 (1967).
- [88] J. Bardeen, Rev. Mod. Phys. **34**, 667 (1962).

Samenvatting

Dit proefschrift beschrijft een serie metingen en een theoretische analyse om meer duidelijkheid te krijgen in de fundamentele werking van supergeleidende systemen wanneer deze in contact worden gebracht met (ferro)magnetische systemen, of wanneer deze zelf in een bijzondere niet-evenwichts situatie wordt gebracht. De aandacht ligt hierbij op de (elektronische) transport eigenschappen van dergelijke gekoppelde systemen, waarbij de werking van de afzonderlijke onderdelen ervan goed bekend is.

De wisselwerking tussen de elektronische toestanden in de supergeleider en de ferromagneet zijn antagonistisch van aard. In de supergeleider vindt paarvorming van elektronen plaats (Cooper paren), waarbij de spins, en dus de magnetisch momenten, van de twee elektronen antiparallel staan. In de ferromagneet is er juist een drijvende kracht om de elektron spins gelijk te richten. Wanneer beide systeem gekoppeld worden ontstaat er aan het grensvlak een competitie tussen beide elektron toestanden, met een nieuwe en niet-triviale toestand als resultaat. Deze is vanuit fundamenteel oogpunt erg interessant, maar biedt ook de mogelijkheid tot nieuwe toepassingen.

Eén van de systemen die de laatste jaren veel aandacht heeft gekregen is de supergeleidende spin-switch (of: -schakelaar). In dit systeem worden twee ferromagnetische lagen gekoppeld door een supergeleidende laag en is de richting van de magnetisatie in de ferromagneten bepalend voor de mate van onderdrukking van de supergeleiding in de tussenlaag. De theoretische voorspelling is dat complete onderdrukking van de supergeleidende toestand optreedt wanneer de magnetisatie in de ferromagneten parallel staat, terwijl in de anti-parallele situatie er wel supergeleiding mogelijk is. Dit is de feitelijke spin-switch: het aan/uit zetten van een (super)stroom door de supergeleider door middel van een kleine manipulatie aan de ferromagneten. Experimenten aan zwakke ferromagneten lijken de theorie te bevestigen, zij het met een heel wat kleiner gemeten effect dan voorspeld, maar ook zijn experimenten met sterke ferromagneten gerapporteerd die een omgekeerd effect laten zien. Wat tot nu toe weinig aandacht kreeg is de invloed van magnetische domeinen. Een groot deel van de hier beschreven experimenten gaat over de effecten van

domein vorming op de wisselwerking tussen de supergeleider en de ferromagneet.

In hoofdstuk 4 en 5 onderzoeken we de effecten van magnetische domeinen in dubbellagen en spin-switch geometrieën. In hoofdstuk 4 gebruiken we het zwak ferromagnetische materiaal CuNi met Nb als supergeleider. In hoofdstuk 5 gebruiken we het sterk ferromagnetische materiaal NiFe, wederom met Nb als supergeleider. We doen veld-afhankelijke weerstands metingen zowel vlak boven als beneden de supergeleidende transitie temperatuur T_c van het Nb, maar ook kritieke stroom metingen ver beneden T_c om te zien of de gevonden effecten eveneens plaats vinden wanneer de supergeleider tot volle sterkte is gekomen. Een hoofdconclusie is dat de effecten van de magnetische domeinen minstens zo belangrijk zijn als de effecten beschreven in het standaardmodel van de spin-switch, en dat ze ook de oorzaak zijn van de omkeer van de werking van het systeem. In de spin-switch met zwakke ferromagneten is de supergeleiding gebaat bij domein vorming doordat het feitelijk een minder parallele magnetische toestand is, en daardoor minder onderdrukkend voor de Cooper paren. In de spin-switch met sterke ferromagneten zorgt een bijeffect van de domeinen, de dipool-strooivelden, er juist voor dat de supergeleider sterker wordt onderdrukt.

In hoofdstuk 6 onderzoeken we de op NiFe gebaseerde sandwiches op een ander voorspeld effect aan de grenslaag van supergeleider en ferromagneet, namelijk mogelijke indringing van magnetisme in de supergeleider. Hiervoor maken we gebruik van een geavanceerde meetopstelling waarin muonen (een elementair deeltje wat enigszins lijkt op een zeer zwaar elektron) in het systeem geschoten worden en die vervolgens het lokale magneetveld meten. Het experiment toont inderdaad de aanwezigheid van magnetizatie aan de supergeleidende kant van het grensvlak aan, hoewel de data analyse bemoeilijkt wordt doordat de grootte van de effecten tegen de gevoeligheid van het meetsysteem aan zitten.

In Hoofdstuk 7 doen we een theoretisch onderzoek aan de werking van een (mesoscopische) supergeleidende draad wanneer de elektronische toestanden in een niet-thermisch evenwicht wordt gebracht door de draad aan weerszijden te koppelen aan normaal metallische reservoirs en vervolgens over die reservoirs een elektrisch spanning te plaatsen. Als functie van deze spanning, en de daardoor opgewekte stroom, modelleren we de verandering van de elektronische toestanden in de supergeleider en het effect ervan op de supergeleider. Het blijkt dat we niet de verwachte (standaard) kritische stroom vinden, waarbij de supergeleider in de normale toestand wordt gedrukt doordat de Cooper paren uit elkaar worden getrokken. In plaats daarvan vinden we dat, voordat deze stroom bereikt wordt, de supergeleiding al door een heel ander effect

onderdrukt wordt, namelijk door de niet-thermische verdelings functies van de elektronen. Aangezien deze bepaald wordt door de spanning over de reservoirs spreken we hier over een kritieke spanning.

List of Publications

1. R. S. Keizer, M. G. Flokstra, J. Aarts, and T. M. Klapwijk
Critical voltage of a mesoscopic superconductor
Phys. Rev. Lett. **96**, 147002 (2006)
2. M. Flokstra, J. Aarts
Domain-wall enhancement of superconductivity in superconductor/ferromagnet hybrids: Case of weak ferromagnets
Phys. Rev. B **80**, 144513 (2009)
3. M. Flokstra, J. M. v.d. Knaap and J. Aarts
Magnetic coupling in superconducting spin valves with strong ferromagnets
to be submitted to Phys. Rev. B
4. J. Aarts, C. Attanasio, C. Bell, C. Cirillo, M. Flokstra and J. M. v.d. Knaap
Superconductor / Ferromagnet hybrids : bilayers and spin switching
to appear in the Springer Series NanoScience and Technology
(eds. V. Moshchalkov and R. Wördenweber).
5. R. S. Keizer, M. G. Flokstra, J. Aarts, and T. M. Klapwijk
Critical voltage of a mesoscopic superconductor between normal electrodes
Proceedings of the 24th international conference on low temperature physics,
AIP Conference Proceedings 850, 755 (2006)

Curriculum Vitae

Machiel Flokstra

Born on the 10th of July 1979 in Oldenzaal, The Netherlands.

- 1991-1997 High school
Thij college, Oldenzaal
- 1997-2003 M.Sc. Applied Physics
Delft University of Technology.
Graduate research in the group of prof.dr.ir. T.M. Klapwijk.
Subject: Anomalous behavior in nano Schottky diodes
- 2004-2009 Ph.D. research at Universiteit Leiden
Supervision by prof.dr. J Aarts
Subject: Proximity effects in superconducting spin-valve structures

Acknowledgements

This thesis has benefited greatly from discussions I had with several people, whom I would like to thank here.

First of all I would like to express my gratitude to my promotor, Jan Aarts. Thank you for creating a research project for me after I came knocking at your door. I have always enjoyed our discussions about physics and appreciated your involvement in the experiments, especially during the first years.

I thank Ruurd Keizer for our many fruitful discussions about physics, which have been a driving force for my work. I am particularly proud of our long summer of modelling Green functions that started out purely as a hobby during weekends but eventually turned into a nice piece of scientific work.

With great pleasure I thank all of the MSM gang for the nice time we shared both in and out of the lab. In particular I want to thank Marcel Hesselberth for all the technical support and for keeping the sample fabrication facilities up and running... most of the time! Thanks to Chris Bell for pushing always enthusiastically for more measurements and to Jorina van der Knaap for helping me during my initial work on spin-valves. Thanks to Federica Galli for all the given compliments (and returning of lent items), to Carla Cirillo for sharing the "langzaam te leven" motto which became the start of many more office mottos. A big thanks goes to the Tibi-Taxi and both its chauffeurs, Oana and Tibi Sorop, it has been a place for physics discussions and, well, resting moments.

I have been very fortunate in collaborating with the muon crew at St Andrews: Stephen Lee, Stephen Lister, David Heron and Soumya Jyoti Ray. The muon experiments we did at the PSI facility were all a great experience, which also gave me a lot of enjoyment. Our humongous lunch in a (almost) deserted canteen and the limping shoulder are not easily forgotten.

During my PhD in Leiden I remained "faithful" to the flat in Delft where I lived as a student. I owe a lot of good moments to my flat mates Luc and Ruurd and also to our frequent visiting guests: Gerrit-Jan and Antonie, with whom we spend many weekends of overdosing on playing cards.

Last but not least, I thank my family for all the given support, especially

near the end of completing this thesis (including the Malm, the Bjursta, ...). I am particularly grateful for the unconditional support I received from Violeta.

